MODELLING COSMIC RAY GROUND LEVEL ENHANCEMENTS AND RELATIVISTIC SOLAR PROTON ACCELERATION

Daniel J. Bombardieri. B.Sc. (Honours)

Submitted in fulfilment of the requirements for the degree of

DOCTOR OF PHILOSOPHY

at the

UNIVERSITY OF TASMANIA
HOBART

June 2008

Declaration

This thesis contains no material which has been accepted for a degree or diploma by the University of Tasmania or any tertiary institution. To the best of the author's knowledge and belief, this thesis contains no material previously published or written by another person, except where due reference is made in the text.

DANIEL JAMES BOMBARDIERI

25-JANUARY-08

Authority of Access

I consent to this thesis being made available for loan and limited copying in accordance with the *Copyright Act 1968*.

DANIEL JAMES BOMBARDIERI

25-JANUARY-08

ABSTRACT

Three solar cosmic ray ground level enhancements (GLEs) have been analysed to better understand the acceleration of protons to relativistic energies during major solar eruptive events. These GLEs, amongst the largest of solar cycle 23, occurred on 14 July 2000, 15 April 2001 and 20 January 2005.

A global analysis technique is used to derive the spectrum, the axis of symmetry of the particle arrival and the anisotropy of relativistic solar protons arriving at Earth. The modelling procedure employs a least squares method to efficiently analyse parameter space for optimum solutions.

Theoretical shock and stochastic acceleration models were used to investigate the source mechanisms. For each GLE, fluxes generated from the response of the global neutron monitor network were input to a generalised non-linear least squares program to assess the respective acceleration models. Analyses were restricted to protons of energy $\geq$450 MeV to avoid complications arising from transport processes which can delay the arrival of low-energy protons.

Each GLE was marked by a strong anisotropic onset. However, for the July 2000 and January 2005 GLEs, the field-aligned component of the pitch angle distribution began to broaden several minutes after their onset and, in addition, local scattering began to increase. For the July 2000 GLE the isotropic component in pitch angle distributions is probably due to scattering effects associated with the interplanetary magnetic field (IMF). For the January 2005 GLE, part of the underlying isotropic component in the pitch angle distributions is attributed to bi-directional flow. Back-scattering from a reflecting boundary beyond Earth is a likely cause. In the case of the April 2001 GLE, the comparatively smaller isotropic component in the pitch angle distributions is probably the result of limited local scattering associated with the IMF.

During the rising phase of the July 2000 GLE, the spectrum derived from neutron monitor observations is best fitted by a shock acceleration spectral form. In contrast, the spectrum at the peak and declining phases is best fitted by a stochastic acceleration spectral form. These results indicate that at least two processes accelerated protons to relativistic energies: (1) a shock driven by a coronal mass ejection (CME) and (2) a stochastic process associated with magnetic reconnection. For each phase of the

15 April 2001 GLE, the spectrum derived from neutron monitor observations is best fitted by a shock acceleration spectral form. This implies that protons were accelerated to relativistic energies by a CME-driven shock. The 20 January 2005 solar eruption produced the highest intensity of relativistic solar particles since the famous event on 23 February 1956. For each phase of the January 2005 GLE, the spectrum derived from neutron monitor observations is best fitted by a stochastic acceleration spectral form. This result suggests that a stochastic process cannot be ruled out as a mechanism for accelerating protons to relativistic energies for this solar event.

In summary, the major finding of this study indicates that, along with CME–driven shocks, sites of magnetic reconnection in the solar corona are a potential source of relativistic protons that give rise to GLEs.

ACKNOWLEDGEMENTS

Completing a PhD is a truly unique experience and this would have not been possible without the aid and support of the following people. I must first express my sincere thanks to my supervisors, Dr. Kelvin Michael, Dr. Marc Duldig and Dr. John Humble for their guidance, patience, meticulous attention to detail and encouragement throughout.

I am grateful to the Australian Antarctic Division for providing me with the resources, magnificent work environment and an Australian Antarctic Science Scholarship, which allowed me to complete my PhD in a most wonderful manner. I have also been the recipient of an Australian Post Graduate Award, for which I am extremely grateful.

Over the years I have enjoyed the aid and friendship of several colleagues at the Australian Antarctic Division and I would particularly like to thank Andrew Klekociuk, Damian Murphy, Lloyd Symons, Gary Burns, John French, Ray Morris, Danny Ratcliffe, John Innis, and Judy Whelan for their valued opinions and assistance.

Thanks to my parents John and Grace Bombardieri for their foresight and vision in choosing Tasmania as the place to achieve your dreams. I would also like to thank my father and mother in-law Giuseppe and Angela Attuoni for their love and support over the many years of my academic career.

A special thanks to my sister Deanna Bombardieri who was there for me from the very beginning.

Finally, to my wife Anna and children Luke and Julia for their love and support and for being there during those difficult times.

TABLE OF CONTENTS

LIST OF TABLES

LIST OF FIGURES

LIST OF ABBREVIATIONS

ACE	Advanced Composition Explorer
CELIAS	Charge, Element, and Isotope Analysis System ((*SOHO* spacecraft)
CORONAS	Complex Orbital Near-Earth Observations of Solar Activity
DGRF	Definitive Geomagnetic Reference Field
EIT	Extreme Ultraviolet Imaging Telescope (*SOHO* spacecraft)
ESA	European Space Agency
CME	Coronal Mass Ejection
GLE	Ground Level Enhancement
GOES	Geosynchronous Operational Environmental Satellites
GRS	Gamma-Ray-Spectrometer (*Yohkoh* spacecraft)
GSE	Geocentric Solar-ecliptic (co-ordinate system)
GSM	Geocentric Solar-Magnetospheric (co-ordinate system)
HEPAD	High Energy Proton and Alpha Detector
HXS	Hard X-Ray-Spectrometer (*Yohkoh* spacecraft)
IGRF	International Geomagnetic Reference Field
IMF	Interplanetary Magnetic Field
IMP	Interplanetary Monitoring Platform
LARC	Laboratorio Antartico de Radiacion Cosmica
LASCO	Large Angle Spectrometric Coronagraph Experiment
NASA	National Aeronautics and Space Administration
NM	Neutron Monitor
NOAA	National Oceanic and Atmospheric Administration
RHESSI	Ramaty High Energy Solar Spectroscopic Imager
SOHO	Solar and Heliospheric Observatory
SONG	Solar Neutron and Gamma Ray Spectrometer (*CORONAS-F*)
STEREO	Solar TErrestrial RElations Observatory
TRACE	Transition Region and Coronal Explorer

INTRODUCTION

1.1 SOLAR ERUPTIVE EPISODES

A central question of solar physics concerns the mechanisms responsible for the production of relativistic protons which give rise to ground level enhancements (GLEs) in the cosmic ray flux. GLEs are sudden increases in the cosmic ray intensity recorded by ground-based detectors and are associated with large solar eruptive episodes. Relativistic protons produced from these solar events represent a direct sample of matter from some of the most energetic processes in the solar system (e.g., solar flares and coronal mass ejections (CMEs)). Solar flares (Figure 1.1, *left*) are enormous explosions which occur in the solar corona, while CMEs (Figure 1.1, *right*) represent vast structures of plasma and magnetic fields that are expelled from the Sun into the heliosphere (the region dominated by the solar wind momentum).

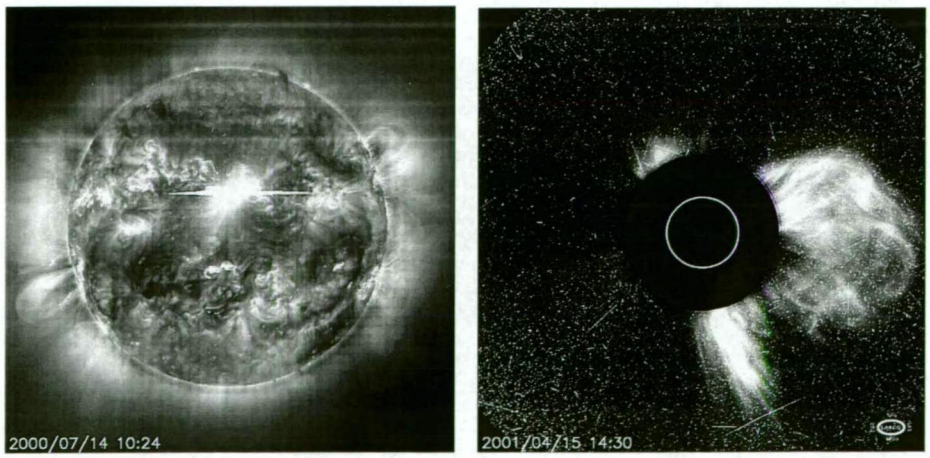

FIGURE 1.1: The 14 July 2000 solar flare as recorded by *EIT* on board *SOHO* at 171 Å (*left*). Source: http://soho.nascom.nasa.gov/hotshots/2001_04_15/c2f1.gif. The 15 April 2001 CME as recorded by the *LASCO/C2* coronagraph on board *SOHO* (*right*). Source: http://sci.esa.int/science-e-media/img/27/21997.jpg.

These energetic solar processes can convert in excess of 10^{32} ergs of magnetic energy into kinetic (accelerated particles) and thermal (heated plasma) energies on timescales of a fraction of a second to several tens of minutes.

Technological systems in space and on the Earth's surface are subject to adverse effects from these powerful solar events. The interaction of plasma generated from these solar phenomena with the Earth's magnetic field can result in electricity grid disruption, telecommunication disruption, satellite memory failures, solar cell degradation, navigation disruption and astronaut radiation hazards. Therefore, the consequences of major solar eruptive episodes can be quite dramatic, having significant economic as well as human impacts.

1.2 THE CURENT DEBATE

The relationship between flares and CMEs, and their role in accelerating particles to relativistic energies during major solar events remains a topic of ongoing research and debate. Solar energetic particle events (SEPs) have been divided, albeit controversially, into two distinct classes, impulsive and gradual events (Reames 1999). The two classes differ in their typical sizes (with gradual events yielding much larger particle intensities and fluences) and in the spatial distribution of their source regions (Tylka & Lee 2006).

Impulsive events originate from a narrow range of solar longitudes that are magnetically well-connected to the observer. For these events, Reames (1999) and others attribute particle acceleration to flare processes such as wave-particle interactions following magnetic reconnection. Impulsive events are characterized by low particle fluxes, high $^3He/^4He$ ratios (>0.1), high Fe charge states (~20) (attributed to the ionization process during magnetic reconnection) and high Fe/O ratios (~ 10 times that of normal coronal abundances) (Reames 1999). In contrast, for gradual events, particles are accelerated out of the ambient plasma over a broad range of longitudes by CME-driven shocks. These events are characterized by low $^3He/^4He$ ratios (<0.1), low Fe charge states (<14) and Fe/O ratios at coronal abundances (Reames 1999).

At energies of a few MeV per nucleon, impulsive and gradual events can be distinguished by compositional signatures. However, when the compositional signatures of gradual events are examined at energies above a few MeV per nucleon, at least some of the compositional distinction becomes blurred (Tylka & Lee 2006).

For example, some gradual events show Fe/O abundance ratios above 2.0 and mean ionic (e.g., Fe) charges close to those typically associated with solar flares. Cane *et al.* (2006) attribute such compositional characteristics to a direct flare component, questioning the validity of the two-class paradigm.

Many researchers consider the presence of a direct flare component in gradual events unlikely. Reasons include timing considerations (e.g., Kahler (1994); Debrunner *et al.* (1997); Bieber *et al.* (2004); Falcone *et al.* (2003)) and the very small source regions (e.g., Tylka *et al.* (2005)). Tylka & Lee (2006) suggest that since flares are often associated with fast CMEs, the CME-driven shocks could have access to flare particle seed populations from previous flare activity. They argue that it is the interplay of variables such as seed populations and shock geometry that provide the framework for understanding the compositional variability at high energies for gradual events.

The application of CME kinematic models (e.g., the flux-rope catastrophe model of Lin & Forbes (2000); see also Lin, Soon & Baliunas (2003) for a review of the various models) hints at the possibility that flares and CMEs might be manifestations of the same eruptive process. This suggests that it would be difficult to isolate the key signatures of relativistic particle acceleration.

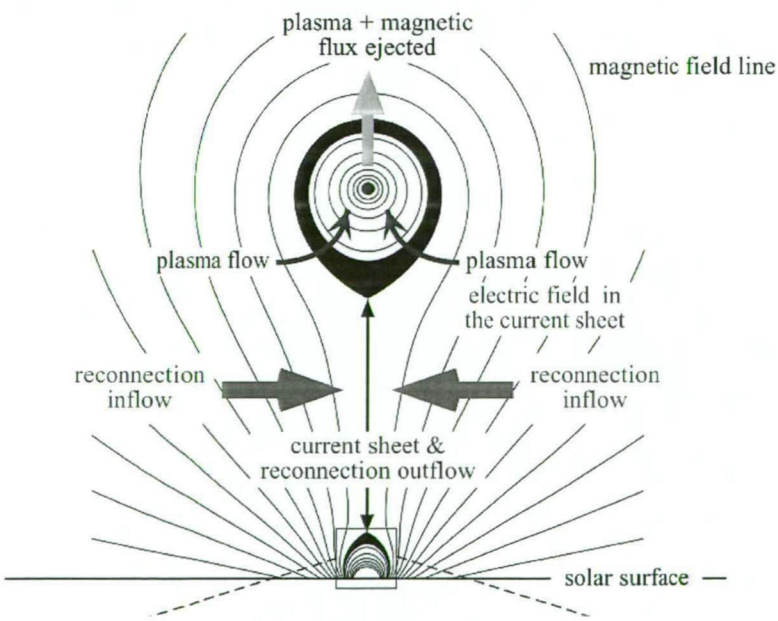

FIGURE 1.2: The standard model for large solar eruptions (Lin, Soon & Baliunas, 2003). The illustration depicts the two-ribbon flare model of Forbes & Acton (1996) and the CME configuration of Lin & Forbes (2000).

Figures 1.2 and 1.3 illustrate the basic idea of the eruptive flare model. Magnetic reconnection occurs in the current sheet produced by the stretching of the erupting solar magnetic field. The dissipating current sheet leads to the impulsive release of magnetic energy and the ejection of the magnetic flux rope (CME).

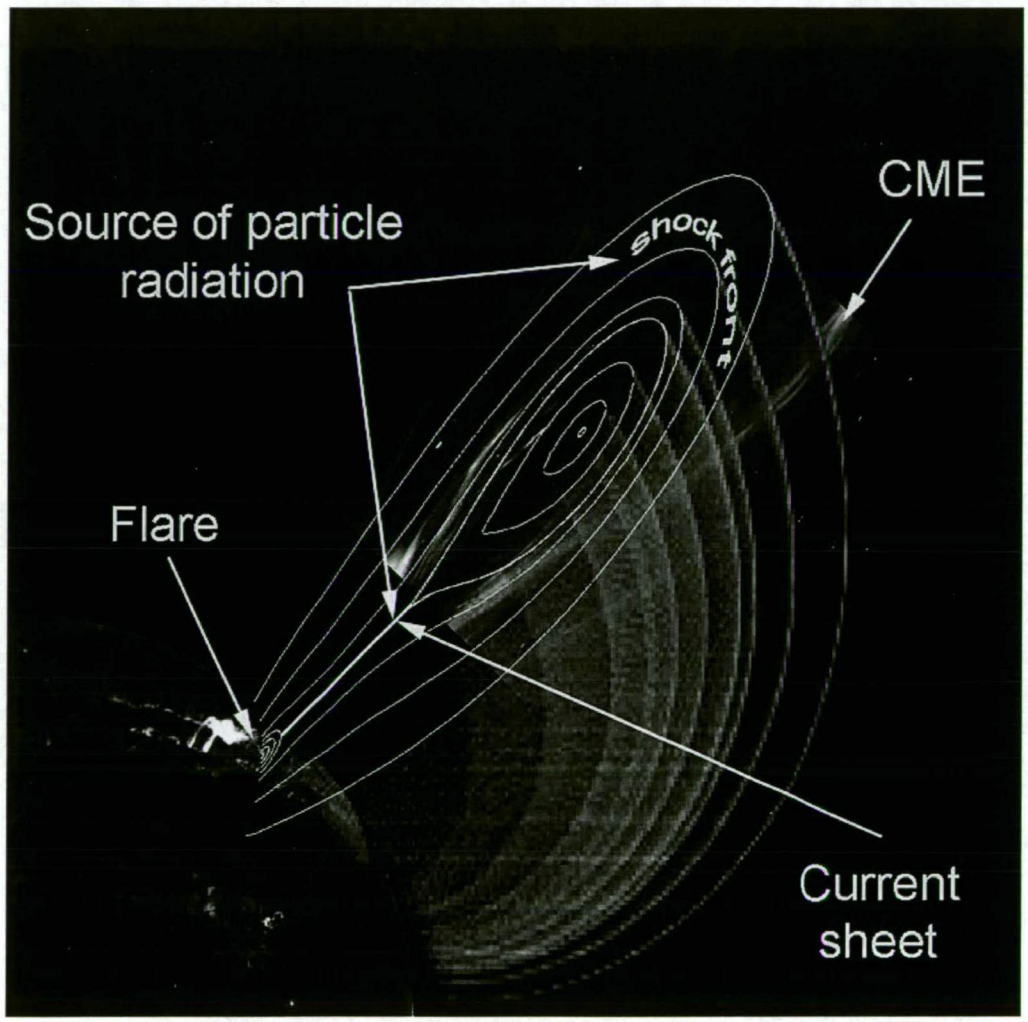

FIGURE 1.3: Illustration showing the Lin & Forbes (2000) standard model for large solar eruptions (*grey lines*) overlaying *SOHO* observations of an eruptive flare. Candidate sites for particle acceleration include CME-driven shocks and dissipating current sheets. Source: http://cfa-www.harvard.edu/press/archive.

In contrast to analysing the low-energy particle compositional characteristics of gradual events, the high-energy particle spectra of these events provide an alternative method for investigating particle acceleration at the Sun. The form of the energy spectra should be determined by the acceleration process. This provides a useful tool for probing the origin of the relativistic particles which produce GLEs.

1.3 AIMS OF THIS STUDY

The major aim of this study was to gain insight into the processes which accelerated the particles to relativistic energies and produced the 14 July 2000, 15 April 2001 and 20 January 2005 GLEs. For these GLEs, the intensities of relativistic particles (as measured by neutron monitors) were amongst the largest of the solar cycle 23. In particular, the 20 January 2005 GLE produced the highest intensity of solar relativistic particles since the famous GLE on 23 February 1956. Importantly, the solar eruptions which produced these GLEs were each associated with a large solar flare and CME.

Acquiring high-energy particle spectral characteristics for these major solar events provides an opportunity to investigate the mechanisms responsible for relativistic particle acceleration. This study used the global analysis technique for modelling GLEs to derive the particle arrival direction, pitch angle distribution and, importantly, the spectrum for each GLE event. The technique has been developed over many years (Shea & Smart 1982; Humble *et al.,* 1991, Cramp *et al.,* 1997) and is described in detail in Chapter 2.

Particle acceleration within the solar corona may occur in a variety of ways: direct particle acceleration in neutral current sheets by DC electric fields; stochastic acceleration through the process of resonant wave-particle interactions; and acceleration at coronal shocks. However, current theoretical models of direct particle acceleration via DC electric fields fail because they cannot explain the presence of energetic protons above a few MeV (Miller *et al.,* 1997). As a result, this study focussed only on the shock and stochastic acceleration processes, both of which are capable of accelerating protons to relativistic energies.

To determine the acceleration processes, analytical and numerical spectra representing shock and stochastic acceleration, respectively, were fitted to neutron monitor observations using a non-linear least squares method (section 2.2.3). The widely-utilised Ellison & Ramaty (1985) analytical expression was used to model diffusive shock acceleration. In the case of stochastic acceleration, two different spectral forms were used. The first incorporates an idealised pre-acceleration step via mono-energetic injection. The second incorporates a more realistic injection function using a pre-acceleration step via DC electric fields in a reconnecting neutral current sheet

Bombardieri *et al.* (2006, 2007) included low-energy spacecraft observations of proton intensities in spectral fits to determine the mechanism/s responsible for relativistic particle acceleration for the 14 July 2000 and 15 April 2001 solar events. However, interplanetary processes such as pitch angle scattering (due to resonant interactions and small-scale magnetic inhomogeneities) and magnetic cloud structures can affect the propagation of low-energy protons en-route to Earth. In addition, for major solar events where a CME-driven shock is generated, streaming particles become trapped near the shock by self-generated Alfvén waves (i.e., streaming-limited intensities), flattening the spectra of escaping particles at low energies (Reames 1999). Because the gyroradii of relativistic protons ≥450 MeV are at least equal to or greater than the coherence length of interplanetary magnetic field turbulence, they are less likely to be affected by interplanetary transport effects. To minimise these effects, analytical and numerical representations of shock and stochastic acceleration respectively were only fitted to neutron monitor energies (≥450 MeV). This allowed for a more accurate determination of the acceleration process. In addition, the effect of velocity dispersion on relativistic protons (i.e., 400 MeV to 10 GeV) is less than the 5-minute sampling time of neutron monitor data used in this thesis and thus can be neglected.

Spacecraft observations are able to acquire data at wavelengths relevant to energetic particle and plasma emissions in the solar corona and complement neutron monitor observations of high-energy particles. Solar cycle 23 has seen an unprecedented number of spacecraft coordinated to observe and measure variations in solar output (e.g., *SOHO, ACE, Wind, TRACE, RHESSI, GOES*). The availability of multiple spacecraft instruments allowed for a more complete analysis of interplanetary medium through which the particles propagated and particle acceleration process.

1.4 INSTRUMENTATION

For over fifty years neutron monitors have remained the state-of-the-art instrument for measuring intensity variations of 1 to 15 GV solar cosmic rays (Moraal, Belov & Clem, 2000). Several different styles of neutron monitors have been developed, including the 1957 International Geophysical Year (IGY) neutron monitor and the much larger NM-64 type detector designed by Carmichael (1968) for the International Year of the Quiet Sun (IQSY) in 1965 (Hatton 1971). The

majority of the world-wide neutron monitor network comprises NM-64s. The simultaneous detection of relativistic particles via this network provides a unique opportunity for determining the anisotropy, axis of symmetry of the particle arrival and, importantly, the spectral characteristics of large solar events. In particular, the latter characteristic is best determined from neutron monitor observations covering a range of magnetic latitudes.

Following a major solar eruption, particles which escape the coronal field into the interplanetary medium are guided via the interplanetary magnetic field (IMF). The trajectory of a particle in a magnetic field of strength B has a gyro-radius r given by:

$$Br = \frac{p}{Ze} \tag{1.1}$$

where p is the momentum of the particle and Ze is the particle's charge (in coulombs). The gyro-radius is proportional to the momentum, and the ratio p/Ze is a measure of the particle's resistance to the deviating effect of the field. Particle rigidity P is described in terms of a particle's momentum per unit charge,

$$P = \frac{pc}{Ze} \tag{1.2}$$

When energetic particles approach the Earth they are deflected by the geomagnetic field. To penetrate the geomagnetic field to the top of the atmosphere at a given position, the particle must have a rigidity which is greater than the geomagnetic cutoff for that location (i.e., the minimum rigidity below which a particle does not have access to a particular site on the Earth's surface). The values of the geomagnetic cutoff range from 0 near the geomagnetic poles to approximately 15 GV in equatorial regions (Moraal, Belov & Clem, 2000; Smart, Shea & Flückiger, 2000). Particles not deflected by the magnetic field enter the atmosphere and undergo multiple interactions, resulting in showers of secondary particles (Figure 1.4) which may reach ground level and be detected by neutron monitors.

Neutron monitors record predominantly the secondary neutrons from atmospheric cascades by counting the ionization events induced by these neutrons in appropriately-designed counters.

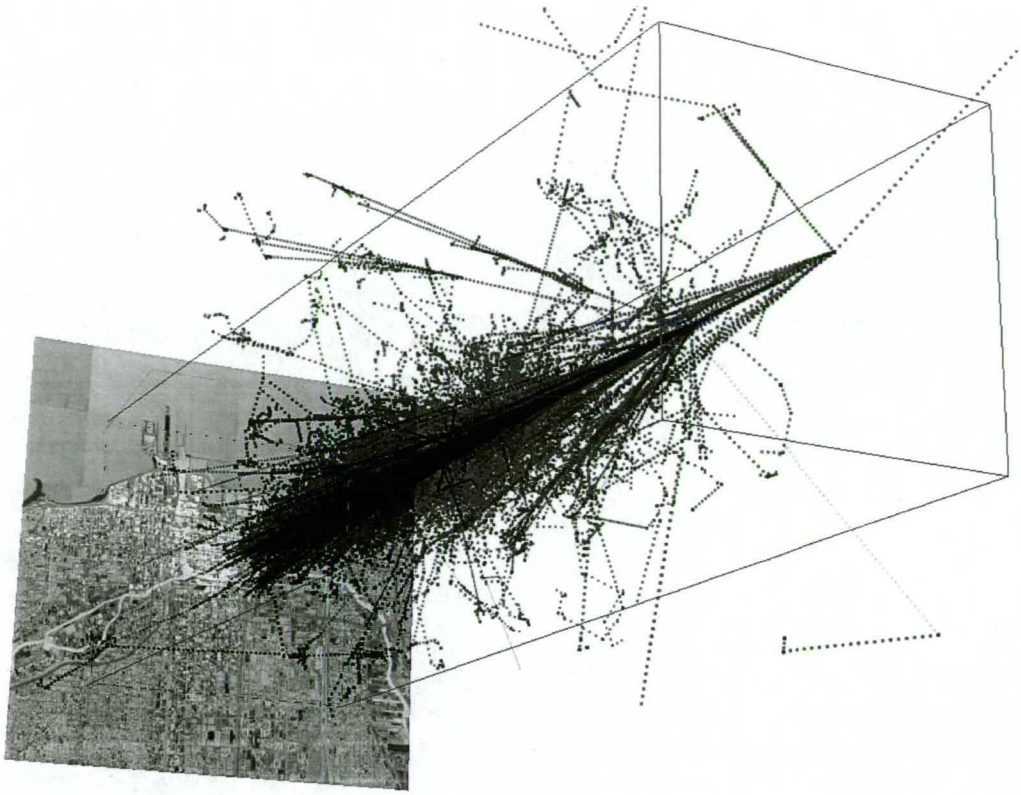

FIGURE 1.4: Representation of an incident relativistic proton colliding with atmospheric nuclei at approximately 20 km above the city of Chicago. Secondary particles include neutrons, electrons, positrons, muons and gamma rays. Source: http://astro.uchicago.edu/cosmus/projects/aires/

Most neutron monitors employ proportional counters filled with BF_3 in which the boron has been 90% enriched with the ^{10}B isotope. Secondary neutrons resulting from the cascade are captured by boron nuclei via the nuclear reaction:

$$^{10}B_5 + n \rightarrow {}^{7}Li_3 + \alpha \qquad (1.3)$$

Even though the secondary neutrons do not leave an ion trail in the proportional tube, the absorption of a neutron by a ^{10}B nucleus is followed by the emission of charged particles, which are detected by proportional counters registering pulses from ionized Li atoms and alpha particles.

Figure 1.5 illustrates the configuration of a NM-64 neutron monitor. Surrounding each proportional counter is the moderator, which acts as an inner reflector redirecting neutrons that have not interacted in the counter back towards the detecting medium. The moderator is generally composed of polyethylene as it provides for smaller local neutron production. Surrounding the moderator is the lead producer, which provides a thick, large-nucleus target for inelastic interactions whereby secondary neutrons are produced. The reflector surrounds the lead producer and reflects any escaped secondary neutrons back towards the counter. The reflector also absorbs low-energy neutrons produced in the atmosphere as well as in materials close to the monitor.

Proportional counters filled with ^3He offer an alternative to the standard BF_3 counters. He counters require higher pressures to improve their efficiency, otherwise their interaction cross-sections are too low. They have been carefully designed to have the same detection efficiency as a standard NM64 counter so that they may be inter-changed in a system. However, He counters have much higher temperature sensitivity and therefore require greater environmental temperature stability.

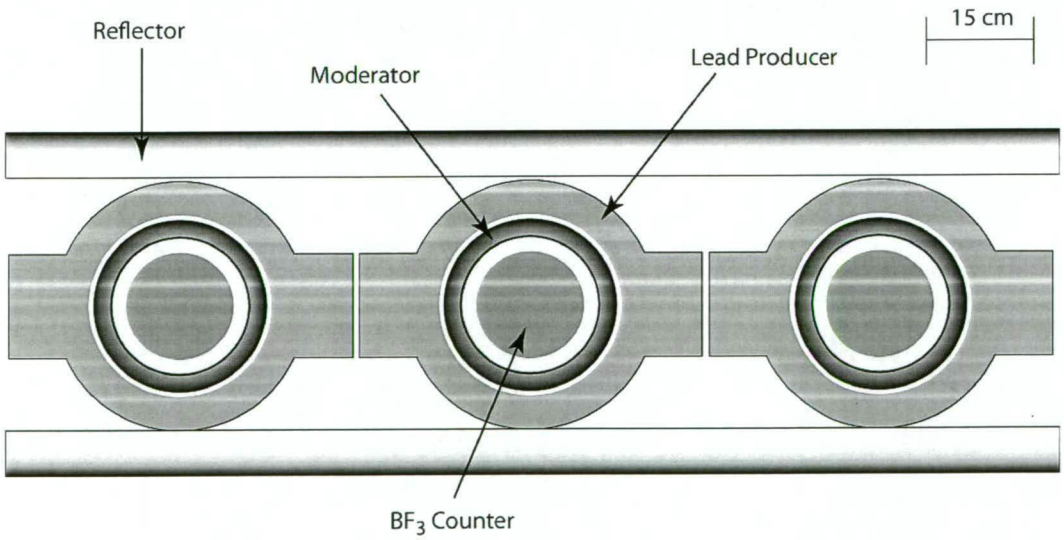

FIGURE 1.5: Schematic diagram of a NM-64 neutron monitor. The monitor consists of BF_3 counters surrounded by polyethylene moderators, a thick lead producer and outer reflector.

Due to their long term reliability and automated data acquisition, the world-wide network of neutron monitors plays a fundamental role in studies of solar cosmic ray physics. Data sets generated by this network form the basis of this study.

1.5 THESIS OUTLINE

The purpose of this study was to gain insight into the process/es which accelerated particles to relativistic energies producing the 14 July 2000, 15 April 2001 and 20 January 2005 GLEs. Chapter 2 presents a discussion of the various models used. This discussion first provides a review of the historical background of GLE modelling. Second, a detailed description is given of the global analysis technique used to model the arrival of relativistic particles at 1 AU. Third, descriptions of the theoretical shock acceleration and stochastic acceleration models used to analyse relativistic particle acceleration are presented. Chapter 2 is completed with a brief discussion of the non-linear least squares routine used to fit the acceleration spectra to neutron monitor observations. Chapters 3, 4, and 5 contain results from modelling the neutron monitor responses of the 14 July 2000, 15 April 2001 and 20 January 2005 GLEs, respectively. In addition, each of these chapters presents a discussion of the results of fitting the analytical/numerical shock and stochastic acceleration spectra to the neutron monitor observations. In Chapter 6 the results presented in Chapters 3, 4 and 5 are discussed in terms of interplanetary conditions at the time of each GLE, the impact of transport processes on low-energy proton intensities, and the source mechanisms responsible for relativistic particle acceleration. A conclusion is presented in Chapter 7, including discussions on improvements to the GLE model and additional research avenues that should be followed.

MODELLING

2.1 INTRODUCTION

This chapter is divided into two sections. Section 2.2 outlines the historical development of GLE modelling, beginning with the developments in understanding the interplanetary magnetic field and its role in the transport of particles from the Sun to the Earth. This is followed by a review of the developments leading to the analytical models which describe the trajectories of cosmic rays through the geomagnetic field, including several definitions of terms related to cut-off rigidities. The final part of section 2.2 describes both the technique used to model the neutron response to higher-energy protons, and the least-squares method used to efficiently analyse parameter space for optimum solutions.

Section 2.3 describes the shock and stochastic acceleration processes which can accelerate particles to relativistic energies. This is followed by a description of the analytical and numerical solutions of equations which describe these acceleration processes. Finally, the method used to fit shock and stochastic acceleration spectra to neutron monitor observations of high energy protons is described.

2.2 MODELLING GLEs

2.2.1 *Interplanetary Magnetic Field*

The systematic study of cosmic ray temporal variations under the direction of S. E. Forbush commenced in the late 1930s with the deployment of a global network of four Compton ionisation chambers. The first observation of relativistic solar particles with these ionisation chambers was made on 28 February 1942. The analysis and interpretation of these data were postponed during World War 2. In

1946, Forbush resumed his research and established that cosmic rays of solar origin were responsible for the increases in count rate of the detectors.

The next step in solar cosmic ray physics related to understanding the propagation of these relativistic particles through the interplanetary medium to the Earth and the mechanism/s which produced the anisotropies observed by ground-based instruments.

Initial investigations were hampered by a lack of knowledge of the IMF. Biermann (1957) and references therein proposed that the solar ejection of particles was a continuous process and not limited to individual eruptions such as solar flares. This was based on observations suggesting that molecular ions in type 1 comet tails experienced acceleration radially outward from the Sun. This led Biermann to conclude that solar corpuscular radiation is emitted continually from the Sun.

Parker (1958) in a seminal paper postulated that the plasma in interplanetary space is a supersonic extension of the solar corona and introduced the term 'solar wind'. He further suggested that the field remained attached to the rotating Sun, resulting in a large-scale pattern of an Archimedean spiral (Figure 2.1).

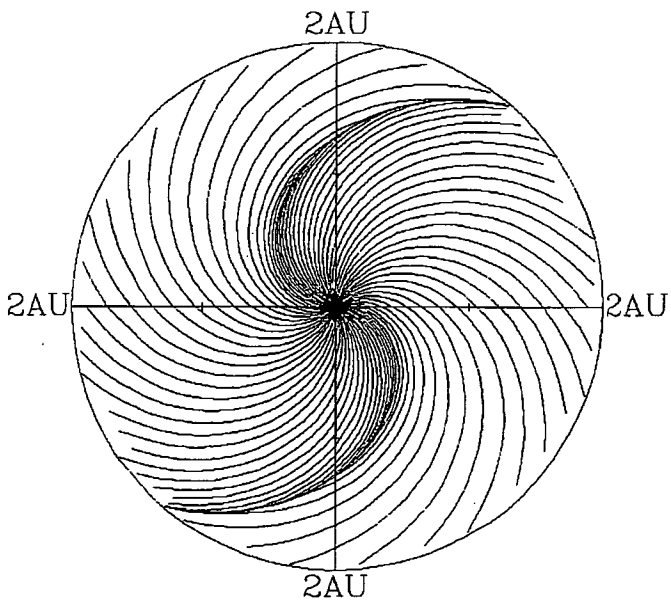

FIGURE 2.1: The spiral structure of the IMF on the equatorial plane. Source: Akasofu (2001)

In the case of an undisturbed field this resulted in an angle of ~60° between the lines of force and the radial direction at the orbit of Earth, based on a solar wind speed of ~300 km s^{-1}. The average quiet-time solar wind speed is now known to be

~400 km s^{-1} which produces an angle of ~45° between the magnetic field lines of force and the Sun-Earth line (Figure 2.2)

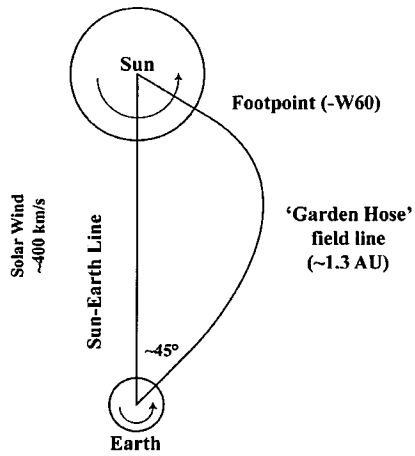

FIGURE 2.2: Schematic representation of the '*garden hose*' field line connecting the Sun to the Earth. Source: Duldig (1994).

Parker (1961) proposed that magnetic irregularities generated by turbulence and instabilities in the solar corona and interplanetary medium would be superimposed on this large scale structure (McDonald 2000). McCracken (1962*b*) was the first to provide verification (from neutron monitor observations) that the IMF was consistent with the geometry derived by Parker (1961). In-situ spacecraft measurements of the IMF in the mid 1960s provided additional evidence for a spiral configuration. Ness, Scearce & Seek (1964), using magnetic field observations from *IMP-1*, noted a sudden reversal in the IMF direction in which the magnetic intensity passed through zero. Further spacecraft observations revealed a well-defined sector structure with a polarity pattern repeating itself every 27 days. Wilcox, Hoeksema & Scherrer (1980) interpreted such observations as due to the presence of a heliospheric neutral current sheet separating two hemispheres of opposite polarity (Figure 2.3).

Near-Earth satellites, such as *ACE*, *WIND* and *SOHO*, continue to make direct measurements of the IMF, and the Ulysses spacecraft continues to probe the heliosphere at high solar latitudes (i.e., >70° from the ecliptic). These and other spacecraft (e.g., *STEREO*), will continue to provide important information on the characteristics of the IMF and the propagation of particles to Earth.

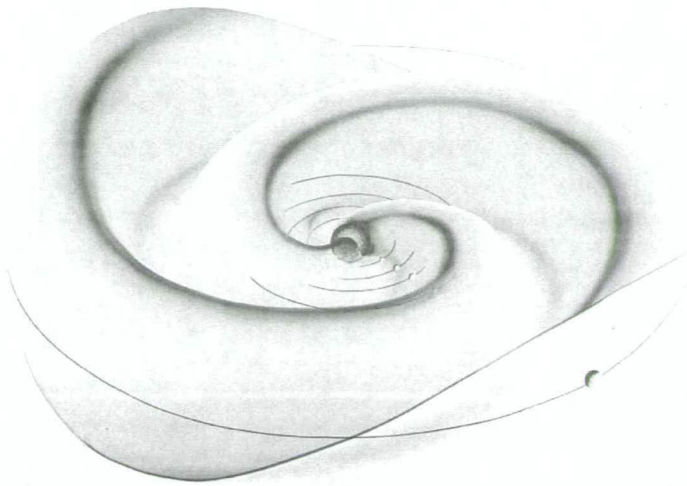

FIGURE 2.3: The three-dimensional structure of the Parker spiral, including the heliospheric current sheet. Source: http://wso.stanford.edu/gifs/helio.gif/

2.2.2 *Asymptotic Directions of Approach*

The motion of a cosmic ray particle in the vicinity of Earth is governed by the geomagnetic field. Using an accurate mathematical model of the Earth's magnetic field, it is possible to trace the path of a particle until it reaches the ground. Particles of different energy will follow different paths through the geomagnetic field.

Instead of considering energy, it is useful to use particle rigidity (units: volt), defined as the relativistic momentum per unit charge. Particles with equal rigidity will follow identical paths through a magnetic field. A cosmic ray particle travelling towards the Earth will follow the same path as a particle with opposite charge travelling away from the Earth anti-parallel to the cosmic ray arrival direction. It is therefore instructive to trace the trajectory of negative particles from points of interest on the Earth because this is far less computationally intensive than the full sky coverage required if working in the opposite sense.

Various models have been produced to calculate the path of an arriving particle through the Earth's magnetic field to an impact point on the Earth's surface. The first attempts to calculate the trajectories of solar particles through the geomagnetic field involved assumptions about arrival directions from the Sun that did not take into account the IMF as we know it today. Furthermore, models of the geomagnetic field were based on a simple dipole approximation (e.g., Firor (1954)). The advent

of more powerful computers in the early 1960s enabled more advanced geomagnetic field models to be developed, which resulted in more complex calculations of cosmic ray trajectories. The foundation of the modern method of trajectory calculations was developed by McCracken, Rao & Shea (1962) based on the numerical solution of the equations of motion (equation 2.1).

In a spherical coordinate system (r,θ,ϕ) the equations of motion for charged particles are

$$\left.\begin{aligned}
\frac{d\upsilon_r}{dt} &= \frac{e}{mc}\left(\upsilon_\theta B_\phi - \upsilon_\phi B_\theta\right) + \frac{\upsilon_\theta^2}{r} + \frac{\upsilon_\phi^2}{r} \\
\frac{d\upsilon_\theta}{dt} &= \frac{e}{mc}\left(\upsilon_\phi B_r - \upsilon_r B_\phi\right) - \frac{\upsilon_r \upsilon_\phi}{r} + \frac{\upsilon_\phi^2}{r\tan\theta} \\
\frac{d\upsilon_\phi}{dt} &= \frac{e}{mc}\left(\upsilon_r B_\theta - \upsilon_\theta B_r\right) - \frac{\upsilon_r \upsilon_\theta}{r} + \frac{\upsilon_\theta \upsilon_\phi}{r\tan\theta} \\
\frac{dr}{dt} &= \upsilon r \\
\frac{d\theta}{dt} &= \frac{\upsilon_\theta}{r} \\
\frac{d\phi}{dt} &= \frac{\upsilon_\phi}{r\sin\phi}
\end{aligned}\right\} \qquad (2.1)$$

where B_r, B_θ B_ϕ are known as explicit functions of (r,θ,ϕ) (i.e., the magnetic field components), υ_r, υ_θ, υ_ϕ are the particle velocity components, c is the speed of light, e and m are respectively the charge and mass of the particle and r is the radial distance from the centre of the Earth (Smart, Shea & Flückiger 2000).

When particle trajectories are calculated by this method, it is found that for a given rigidity there may be some trajectories that remain forever within the geomagnetic field or intersect the Earth's surface. These trajectories are termed *re-entrant* and indicate that the site is not accessible from space for that rigidity and arrival direction at the monitor (Figure 2.4 *left*). The accessible directions are known

as *asymptotic directions of approach* (Figure 2.4 *right*) and the set of rigidity-dependent accessible directions defines the neutron monitors *asymptotic cone of view* (McCracken 1962*a*).

To better resolve the responses of neutron monitors, Rao, McCracken & Venkatesan (1963) used a 9-direction trajectory calculation sequence to approximate the angular response of a neutron monitor (Smart, Shea & Flückiger 2000). Calculations are performed for trajectories of particles which have arrival directions at Earth's surface of 16° and 32° from the zenith (azimuths of 0°, 90°, 180°, 270°) as well as those arriving vertically. The increasing solid angle away from the zenith compensates for the decreasing flux caused by increased atmospheric attenuation; therefore each cone represents an approximately equal contribution to the total counting rate (Rao, McCracken & Venkatesan 1963). The use of the 9-direction approximation method produces a more accurate representation of the neutron monitor asymptotic cone of view compared to models using simple vertical approximation methods (e.g., Belov *et al.* (2001); Vashenyuk *et al.* (2003)).

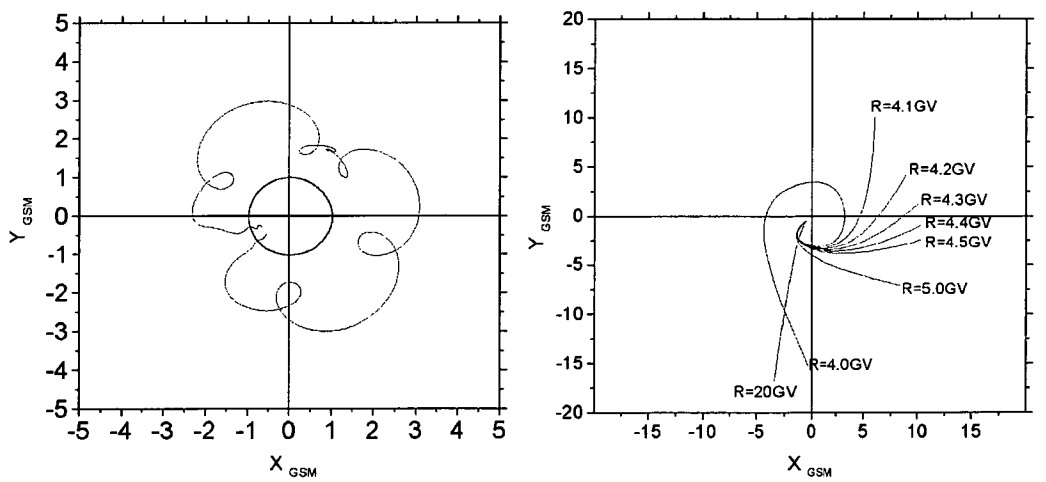

FIGURE 2.4: Illustration of re-entrant (*left*) and allowed (*right*) charged particles trajectories (vertical direction) from Lomnický Štít (Slovakia), which has a cut-off of ~4 GV. Re-entrant trajectory is calculated for a particle of ~3GV. GSM is the geocentric solar-magnetospheric coordinate system. Source: Kudela & Usoskin (2004).

The work of McCracken, Rao & Shea (1962) and McCracken (1962*a*) represented a watershed in modelling cosmic ray phenomena. Using high-order simulations (for that time) of the geomagnetic field, McCracken and his colleagues were able to calculate particle access to specific cosmic ray stations on the Earth to

describe the cosmic ray anisotropy. Furthermore, they also showed that the observed cosmic ray intensity could be well ordered by geomagnetic cut-off rigidities (Smart, Shea & Flückiger 2000).

During the mid-1960s it became clear that the solar wind caused significant distortion to the geomagnetic field, compressing the field lines on the day-side and producing a tail on the night-side (Ness, Scearce & Seek 1964). This asymmetry, as well as the effects of currents in the magnetopause and the neutral sheet in the geomagnetic tail, resulted in variations in the asymptotic viewing cones of neutron monitor detectors as the Earth rotated (Ahluwalia & McCracken 1965). Magnetospheric models were developed to account for a specified time (year, day, month, hour and geomagnetic disturbance). Whilst analyses of GLEs with these improved models (e.g., Gall, Jiménez & Camacho (1968); Gall, Jiménez & Orozco (1969); Gall, Smart & Shea (1971); Smart, Shea & Gall (1969)) incorporated a significant improvement in the calculation of the asymptotic cones of acceptance, they did not take into account the effects of the various current systems flowing within the magnetosphere, or variations in solar wind speed with time. It was not until the mid-to late 1980s that more sophisticated magnetospheric models, which provided a more realistic representation of magnetospheric processes, became available (Smart, Shea & Flückiger 2000).

2.2.3 *The Geomagnetic Field*

Current methods for calculating asymptotic directions are essentially the same as that of McCracken, Rao & Shea (1962) except for the incorporation of more advanced geomagnetic field models (Smart, Shea & Flückiger 2000). The software employed in the present study to calculate the asymptotic directions of approach was developed at the University of Bern by E. Kobel (Kobel 1989; Flückiger & Kobel 1990). The internal field is represented by the International Geomagnetic Reference Field (IGRF) model and the external field is represented by the magnetospheric model of Tsyganenko (1989).

The Internal Field

The geomagnetic field originates primarily within the planets interior, with a small part produced by currents in the ionosphere and the magnetosphere. The geomagnetic field in undisturbed form has an underlying offset dipolar configuration,

but is compressed on the day-side and expanded on the night-side as a result of interaction with the solar wind.

The internal component of the field may be represented by centred or eccentric dipole models, but a more accurate spherical harmonic series is usually employed. The IGRF is a series of models of the main geomagnetic field, each consisting of a set of spherical harmonic coefficients (Kodama 1992) for a series expansion of the geomagnetic potential, V and takes the form

$$V(r,\theta,\phi) = a\sum_{n=1}^{\infty}(a/r)^{n+1}\sum_{m=0}^{n}\left|g_n^m \cos m\phi + h_n^m \sin m\phi\right| P_n^m \cos(\theta) \qquad (2.2)$$

where g_n^m and h_n^m are Gauss coefficients describing the magnetic field, P_n^m are the Schmidt-normalised associated Legendre polynomials, a is the mean radius of the Earth, r is the radial distance from the centre of the Earth and ϕ is the geocentric co- latitude. In the dipole case, the expansion results in simple algebraic equations in (r,θ,ϕ) that can be repeatedly evaluated to find a solution for a trajectory initiated from a specified direction at a specific energy. As the complexity of the magnetic field expansion increases, the number of terms to be evaluated increases by n (Smart , Shea & Flückiger 2000).

IGRF coefficients are found by least-squares fitting of the model to datasets obtained from ground, marine, air and spacecraft measurements (Tsyganenko 1990). A set of coefficients has been calculated for each five-year period from 1945. The most recent IGRF available at the time of this study was a predictive model for 2005-2010 based on a secular variation to the parameters and measurements taken no later than one or two years prior to the epoch. Once data from this period have been collected, the coefficients will be revised and the new model will become the Definitive Geomagnetic Reference Field (DGRF) for that epoch. Linear interpolation between coefficients for different epochs and extrapolation from the most recent IGRF allows the determination of the model for any given time.

The External Field

The external magnetic field is the sum of the fields transported by the solar wind and those which the solar wind induces in the magnetosphere. The external field is

much less stable than the internal field, and the factors contributing to the external field are not completely understood. Therefore, additional external magnetic field models are required to account for the effects of various current systems flowing within the magnetosphere (Figure 2.5).

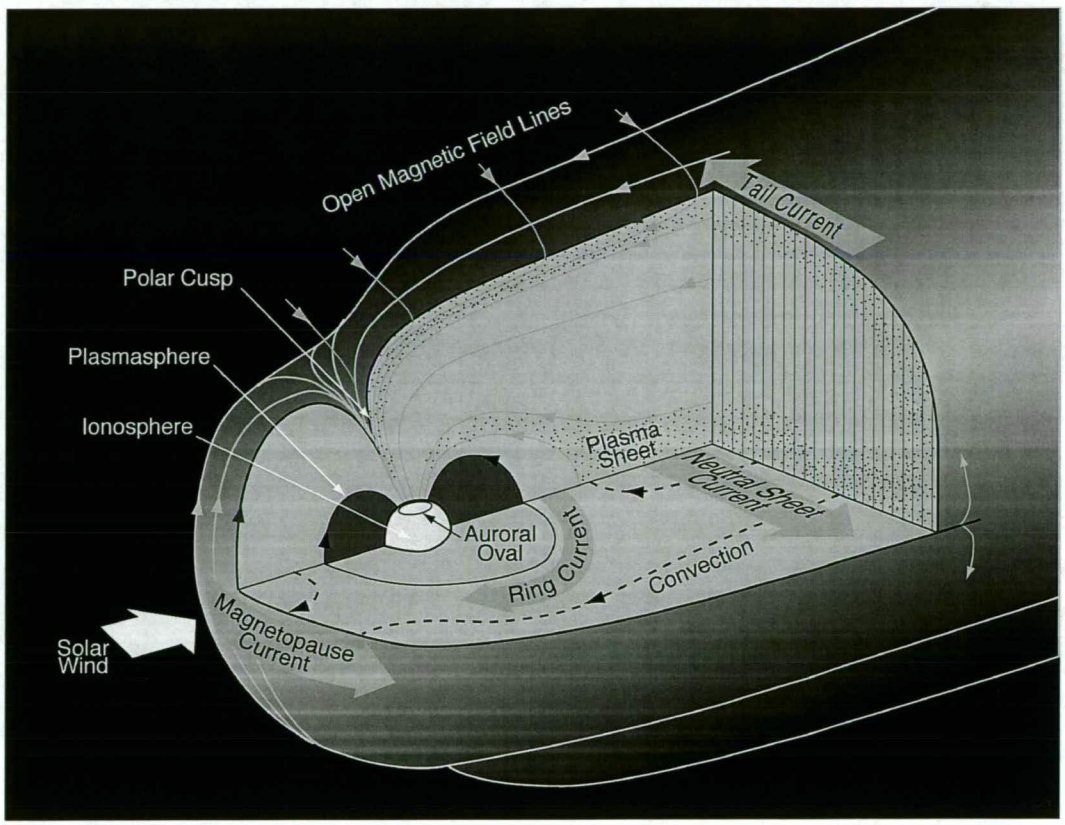

FIGURE 2.5: Schematic of the major magnetospheric currents systems, which include the magnetopause current, tail current, neutral sheet current and the ring current. Source http://www-solar.mcs.st-and.ac.uk/

The magnetopause shrinks, expands and erodes with varying degrees of connectivity to the IMF. The magnetopause current results from the deflection of solar wind plasma by the day-side magnetosphere. As this is a Lorentz force effect (the electromagnetic force on a charged particle moving in electric and magnetic fields), protons and electrons are affected oppositely resulting in a current in the dawn/dusk direction. The magnetopause current is closed either by the tail current or field-aligned currents through the day-side high latitude ionosphere.

The tail current sheet warps, bends and twists in response to wobbling at the geo-dipole and variations in the IMF. Tail currents are the result of a Lorentz force produced as the solar wind flows across open field lines in the magnetotail. The

currents are confined to the outer reaches of the tail as it is only there that a component of the magnetic field is perpendicular to the direction of flow of the solar wind plasma. The tail currents result in a dawn-to-dusk electric field across the magnetotail, effectively creating a magneto-hydrodynamic generator which extracts kinetic energy from the solar wind. The J x B force resulting from the currents confines the tail plasma to a sheet. It is across this sheet that the neutral sheet current flows as a discharge of the dawn to dusk electric field across the tail.

The injection of accelerated particles into the inner magnetosphere results in the formation of a storm-time ring current. The ring current is a gradient-drift effect. The magnetic field is strongest close to the Earth, so as particles gyrate along field lines from one hemisphere to the other they encounter a gradient in the magnetic field. This gradient causes the particles to flow around the Earth, with protons and electrons moving in opposite directions thus producing a clockwise current when viewed from the north.

These currents all contribute to the external magnetic field. Since the internal field strength decreases as r^{-3}, beyond about 10 Earth radii the geomagnetic field is dominated by the external components. The outer regions of the magnetosphere are also the most variable since the various currents are closely connected with highly-variable solar wind conditions. To achieve an accurate model of the magnetosphere, the mathematical representation must account for variations in these current systems.

2.2.4 *The Modified Tsyganenko (1989) magnetosphere model*

The Tsyganenko (1989) magnetosphere model (Figure 2.6), hereafter referred to as TY89, takes into account the effect of warping the tail current sheet in two dimensions due to the geo-dipole tilt, as well as spatial variations of the current sheet thickness along the Sun-Earth and dawn-dusk directions. The three main components used to construct the TY89 model are the magnetopause current, the neutral sheet current, and the ring current. TY89 contains 26 input parameters to allow the user to simulate specific magnetospheric conditions. Six levels of geomagnetic activity can be specified (Kp 0 to 5). The model is valid for geocentric distances up to 70 Earth radii.

For this study, improvements to the geomagnetic field model include the addition of a Dst index parameter to account for larger geomagnetic disturbances (Boberg *et al.*, 1995). The Dst index essentially monitors ring current field

variations. The addition of this parameter enables a more accurate determination of the asymptotic cone of view of a neutron monitor.

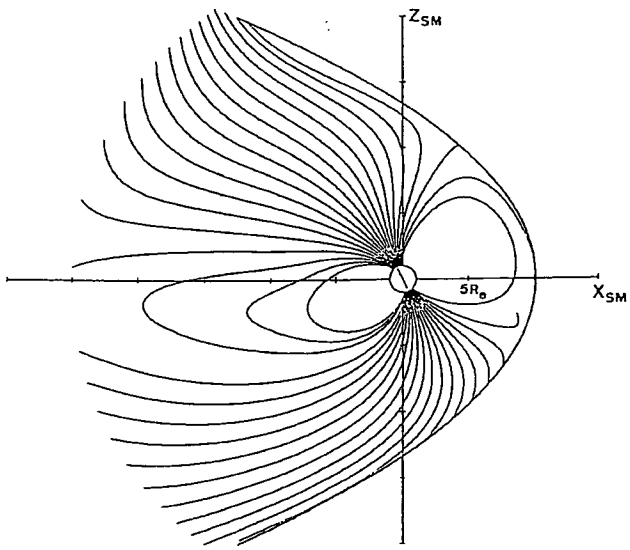

FIGURE 2.6: Schematic of the geomagnetic field topology derived from the Tsyganenko (1989) magnetospheric model. The field is projected on the X_{GSM}, Z_{GSM} plane. Source: Smart, Shea & Flückiger (2000) (originally from Flückiger & Kobel 1990).

Cosmic ray trajectories are traced through the magnetic field by numerical integration of the differential equation of motion (equation 2.1). The integration method of Stoer & Burlirsh (1980) is used, as it is faster than the Runge-Kutta method. Input parameters are date, time, Kp and Dst (level of geomagnetic disturbance), location on Earth and arrival direction at or near the Earth's surface. From this information, the direction of approach and the entry point at the magnetopause can be calculated. Cut-off rigidities are obtained by performing trajectory calculations systematically through the rigidity spectrum.

Asymptotic directions of approach are calculated using the full cone of view of the neutron monitor. This is achieved by using the nine-direction approximation method as described in section 2.2.2. Calculations begin at 20 GV with rigidity step-size dependant upon the particular station and decreasing to a minimum of 0.1 GV as the geomagnetic cut-off is approached. For stations with geomagnetic cut-off above the atmospheric cut-off (~1 GV) calculations continue through the penumbral region to the point below which all trajectories are forbidden. This is often termed the Störmer cut-off rigidity. Calculations are terminated at 1 GV for stations with Störmer cut-offs below this rigidity (Cramp 1996).

2.2.5 *Cutoff Rigidity Terminology*

Knowledge of the threshold rigidities for cosmic ray particles arriving at different geographic locations on the globe is of great importance in the study of the spectrum of solar cosmic rays. The path of a cosmic ray particle through the geomagnetic field is dependent upon its rigidity and direction of motion. As a consequence there are minimum rigidities below which particles do not have access to particular sites on the Earth's surface. These are known as geomagnetic cut-off rigidities (as defined in section 1.4). The vertical cutoff at the geomagnetic equator is ~17 GV and decreases to almost zero at the poles. In order to determine geomagnetic cut-offs it is necessary to systematically calculate the trajectories of arriving particles as a function of rigidity.

Re-entrant trajectories (see section 2.2.2) are combinations of rigidity and arrival directions which are not accessible at the surface location from outside the Earth's magnetic field. Considering one arrival direction at some point on Earth and calculating a set of trajectories at decreasing rigidities, there comes a point where the first re-entrant particle is encountered. The rigidity at which this transition occurs is called the *upper cut-off rigidity*, P_U. At lower rigidities there may be some re-entrant and some allowed trajectories until a rigidity is reached below which all trajectories are re-entrant. This is known as the *lower cut-off rigidity*, P_L. The region between allowed and forbidden trajectories is known as the *penumbra*. Some low-latitude stations do not exhibit a penumbral region in their asymptotic cones of view, so that P_U is equal to P_L.

For stations with a penumbral region it is useful to define the effective geomagnetic cut-off rigidity, P_C, which is defined such that if all trajectories above P_C are allowed and trajectories below it are re-entrant, the resulting count rate of a neutron monitor would be equal to the actual count rate. The effective geomagnetic cut-off rigidity may be calculated as a linear average of allowed rigidity intervals in the penumbra or from functions weighted by the particle spectrum and/or detector response. In the case of a linear average, this would have the form of

$$P_c = P_u - \sum_{P_L}^{P_U} \Delta P(allowed) \tag{2.3}$$

where the trajectory calculations were performed at rigidity intervals of ΔP and only allowed trajectories are included in the summation. The above definitions for P_U, P_L and P_C follow the conventions set down by Cooke *et al.* (1991) and are described in detail in Cramp (1996).

Some sites have effectively a zero geomagnetic cut-off. At such sites atmospheric interactions determine the threshold rigidity for access. As particles propagate through the atmosphere their kinetic energy is reduced as a result of interaction with atmospheric nuclei. Particles must therefore have sufficient energy to penetrate the atmosphere in order to generate a neutron monitor response. The *effective atmospheric cut-off* is defined as the energy (rigidity P_{atm}) below which particles do not make a significant contribution to the count rate of a ground-based detector. This will depend on the flux of arriving relativistic particles but is generally ~450 MeV (~1 GV in terms of rigidity). It is important to note that P_{atm} depends on altitude and is somewhat lower at sites such as South Pole (2820 m) when compared to sites located at sea level.

2.2.6 *Atmospheric Corrections*

The response of a neutron monitor varies with altitude due to variations in atmospheric pressure. For example, a sea-level neutron monitor will record a smaller number of secondary neutrons compared to a monitor at higher altitude. This is due to increased atmospheric depth and therefore increased atmospheric particle absorption.

The GLE modelling procedure requires that observed increases at each station be directly comparable. This is achieved by applying suitable pressure corrections to the data so that all neutron monitors have their count rates corrected to a standard atmospheric depth (equatorial sea-level).

The attenuation length represents the *e*-fold absorption of particles by the atmosphere. This depends on the spectrum of particles and, as a result, the attenuation lengths of galactic and solar cosmic rays are different. Since both galactic and solar cosmic ray particles are present during a GLE, a method utilizing the attenuation length of both populations is required.

The attenuation length for galactic cosmic rays λ_g is derived from the barometric correction coefficient, β, for a given station,

$$\lambda_g = \frac{1}{\beta} \tag{2.4}$$

This value is used to correct data to standard atmospheric pressure at the station. The attenuation length for solar particles λ_f can vary throughout a GLE and is generally calculated for each time interval. This method compares the response at two stations at different altitudes but with essentially the same viewing directions. Pairs of neutron monitor stations used in this study include Mt Wellington and Hobart or Mt. Washington and Durham (see Wilson *et al.* (1967) for a description of the procedure by which the calculation is made).

The relationship between the intensity at sea level and altitude is given by

$$N_s(sl) = N_s(alt)exp(-\alpha\Delta p)$$

$$N_g(sl) = N_g(alt)exp(-\beta\Delta p) \tag{2.5}$$

where N_s and N_g are the count rates arising from the solar and galactic particles, respectively, *sl* represents the sea level component, *alt* represents the altitude, α and β are the pressure coefficients for solar and galactic cosmic ray particles respectively, and Δp is the pressure difference between stations that are being considered. These relationships lead to

$$\frac{\Delta N_s(alt)}{\Delta N_s(sl)} = \exp\left[(\alpha - \beta)\Delta_p\right] \tag{2.6}$$

where ΔN_s is the observed percentage increase, defined as

$$\Delta N_s = \frac{N_o - N_g}{N_g} \times 100 \tag{2.7}$$

and $N_o = N_s + N_g$ (i.e. the total observed count rate). If β is known then α may be determined through equation 2.6.

McCracken (1962*a*) showed that the fractional increase in counting rate corrected to a standard pressure is

$$F = \left\{ \frac{C_E}{C_0} \exp\left(\frac{\delta p}{\lambda_f} \right) - \exp\left(\frac{\delta p}{\lambda_f} \right) \right\} \exp\left(\frac{p_0 - p}{\lambda} \right) \tag{2.8}$$

where C_0 and p_0 are the mean counting rate and pressure prior to the GLE increase, C_E and $p_0 + \delta p$ are the counting rate and pressure at some time during the GLE event, p is the standard pressure, λ_f is the attenuation length α^{-1} and λ is the attenuation length derived from β and α from the relationship

$$\lambda = \frac{1}{\alpha - \beta} \tag{2.9}$$

Equation 2.8 can be used to correct the fractional increase observed at an altitude station to sea-level pressure. In this case the equation becomes

$$\Delta N(SL) = \Delta N \exp\left(\frac{p - p_{SL}}{\lambda} \right) \tag{2.10}$$

where ΔN is the observed percentage increase at the station; $\Delta N(SL)$ is the corrected increase; p is the pressure at the station in g cm^{-2}; p_{SL} is the atmospheric pressure at equatorial sea-level (i.e., 1033 g cm^{-2}) and λ is the attenuation length as described above (Cramp 1996).

2.2.7 *Modelling the Neutron Monitor Response*

The global method for modelling the solar cosmic ray ground level response by neutron monitors has been developed over many years (Shea & Smart 1982; Flückiger & Kobel 1990; Humble *et al.,* 1991) and is described in detail by Cramp (1996) and Cramp *et al.* (1997). This method employs a least-squares fitting technique to determine the axis of symmetry of the particle arrival, the spectrum and the anisotropy of the high-energy solar protons that give rise to the increased neutron monitor response. Furthermore, the use of a least-squares package allows one to

efficiently analyse parameter space and derive an optimal solution for each of the time intervals considered. However, for the technique to work effectively, data are needed from neutron monitors at a range of locations around the globe. A range of cut-off rigidities (geomagnetic latitudes) allows the determination of spectral characteristics, whilst a range of latitudes and longitudes are necessary to determine the extent of anisotropy.

The response of a neutron monitor to particles arriving at the top of the atmosphere above a site is modelled using the following form (Cramp *et al.*, 1997)

$$\frac{\Delta N}{N} = \frac{1}{9}\sum_{(\theta,\phi)=1}^{9} \frac{\sum_{P_{min}}^{P_{max}} Q_{(\theta,\phi)}(P)\, J(P)\, S(P)\, G(\alpha)\, \Delta P}{\sum_{P_{min}}^{\infty} Q_{(\theta,\phi)}(P)\, J_0(P)\, S(P)\, \Delta P} \tag{2.11}$$

where

ΔN is the count rate increase due to solar cosmic rays corrected to sea level;

N is the pre-event baseline count rate due to galactic cosmic rays;

P is the particle rigidity (GV);

P_{min} is the lowest particle rigidity considered in the analysis;

P_{max} is the maximum particle rigidity;

Q is 1 for accessible arrival directions, 0 otherwise;

J is the solar proton flux;

J_0 is the interplanetary differential nucleon flux adjusted for the level of solar cycle modulation;

S is the neutron monitor yield function;

G is the pitch angle distribution of the arriving solar protons;

Λ, Ψ represent the latitude and longitude of the asymptotic viewing direction associated with (θ,ϕ) and rigidity P;

$\cos\alpha = \sin\Lambda(P)\sin\theta_s + \cos\Lambda(P)\cos\theta_s\cos(\Psi(P)-\phi_s)$;

(θ_S,ϕ_s) is the axis of symmetry of the pitch angle distribution.

P_{min} in the calculation is the lowest allowed rigidity as defined in section 2.2.5, except where this is less than the cut-off due to atmospheric absorption, which is assumed to be 1 GV. For high-altitude polar sites (e.g., South Pole) this is not accurate as lower rigidity particles do have access to the sites. However, Cramp (1996) showed that the resulting errors in best fit parameters are insignificant. P_{max} is generally taken to be 20 GV unless there is evidence from surface or underground muon telescopes of significant fluxes of higher rigidity particles (as was the case for the 29 September 1989 GLE (Swinson & Shea 1990; Humble *et al.*, 1991). The asymptotic cone of view calculations define Q, which has a value of 0 for all forbidden directions above P_{min} and 1 otherwise.

Increases are modelled above the pre-event background arising from galactic cosmic rays taking into account the level of solar cycle cosmic ray modulation (Badhwar & O'Neill 1996). For each neutron monitor the background is determined by summing the response of the solar cycle-modulated cosmic ray nucleon spectrum J_0 and the neutron monitor yield function S over all allowed rigidities. This function is defined so that the response to galactic cosmic rays is 100 particles (cm^2 s sr $GV)^{-1}$ above 1 GV. The analyses presented in this study have been performed using the Debrunner *et al.* (1982) neutron monitor yield function. This yield function was calculated using a Monte Carlo approach and is considered to be one of the best available, particularly at low rigidities.

2.2.8 *Least-Squares Determination of Parameters*

The least squares package used for this study, *Gaushaus*, was written at the University of Wisconsin Computing Centre and released in their Supplementary Program Series (No. 603) in 1966. An iterative technique combining the Gauss (Taylor series) technique and the method of steepest descent is used to obtain the final parameters from a series of initial guesses. The least-squares method involves minimising the sum of squares of differences between observed data and values calculated using a model function. It is represented by

$$SS = \sum_{k=1}^{n} \left[Y_k - f(\bar{\theta}, \xi_k) \right]^2 \qquad (2.12)$$

where Y_k is the k^{th} observed data point, f is the model function, $\bar{\theta}$ is the set of parameters and ξ_k is a set of constraints appropriate to the k^{th} observation. For each iteration, a set of new parameters $\bar{\theta}$ are derived with the aim of decreasing the value of *SS*.

Gaushaus has three criteria for the termination of calculations. The first involves manually setting a maximum number of iterations at which calculations are terminated even though convergence may not have been achieved. The remaining two criteria are (i) sum of squares convergence and (ii) parameter convergence. If the sum of squares convergence criterion is ϵ_1, calculations will terminate when

$$\left| \frac{SS\left(\bar{\theta}^{i}\right) - SS\left(\bar{\theta}^{i-1}\right)}{SS\left(\bar{\theta}^{i-1}\right)} \right| < \epsilon_1 \tag{2.13}$$

where *SS* is defined as above, $\bar{\theta}$ is the set of parameter values and i, $i-1$ represent consecutive iterations. If the parameter convergence criterion is ϵ_2, calculations will terminate when

$$\left| \frac{\theta_j^{\,i} - \theta_j^{\,i-1}}{\theta_j^{\,i-1}} \right| < \epsilon_2, \text{ for all } \theta_j \tag{2.14}$$

where θ_j is the j^{th} parameter, j ranges from one to the number of parameters and i, $i-1$ represent consecutive iterations. If both ϵ_1 and ϵ_2 are set, calculations will terminate when either of these criteria are satisfied.

The output from *Gaushaus* includes the final function values, final parameter values and individual 95% confidence limits for each parameter. These confidence limits are based on a linear hypothesis. However, the main assumption of this error calculation is invalid as the model employed here is highly non-linear. For example, the spectral exponent is dependent on any change of slope parameter and the spectrum is also dependent on the particle arrival direction and pitch angle distribution due to the rigidity dependence of viewing directions. However, some attempt to estimate the errors can be made. It is only practical to consider one parameter at a time, while fixing the best fit values of all other parameters. The

significance of the change of the *SS* value gives a measure of the significance of the change in the parameters. This method is used in this thesis to estimate uncertainties in parameters.

The observed data points are the percentage increases recorded by neutron monitors. Clearly it is necessary to have at least as many stations as parameters. The model should accurately reproduce the observed increases, as well as produce null responses for those stations that did not record an intensity increase. Inclusion of data from stations with null responses places additional bounds on the spectra and anisotropy characteristics.

Weighted least squares

Errors in observed values may not be equal and, as a result, observations should not be treated equally in the minimisation of *SS*. It such cases it is usual to minimise a weighted sum of squares, WSS_N, where subscript N denotes fitting to neutron monitor data. The sum of squares represented by equation 2.12 is replaced by

$$WSS_N = \sum_{k=1}^{n} w_k \left[Y_k - f\left(\bar{\theta}, \xi_k\right) \right]^2 \tag{2.15}$$

where w_k is the weight assigned to the k^{th} observation, Y_k. In the specific application of the weighted least squares method, the observed values Y_k are the actual percentage increases in count rate. The calculated function values, $f\left(\bar{\theta}, \xi_k\right)$, are the calculated increases from the model, given the input parameters $\bar{\theta}$. The weight applied to each observation is defined as

$$w = \sqrt{\frac{background + increase}{background}} \times 100 \tag{2.16}$$

where the background is the average count rate prior to the GLE and increase is the increase in count rate above the background level. The value of the background is obtained from an average over one hour of data, but scaled to the same time interval over which the increase is recorded (Cramp 1996).

2.2.9 *Pitch angle distributions*

The propagation of particles through the interplanetary medium results in a distribution of pitch angles which can be described using a functional form. Formally, the particle pitch angle $\alpha(\theta,\phi)$ is defined as the angle between the axis of symmetry of the particle distribution (θ_s,ϕ_s) and the asymptotic direction of view at rigidity P associated with the arrival direction (θ,ϕ). The most widely-used functions have been cosine or Gaussian relationships. However, Smart & Shea (1990) found that significantly better results could be obtained with an exponential function of the form

$$G(\alpha) = exp\left[\frac{-0.5(\alpha - \sin\alpha\ \cos\alpha)}{A}\right] \tag{2.17}$$

The pitch angle distribution used in this study is a simplification of the exponential form described by Beeck & Wibberenz (1986). It has the functional form

$$G(\alpha) = exp\left[\frac{-0.5(\alpha - \sin\alpha\ \cos\alpha)}{A - 0.5(A-B)(1-\cos\alpha)}\right] \tag{2.18}$$

where A and B are variable parameters (Cramp *et al.*, 1997).

The pitch angle distribution function represented by equation (2.18) can be further modified to allow for bi-directional flow:

$$G'(\alpha) = G_1(\alpha) + C \times G_2(\alpha') \tag{2.19}$$

where G_1 and G_2 are of the same form as in equation (2.18) with independent parameters A_1, B_1, A_2 and B_2; $\alpha' = \pi - \alpha$; and C is the ratio of reverse-to-forward flux ranging from 0 to 1.

Reverse-propagating particles have opposite flow (pitch angles >90°). This can arise if particles initially travelling outward from the Sun encounter magnetic turbulence in the disturbed interplanetary medium beyond Earth's orbit, resulting in

the back-scattering of relativistic protons. Alternatively, bi-directional flow can be the result of particles arriving from the Sun along two different paths in a closed interplanetary magnetic loop configuration.

2.2.10 *Spectrum*

The form of the particle spectrum is related to the acceleration process. One advantage of the modelling technique used in this study is the ability to utilise various spectral forms, such as pure and modified power laws, as well as spectra based on theory (Ellison & Ramaty 1985), to achieve the best fit between observed and calculated responses. The Ellison & Ramaty shock spectrum is approximated by a power law with exponent $-\gamma-(1-\beta^2)(1+\delta\gamma)$ (Cramp 1996), where γ is the spectral index, β is the ratio of the particle speed to the speed of light and $\delta\gamma$ is an exponent modifier to account for a non-infinite shock interacting for a finite time. This form is referred to as the modified Ellison & Ramaty spectrum.

An empirical functional form that can be employed to fit the neutron monitor observations is

$$J_{\parallel} = K P^{-(\gamma-\delta\gamma(P-1))} \tag{2.20}$$

where $J_{\parallel}$ is the peak cosmic ray flux arriving from the Sun along the axis of symmetry of the pitch angle distribution. The parameters are the particle rigidity (P), the parallel flux at 1 GV (K), the power law exponent (γ) and the change of γ per GV ($\delta\gamma$), where a positive value of $\delta\gamma$ results in a spectrum that steepens with increasing rigidity. This functional form is referred to as the modified power law spectrum

2.3 MODELING PARTICLE ACCELERATION

Particle acceleration within the solar corona may occur in a variety of ways: acceleration at coronal shocks, either CME- or flare-driven; stochastic acceleration through the process of resonant wave-particle interactions; and direct particle acceleration in neutral current sheets by DC electric fields. Theoretical studies suggest that relativistic particle acceleration directly via DC electric fields is unlikely (Miller *et al.* 1997) and therefore, this process is not discussed further. The remainder of this chapter focuses on analytical and numerical solutions of equations

which describe shock and stochastic acceleration processes, both of which are capable of accelerating protons to relativistic energies.

2.3.1 *Shock Acceleration*

Astrophysical shocks have been invoked as mechanisms capable of accelerating particles to relativistic energies. Such shocks exist in a wide variety of astrophysical sites including supernova remnants, active galactic nuclei, extra-galactic radio jets and interplanetary shocks resulting from coronal mass ejections. Particle acceleration by collisionless shocks (i.e., non-linear disturbances that involve momentum and energy transfer between particles purely by plasma processes) has been the subject of numerous theoretical investigations for decades (for a review of the literature see Jones and Ellison (1991)).

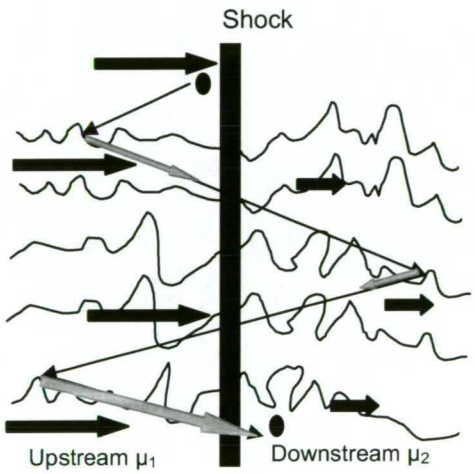

FIGURE 2.7: Schematic of the diffusive shock acceleration process showing a particle (*black circle*) moving back and forth across a shock (*thick black line*) and being accelerated. μ is the plasma flow speed indicated by the size of the black arrows. Note $\mu_1 > \mu_2$ and there is always a net gain in particle energy after a complete cycle. Energy gain is indicated by the grey arrows.

In collisionless shocks, charged particles gain energy via scattering due to magnetic field turbulence (Alfvén waves) back and forth between the converging upstream and downstream plasmas (Figure 2.7). This basic physical process, called diffusive or first-order Fermi shock acceleration, is the same in relativistic and non-relativistic shocks (Ellison & Double 2002). Most collisionless shocks are non-relativistic, i.e., the flow speed of the unshocked plasma in the reference frame at rest with the shock, is much less than the speed of light (Ellison and Double 2002).

The Diffusion-Convection Equation Describing Shock Acceleration

If the distribution function in space and scalar momentum of accelerated particles $f(x, p)$, is considered to be isotropic to the first order, then the steady-state Boltzmann equation describing the transport of particles with $\upsilon > u$ (where υ is the individual particle velocity and u is the plasma flow velocity) can be written in the form of a diffusion-convection equation (Jones & Ellison 1991)

$$\frac{\partial}{\partial x}\left[uf(x, p) - \kappa \frac{\partial f(x, p)}{\partial x}\right] = \frac{1}{3}\left(\frac{\partial u}{\partial x}\right)\frac{\partial}{\partial p}[pf(x, p)] \tag{2.21}$$

where $\kappa = \kappa_{||}\cos^2\theta_{Bn} + \kappa_{\perp}\sin^2\theta_{Bn}$ is the diffusion coefficient in the direction normal to the shock, θ_{Bn} is the angle between the shock normal and the mean magnetic field, and $\kappa_{||}$ and $\kappa_{\perp}$ are the diffusion coefficients parallel and perpendicular to the magnetic field respectively (Jones & Ellison 1991).

From this equation, Axford, Lear & Skadron (1977) and Blandford & Ostriker (1978) established that a shock propagating through a region where particles gain energy by scattering freely between the converging upstream and downstream plasma flows (without influencing the shock structure), would produce a suprathermal population of particles described by a power-law momentum distribution function

$$f(p)d^3p \propto p^{-\sigma}d^3p \tag{2.22}$$

where $f(p)d^3p$ is the number density of particles in momentum space, p is the momentum and $\sigma = 3r/(r\text{-}1)$ is the spectral index, where r is the compression ratio of the shock ($r = u_1/u_2$, the ratio of the upstream and downstream plasma flow velocities).

Based on this, Ellison & Ramaty (1985) developed a corresponding diffusive-shock acceleration expression in the differential particle intensity domain, which is essentially a power law truncated with an exponential

$$\left(\frac{dJ}{dE}\right) \propto \left(\frac{dJ}{dE}\right)_0 \exp\left(-\frac{E}{E_0}\right) \tag{2.23}$$

where

$$\left(\frac{dJ}{dE}\right)_0 \propto n_{inj}\left(E_i^2 + 2E_i m_0 c^2\right)^{3/[2(r-1)]}\left(E^2 + 2Em_0 c^2\right)^{-(1/2)[(r+2)/(r-1)]} \tag{2.24}$$

and $(dJ/dE)_0$ is the differential particle intensity,

n_{inj} is the number density of seed particles injected far upstream of the shock,

c is the speed of light,

$m_o c^2$ is the proton rest mass energy,

E is the particle energy,

E_i is the particle injection energy,

r is the shock compression ratio.

The exponential turnover in equation (2.23) was incorporated to account for the various effects which might limit the number of particles accelerated to higher energies in an actual three-dimensional shock. These effects include the finite temporal evolution of the shock compared to particle acceleration times and the finite spatial distribution of the shock compared to particle diffusion lengths. In addition, particle acceleration is also thought to be less effective above the energy E_0 (*e*-folding energy) when proton intensities can no longer sustain the growth of resonant waves. This process leads to the leaking of high-energy particles from the acceleration region, thereby truncating the power law behaviour. Ellison & Ramaty (1985) found that for several large solar events the electron and proton spectra were consistent with predictions for diffusive-shock acceleration.

The Ellison & Ramaty (1985) diffusive shock acceleration equation, and variations thereof, have been extensively cited in the literature and widely used to model SEP acceleration (e.g., Lockwood *et al.* (1990); Mazur *et al.* (1992); Lovell, Duldig & Humble (1998); Tylka *et al.* (2000, 2001); Mewaldt (2005); Tylka & Lee (2006); Bombardieri *et al.* (2006, 2007)).

2.3.2 *Stochastic Acceleration*

Stochastic acceleration is broadly defined as any process in which a particle can gain or lose energy in a short time interval, but where the particle systematically gains energy over longer intervals of time (Miller *et al.* 1997). Energy from magnetohydrodynamic (MHD) turbulence is transferred to particles through the process of wave-particle resonant interactions. In such an interaction, a particle gyrating along the magnetic field follows and is accelerated by the electric field of an wave, which has a velocity much less than the particle. Alfvén waves are incompressible transverse oscillations which propagate along field lines with magnetic tension as a restoring force. They can be thought of as propagating wiggles in magnetic field lines. In gyro-resonant interactions, the oscillations are rapid enough so that the first adiabatic invariant of the particle is not conserved and the particle is scattered in pitch angle and is simultaneously energised (Miller 1991).

The origin of Alfvén waves is a topic of much conjecture. However, it is thought that they are generated at large wavelengths by plasma outflow jets created at magnetic reconnection sites or by large-scale magnetic field perturbations (Miller *et al.,* 1997; Priest & Forbes 2002). Magnetic reconnection refers to the breaking and reconnecting of oppositely- directed magnetic field lines in a plasma. Current sheets store magnetic energy by increasing the energy density of the magnetic field.

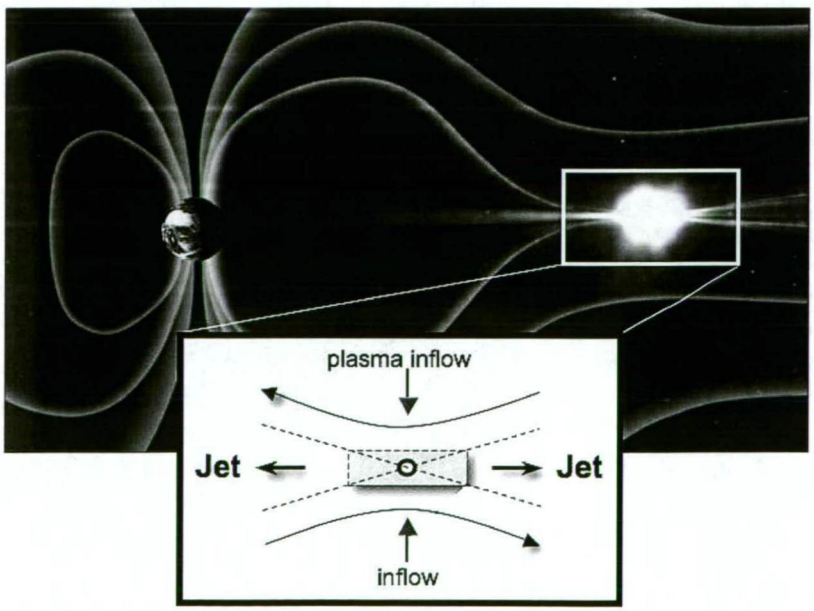

FIGURE 2.8: Schematic representation of the reconnection process at the Earth's magnetotail as observed by the *Cluster* spacecraft. Source: http://sci.esa.int/science-e-media/img/3a/Reconnection-scales.tiff/

Plasma instabilities can arise near strong current sheets, which are prone to collapse (dissipate). This results in magnetic reconnection, which rapidly converts stored magnetic energy into kinetic and thermal energy. High-velocity plasma outflow jets (Innes *et al.*, 1997; Miller *et al.*, 1997; Galsgaard *et al.*, 2005) are produced as a result of the magnetic reconnection process (Figure 2.8). Such jets represent a potential source of MHD turbulence which can initiate stochastic acceleration.

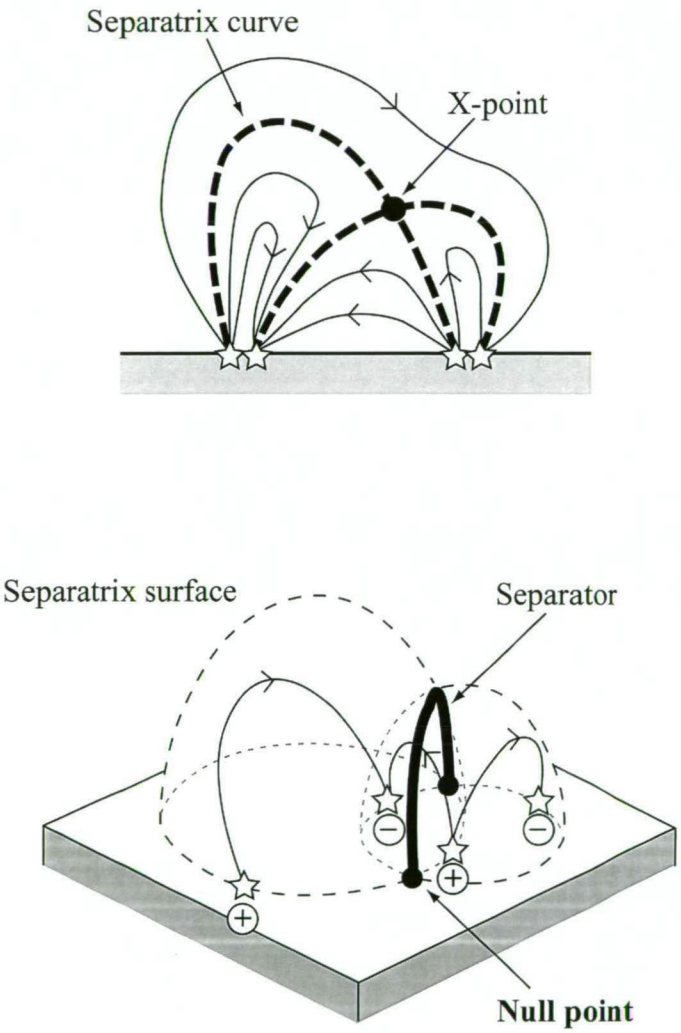

FIGURE 2.9: Schematic representation of photospheric footpoint topology. Current sheets are hypothesised to form at a separatrix curve in two-dimensions (*top*) and separatrix surface in three dimensions (*bottom*). Source: Priest & Forbes (2002)

Current sheets form due to gradients in the magnetic field which are created by a variety of mechanisms such as MHD instabilities and MHD motions. Figure 2.9 illustrates the complexity of current sheet topology in two and three dimensions. In two dimensions (Figure 2.9 *top*), the field is due to four sources of alternating sign in

a line, creating an X type magnetic null point where the magnetic field intensity, B, is zero. Emanating from the null point are four separatrix curves, which divide the plane into topologically-distinct regions. Current sheets are thought to occur at both the magnetic null (X) points and separatrix curves (Priest & Forbes 2002). In three dimensions (Figure 2.9 *bottom*), the field is due to four photospheric sources on a plane possessing two separatrix surfaces in the form of domes. The domes separate the volume into topologically-distinct regions, which intersect each other via a separator. Current sheets can form at both the separatrix surface (the 3D equivalent to the separatrix curve) and separator.

The magnetic reconnection process is ubiquitous in the solar corona and has been invoked as the main driver of solar eruptive episodes (Innes *et al.*, 1997; Priest & Forbes 2000 & 2002). Importantly, stochastic processes resulting from magnetic reconnection can accelerate particles to relativistic energies.

With the advent of the *RHESSI* spacecraft, there is now strong observational evidence supporting the importance of current sheets in major solar eruptive episodes (Ciaravella *et al.*, 2002; Ko *et al.*, 2003; Sui & Holman 2003; Webb *et al.*, 2003; Gary & Moore 2004; Sui, Holman & Dennis 2004, Lin *et al.*, 2005, Bemporad *et al.*, 2006).

Stochastic Acceleration: Solutions to the Fokker-Planck Equation

Stochastic acceleration initiated by processes associated with magnetic reconnection (e.g., MHD turbulence), can be described by either a diffusion equation in momentum space or a Fokker-Planck equation in energy space (equation 2.25). The Fokker-Planck equation describes the time evolution of the probability density function of the position and velocity of a particle. The diffusion equation is characterised by a momentum diffusion coefficient, whereas the Fokker-Planck equation displays the diffusive and convective nature of the stochastic acceleration process.

$$\frac{\partial N(E,t)}{\partial t} = \frac{1}{2}\frac{\partial^2}{\partial E^2}[D(E)N(E,t)] - \frac{\partial}{\partial E}[A(E)N(E,t)] - \frac{N(E,t)}{\tau(E,t)} + Q(E,t) \quad (2.25)$$

where,

$N(E,t)$ is the number density of particles as a function of energy and time;

$A(E)$ contains the systematic effect of stochastic acceleration and deceleration processes;

$D(E)$ contains the diffusive effects as a result of dispersion due to the systematic energy change rate;

τ is the energy-dependent escape time;

Q is the injection rate.

The Fokker-Planck equation has been solved analytically in the non- and ultra-relativistic domains (Ramaty 1979; Miller, Guessoum & Ramaty, 1990); however there is no analytical time-dependent solution (which describes both instantaneous and continuous injection) for the Fokker-Planck equation in the trans-relativistic domain.

Perez-Peraza & Gallegos-Cruz (1994) and Gallegos-Cruz & Perez-Peraza (1995) presented solutions to the Fokker-Planck equation (2.25) in the energy domain, based on the WKBJ (Wentzel, Karmer, Brilloun, Jeffery) numerical approximation method. The WKBJ method is a useful technique for solving differential equations (see Gallegos-Cruz & Perez-Peraza (1995) for a complete review of the technique). These solutions are valid over the entire energy range (i.e., non-relativistic, trans-relativistic, ultra-relativistic) for both time-dependent and steady-state conditions. Furthermore, Perez-Peraza & Gallegos-Cruz (1994) demonstrated that steady-state spectra obtained using the WKBJ method are in excellent agreement with steady-state spectra obtained by Miller et al. (1990), thereby providing confidence in the technique.

When the time evolution term in equation (2.25) is removed (i.e., $\partial N/\partial t$ is equal to zero), the general solution for the steady-state condition is written as equation (2.26) (equation (21) in Gallegos-Cruz & Perez-Peraza (1995))

$$N(E) \cong \frac{D^{1/4}(E)}{2a^{1/4}} \int_{E_0}^{E} \frac{q(E')}{D^{3/4}(E')} \exp\left(-R_1 - 2a^{1/2}R_2\right) dE' \qquad (2.26)$$

where,

$N(E)$ = particles per unit energy;

$D = (a/3)\,\beta^3\varepsilon^2$, where $a = (\delta+\alpha)\beta + (\alpha/3)\beta^{-1}$, δ is set to 1 s^{-1}, $\beta = v/c$,

ε = energy + proton rest mass energy and α is the acceleration efficiency (NB: here α does not represent the pitch angle distribution);

$q(E')$ is the injection spectrum;

R_1 and R_2 are analytical functions of energy

Stochastic Acceleration: Mono-Energetic Continuous Injection

A selective injection process is required to supply particles into the acceleration region where they are then re-accelerated to higher energies via resonating Alfvén wave–particle interactions. Equation (2.27) (equation (43) in Gallegos-Cruz & Perez-Peraza (1995)) incorporates an idealized pre-acceleration step via continuous mono-energetic injection at a characteristic supra-thermal energy E_i. Equation (2.27) represents the steady state analytical solution to equation (2.26) incorporating a mono-energetic injection function.

$$N(E) \cong \frac{(q_0/2)(\beta_0/\beta)^{1/4}(\varepsilon/\varepsilon_0)^{1/2}}{(\alpha/3)^{1/2}a^{1/4}(E)a^{1/4}(E_i)\beta_0^{3/2}\varepsilon_0}\left[\frac{\varepsilon+\beta\varepsilon}{\varepsilon_0+\beta_0\varepsilon_0}\right]^{-(b+1)/2b} \times \exp\left[\left(\frac{-1}{2b}\right)\left(\beta^{-1}-\beta_0^{-1}\right)\right] \tag{2.27}$$

where,

$N(E)$ = particles per unit energy;

q_0 = rate of particle injection;

$\beta = v/c$;

E_i = energy of injected particles;

$a \approx (\delta+\alpha)\beta + (\alpha/3)\beta^{-1}$, with δ set to 1 s^{-1};

ε = energy + proton rest mass energy;

α is the acceleration efficiency;

$b = [(3/\alpha)(\delta+\alpha)]^{½}$.

Stochastic Acceleration: Neutral Current Sheet Injection

Equation (2.28) is an alternative steady-state numerical solution to equation (2.26) and incorporates a more realistic injection function which represents an initial

acceleration phase by DC electric fields within a neutral current sheet. The rapid dissipation of the magnetic field within current sheets releases stored magnetic energy. A major fraction of this released energy generates MHD turbulence and particles are then further accelerated to relativistic energies via resonating Alfvén wave–particle interactions. Equation (2.28) is based on an updated version of equation (51) in Gallegos-Cruz & Perez-Peraza (1995) (J. Perez-Peraza 2006, private communications). Further numerical quadrature was used to evaluate this integral, which is written as

$$N(E) \cong \frac{9.44\times10^{-7}}{(a\alpha/3)^{1/2}} \times \frac{\varepsilon^{1/2}\exp(-J_E)}{\beta^{1/4}} \times \int_{E_i}^{E} \frac{\exp\left[J_{E'} - 1.12(E'/E_c)^{3/4}\right]}{E'^{1/4}\,\varepsilon'^{3/2}\,D^{1/4}(E')}dE' \quad (2.28)$$

where

$\beta = (\varepsilon^2 - m^2c^4)^{1/2}/\varepsilon$;

$D = (a/3)\,\beta^3\varepsilon^2$;

E_i is the injection threshold value;

$E_c = 1.7926\text{x}10^3(\text{B}^3L/n) = 4.5$ MeV.

Here *N(E)* is particles per unit energy; *a* and *J* are analytical functions of energy as described by Gallegos-Cruz & Perez-Peraza (1995) and Perez-Peraza et al. (2006); ε is the energy + proton rest mass energy; B is the background magnetic field strength in the neutral current sheet (5 x 10^{-4} T); *n* is the local particle number density (10^{13} cm^{-3}); and *L* is the length of the neutral current sheet (10^7 cm).

2.3.3 *Non-Linear Least Squares Analysis*

The generalized non-linear least squares (GNLS) package used in this study is a FORTRAN program developed by Powell and MacDonald (1972). This program is designed to solve the GNLS problem where the model may be non-linear in its parameters and independent variables, and both are subject to errors. Furthermore, the program calculates all derivatives used in the analysis by numerical approximation, thereby avoiding the need for user-supplied input derivatives. The GNLS program converges rapidly to a solution yielding estimates of the parameters and providing good approximations to their variances.

To formalize the method, let the non-linear model represent a function $y=f(x, \alpha)$, where the components of α represent the parameters α_k, k = 1, 2,....., *NP* (Powell and MacDonald (1972)). The least squares condition requires that the sum of squares be minimized as follows:

$$WSS = \sum_{i=1}^{N} \left(w_{y_i} R_{y_i}^2 + w_{x_i} R_{x_i}^2 \right) \tag{2.29}$$

where;

$R_{y_i} = Y_i - y_i$ and $R_{x_i} = X_i - x_i$ are the least square residuals,

$w_{y_i} = 1/\sigma_{y_i}^2$ and $w_{x_i} = 1/\sigma_{x_i}^2$ are the weights w in terms of the variances σ of the observations.

N is the number of observations.

The program uses the Deming method to refine the user-supplied starting parameter guesses before the 'general method' is employed to find the final least squares approximations. The Deming method uses weights derived from uncertainty measures for each variable at each measured point. However, the Deming iterative solution is only an approximation and, on convergence, does not necessarily lead to a true least-squares solution. In contrast, the 'general method' iteration converges to a solution with a sum of squares always less than that found by the Deming method (MacDonald 1974).

For this study, the diffusive-shock acceleration equation (2.23) and stochastic acceleration equations (2.27) and (2.28) were incorporated into the GNLS program as functions in the log domain. The variable parameters for equation (2.23) are the shock compression ratio r and the e-folding energy E_0 (MeV). The variable parameters for equations (2.27) and (2.28) are the acceleration efficiency α and a normalization factor. The neutron monitor input into the GNLS fitting routine is chosen at selected energies with data points weighted by errors in the flux data, spaced evenly on a logarithmic scale.

2.4 SUMMARY

The historical development of GLE modelling has been briefly reviewed. This sets into context the form of the modelling used to investigate the 14 July 2000, 15 April 2001 and 20 January 2005 GLEs. Geomagnetic field disturbances are accounted for by the use of the Tsyganenko (1989) magnetospheric model. This model was upgraded to include the Dst index (Boberg *et al.,* 1995), allowing for a more accurate determination of viewing directions for appropriate levels of geomagnetic disturbance. To better resolve the responses of neutron monitors and produce a more accurate model of the arrival of relativistic particles at the Earth, asymptotic viewing cones were calculated using nine different arrival directions (vertical; and 90°, 180°, 270° and 360° azimuth at 16° and 32° zenith). The modelling procedure employed a least-squares method to efficiently analyse parameter space for optimum solutions. An exponential function was used to model the particle pitch angle distribution and a modification of this function was used to model bi-directional flow.

This chapter has also examined the theoretical framework behind the shock and stochastic mechanisms which can accelerate protons to relativistic energies (section 2.3). An analytical description of the widely used Ellison & Ramaty (1985) diffusive shock acceleration equation is given. In addition, analytical and numerical descriptions of stochastic acceleration via mono-energetic continuous injection and neutral current sheet injection are presented. To determine the acceleration processes responsible for the 14 July 2000, 15 April 2001 and 20 January 2005 GLEs, these analytical and numerical spectral forms were fitted to neutron monitor measurements of relativistic proton fluxes covering the energy spectrum up to 10 GeV, as described in the following chapters.

THE 14 JULY 2000 GLE

3.1 INTRODUCTION

The 14 July 2000 X5.8/3B solar flare and associated full halo CME (Figure 3.1) represent the largest of a series of solar transient phenomena which occurred during a period of intense solar activity extending from 10 to 15 July 2000. This period, described as the 'Bastille Day Epoch' by Dryer *et al.* (2001), produced three X-class flares (including the Bastille Day flare) and two halo CMEs that were observed with the *LASCO* coronagraphs (C2/C3) on board the *SOHO* spacecraft. The CMEs, associated shocks and magnetic cloud structures caused major disturbances to the IMF and the geomagnetic field (Dryer *et al.,* 2001). The primary source of this activity was NOAA active region 9077, located near the solar meridian N22°, W07° at the time of the Bastille Day flare.

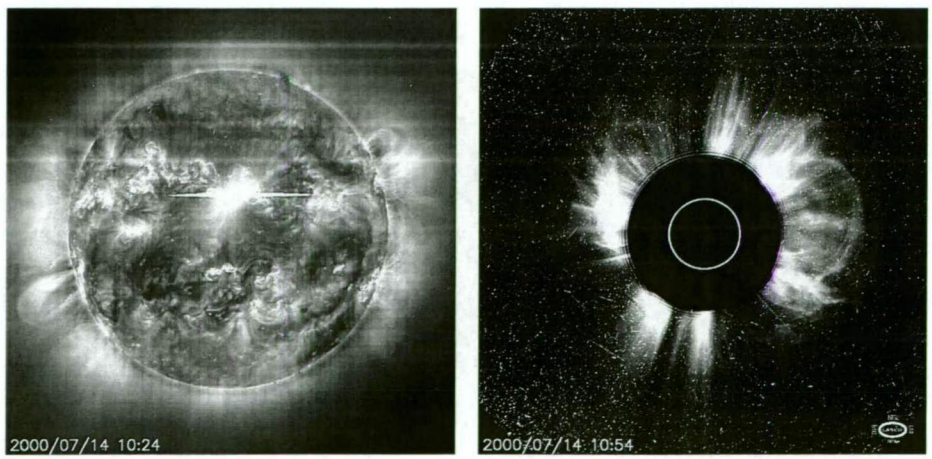

FIGURE 3.1: The 14 July 2000 solar flare as recorded by *EIT* on board *SOHO* at 171 Å (*left*). Source: see Figure 1.1. The 14 July 2000 CME as recorded by the *LASCO/C2* coronagraph on board *SOHO* (*right*). Source: http://soho.nascom.nasa.gov/hotshots/2000_07_14/1054_c2.jpg/

3.2 OBSERVATIONS

Soft X-rays observed by the *GOES 8* geostationary satellite commenced at 10:03 UT, and reached a peak at 10:24 UT (Figure 3.2). Klein *et al.* (2001) reported prominent bright continuum radio emission accompanied by a group of intense Type III bursts from microwave to hectometric wavelengths, with a sudden onset near 10:22 UT and a bright phase between 10:30 and 10:40 UT. Reiner *et al.* (2001) reported that the flare produced very intense, long-duration Type III radio emissions associated with electron acceleration deep in the solar corona. During its propagation through the solar corona and interplanetary medium, the associated CME generated decametric to kilometric Type II radio emissions (Reiner *et al.*, 2001). Share *et al.* (2001) reported that hard X-ray and γ-ray line emissions were observed by the *HXS* and *GRS* detectors on board the *Yohkoh* spacecraft at 10:20 UT, approximately four minutes before the peak in soft X-ray emission (10:24 UT). Both emissions peaked at 10:27 UT with γ-ray emission lasting until approximately 10:40 UT. The *HEPAD* detectors on board *GOES 8* recorded sudden increases in relativistic protons (370-850 MeV) between 10:30 and 10:35 UT (Figure 3.2).

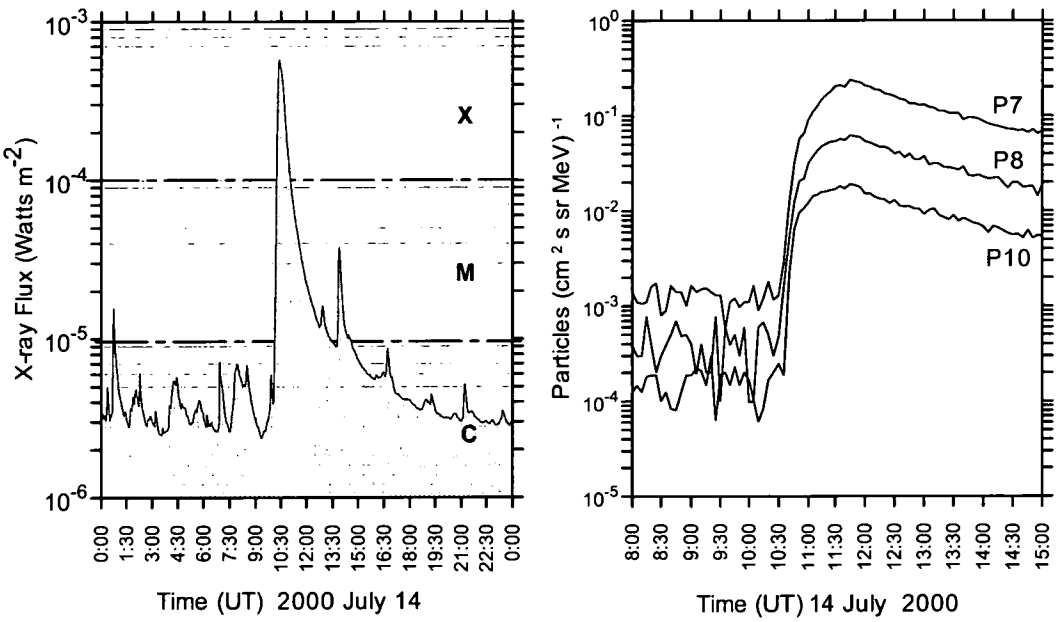

FIGURE 3.2: *GOES 8* observations of soft X-ray emissions at 1-8 Å (low energy channel) (*left*). Five minute *GOES 8* observations of relativistic proton fluxes (*right*). P8 to P10 represent the HEPAD detector differential energy channels (particles (cm^2 s sr $MeV)^{-1}$) with the following characteristics of nominal energy range (MeV): P8 = 370-480; P9 = 480-640; P10 = 640-850.

The GLE onset occurred between 10:30 and 10:35 UT at several stations, with Thule recording an onset at ~10:32 UT in 1-minute data.

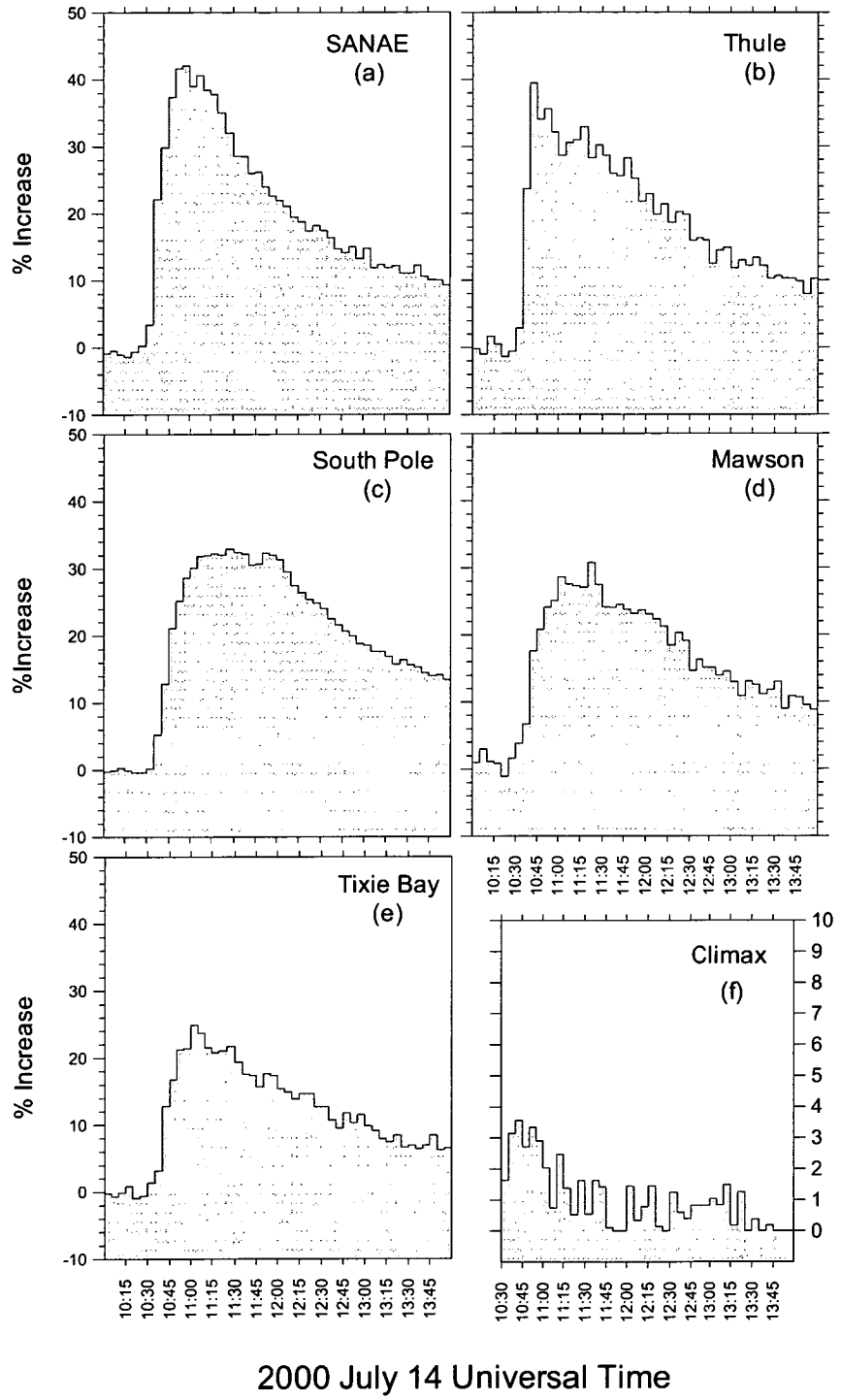

FIGURE 3.3: GLE intensity/time profiles (corrected to sea-level pressure) for 14 July 2000 as recorded by (*a*) SANAE, (*b*) Thule, (*c*) South Pole, (*d*) Mawson, (*e*) Tixie Bay and (*f*) Climax neutron monitors. The Climax intensity above background is shown on a different scale.

The largest neutron monitor responses were observed at South Pole and SANAE, with respective maxima in 5-minute data of 58.3% and 54.5% above the pre-increase levels. The event was seen at Climax, indicating the presence of particles with rigidity of at least 3.0 GV. The Lomnický Ŝtít neutron monitor, with a geomagnetic cut-off of 4.0 GV, recorded an increase of marginal significance that may or may not be related to the GLE. Corrections of observed increases to a standard sea-level atmospheric depth of 1033 g cm^{-2} were made using the two-attenuation length method of McCracken (1962*a*). An attenuation length of 110 g cm^{-2} was derived from a comparison of data from Mt Wellington, Hobart and Kingston neutron monitors. Figure 3.3 shows the details of the pressure-corrected sea-level intensity-time profiles for selected neutron monitors. SANAE was found to have the largest response (42.1%, Figure 3.3*a*) and was used as the normalisation station for this analysis.

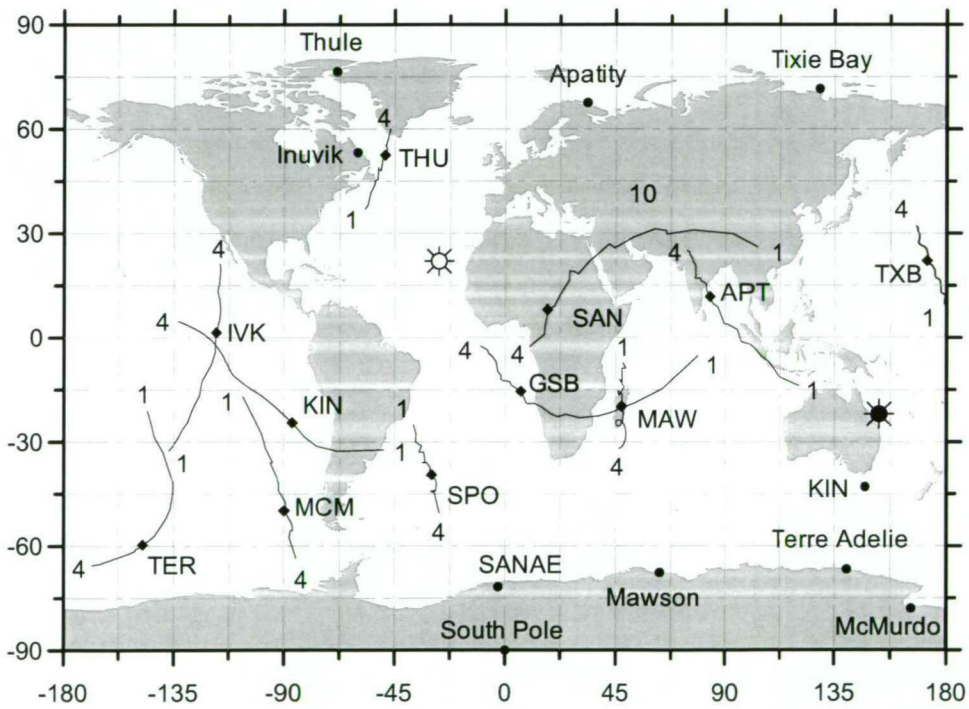

FIGURE 3.4: Viewing directions of neutron monitors in geographic coordinates at 10:40 UT (10 minutes after GLE onset) on 14 July 2000. Geomagnetic conditions were slightly disturbed (Kp = 4; Dst = -18). Lines for each station represent the vertical viewing direction at different rigidities. '4' represents the vertical viewing direction at maximum rigidity (~4 GV), while '1' represents the vertical viewing direction at the atmospheric cutoff (~1 GV). The solid circles show the median rigidity of response to the GLE for each station. Star and filled star symbols designate the position of the sunward and anti-sunward field direction respectively. Station abbreviations are: APT = Apatity, Russia; GSB = Goose Bay, Canada; IVK = Inuvik, Canada; KIN = Kingston, Australia; MAW = Mawson, Antarctica; MCM = McMurdo, Antarctica; SAN = SANAE, Antarctica; SPO = South Pole, Antarctica; TER = Terre Adélie, Antarctica; THU = Thule, Greenland; TXB = Tixie Bay, Russia.

Figure 3.4 shows the viewing directions (in geographic coordinates) of selected neutron monitors at 10:40 UT. The Thule neutron monitor, with a viewing direction near the measured field direction (*ACE*) recorded a rise to maximum intensity (39%) in approximately 10 minutes (Figure 3.3*b*) indicating that relativistic protons had very good access to Sun-Earth connecting field lines. This is in contrast to other events where the rise to maximum intensity can take many hours (e.g., the GLE of 19 October 1989). The rapid rise is surprising considering the source of the 14 July 2000 solar eruption, near the solar meridian, which is at a considerable distance from the nominal garden hose foot-point (i.e., W60°). Significant increases in neutron monitor responses at 10:40 UT were also observed at stations viewing in the anti-sunward field direction (e.g., Tixie Bay, 12.8%; Figure 3.3*e*), as well as stations viewing perpendicular to the measured sunward field direction (e.g., Apatity, 30.6% and Inuvik, 15.3% not shown in Figure 3.3).

3.3 MODELLING THE NEUTRON MONITOR RESPONSE

The geomagnetic field model as described in section 2.2.4 with IGRF 2005 parameters was employed to determine the asymptotic viewing directions of neutron monitors. Observations from 30 neutron monitors were modelled for every five-minute interval between 10:35 and 10:55 UT during the rise and peak phases of the event. During the decay phase, observations were modelled every ten-minutes from 11:00 to 14:00 UT. Each indicated time represents the start of a five-minute integration interval. Parameter determinations are less accurate later in the event, when the increase above background is small. Fits were discontinued at 14:00 UT by which time the increase above the background at the normalisation station (SANAE) was ~10 %.

Tables 3.1 and 3.2 show the calculated percentage increase for time intervals representing the rise (10:35 to 10:50 UT), peak (10:55 UT, 11:00 UT) and decline (11:10, 11:20, 11:40 and 11:50 UT) phases of the event along with the actual increases corrected to standard sea-level atmospheric depth. Good fits to observations were achieved during all phases of the 14 July 2000 GLE. However, South Pole and Mawson responses were not as well fitted during the high intensity phase of the event.

TABLE 3.1

COMPARISON OF OBSERVED AND CALCULATED INCREASES FOR THE 14 JULY 2000 GLE FOR THE MODIFIED POWER LAW FIT

Station	Lat.	Lon.	P_c [b]	Alt.	10:35 UT		10:40 UT		10:45 UT		10:50 UT	
	(deg.)	(deg.)	(GV)	(m)	Observed [c]	Calculated [d]	Observed [c]	Calculated [d]	Observed [c]	Calculated [d]	Observed [c]	Calculated [d]
Apatity	67.55	33.33	0.61	177	20.0	18.7	30.6	22.9	32.2	28.6	28.2	29.1
Aragats	40.50	44.17	7.60	3200	0.0	0.8	0.0	0.0	0.0	0.0	0.0	0.1
Climax	39.37	253.82	3.03	3400	3.1	4.4	3.5	5	2.7	4.1	3.3	3.9
Goose Bay	53.27	299.60	0.52	46	8.6	9.0	18.5	18.6	23.2	23.6	24.1	26.9
Haleakala	20.27	203.73	13.3	3033	0.0	0.1	0.0	0.0	0.0	0.0	0.0	0.0
Hermanus	-34.42	19.22	4.90	26	11.1	4.4	15.3	12.1	15.6	14.1	16.1	14.0
Hobart	-42.90	147.33	1.88	18	1.6	1.8	0.0	0.2	1.1	0.2	1.8	0.3
Inuvik	68.35	226.28	0.18	21	7.5	5.1	15.6	13.3	18.9	18.3	20.8	21.5
Jungfraujoch	46.55	7.98	4.48	3475	0.8	1.2	0.5	0.1	0.2	0.2	0.4	0.3
Kerguelen Island	-49.35	70.25	1.19	33	6.4	10	14.9	20.9	22.7	24.3	26.2	25.1
Kiel	54.33	10.13	2.29	54	3.3	4.6	7.4	8.4	8.2	8.0	7.0	7.1
Kingston	-42.99	147.29	1.88	65	8.6	4.3	16.2	12.0	15.4	14.4	14.2	13.9
LARC	-62.20	301.04	2.21	40	1.2	1.8	1.3	0.8	1.3	0.8	1.2	0.9
Lomnický Štít	49.20	20.22	4.00	2634	4.1	7.7	1.7	4.8	4.0	3.9	3.2	3.8
Magadan	60.12	151.02	2.10	220	6.7	8.0	17.6	17.3	20.8	24.3	24.1	27.4
Mawson	-67.60	62.88	0.22	30	7.3	4.6	11.2	12.0	11.5	14.6	12	14.6
McMurdo	-77.85	166.72	0.01	48	2.0	5.0	11.4	11.8	20.1	18.5	26.3	22.0
Moscow	55.47	37.32	2.46	200	4.1	4.3	8.4	9.3	9.1	7.5	8.7	7.1
Mt. Wellington	-42.92	147.23	1.89	725	10.0	4.4	14.2	11.8	16.2	14.3	15.3	13.6
Newark	39.68	284.25	1.97	50	6.3	6.3	8.9	10.9	7.7	9.6	8.8	8.1
Oulu	65.05	25.47	0.81	15	17.3	14.7	24.8	19.7	25.0	25.3	24.8	26.5
Potchefstroom	-26.68	27.10	7.30	1351	1.1	0.6	1.2	0.0	1.6	0.0	0.2	0.0
Rome	41.86	12.47	6.32	0	0.0	0.5	0.0	0.0	0.0	0.0	0.0	0.0
SANAE [a]	-71.67	357.15	1.06	856	22.2	22.2	30.0	30.0	37.5	37.3	41.8	41.8
South Pole	-90.00	0.00	0.10	2820	5.2	4.9	12.8	13.0	21.1	18.8	25.2	22.3
Terre Adelie	-66.67	140.02	0.01	45	3.7	5.5	9.7	12.1	16.2	19.1	18.9	23.0
Thule	76.50	291.30	0.00	260	23.7	23.3	39.6	37.1	34.2	33.3	35.8	36.5
Tixie Bay	71.58	128.92	0.53	0	3.2	6.3	12.8	16.0	16.7	20.4	21.2	22.8
Tsumeb	-19.20	17.58	9.29	1240	0.3	0.3	0.0	0.0	0.0	0.0	0.9	0.0
Yakutsk	62.03	129.73	1.70	105	3.7	4.7	10.2	12.1	14.6	17.1	15.7	19.3

[a] Normalisation station

[b] Nominal vertical geomagnetic cutoff rigidities represent the minimum rigidities below which particles do not have access to a particular site on the Earth's surface. The cut-off at the geomagnetic equator is ~ 17 GV, decreasing to zero at the geomagnetic poles.

[c] Actual % increases corrected to standard sea level atmospheric depth.

[d] Calculated % increases

TABLE 3.2

COMPARISON OF OBSERVED AND CALCULATED INCREASES FOR THE 14 JULY 2000 GLE FOR THE MODIFIED POWER LAW FIT

Station	10:55 UT.		11:00 UT		11:10 UT		11:20 UT		11:40 UT		11:50 UT	
	Observed [b]	Calculated [c]	Observed [b]	Calculated [c]	Observed [b]	Calculated [c]	Observed [b]	Calculated [c]	Observed [b]	Calculated [c]	Observed [b]	Calculated [c]
Apatity	26.2	27.4	28.4	28.3	26.4	27.4	24.9	26.7	20.9	21.8	21.5	20.6
Aragats	0.0	0.0	0.0	0.2	0.0	0.1	0.0	0.1	0.0	0.0	0.0	0.0
Climax	2.9	3.3	2.0	2.8	2.5	2.1	0.5	1.6	1.4	1.0	0.0	0.6
Goose Bay	27.9	30.5	30.8	31.9	26.7	31.9	28.9	32.5	22.8	26.5	22.5	25.2
Haleakala	0.0	0.0	0.0	0.0	0.0	0.0	0.0	0.0	0.0	0.0	0.0	0.0
Hermanus	13.4	13.2	13.6	13.0	12.8	11.4	12.0	11.0	9.9	9.1	7.6	7.6
Hobart	0.6	0.4	0.0	0.4	0.0	0.2	0.6	0.2	0.9	0.1	0.0	0.1
Inuvik	22.2	22.6	25.8	24.0	27.3	23.6	27.1	23.2	24.2	19.4	21.8	18.1
Jungfraujoch	0.3	0.3	1.2	0.3	0.1	0.2	0.6	0.1	0.7	0.1	0.9	0.0
Kerguelen Island	26.9	24.1	28.0	24.8	26.7	24.9	26.2	24.4	22.7	20.0	20.6	19.5
Kiel	6.7	6.2	6.5	6.0	4.8	4.4	4.5	3.6	1.5	2.6	2.6	1.9
Kingston	14.5	14.1	14.7	13.9	12.7	13.1	11.4	12.8	10.1	10.4	8.2	7.8
LARC	1.0	0.8	1.3	0.9	1.0	0.6	0.8	0.5	0.4	0.2	0.5	0.2
Lomnický Štít	1.6	3.4	3.0	3.1	2.0	2.3	0.7	1.3	0.5	0.9	2.0	0.7
Magadan	25.1	30.5	28.6	32.3	27.3	31.7	30.7	31.9	24.5	25.6	23.1	24.3
Mawson	10.8	13.3	10.6	12.5	10.6	10.8	8.6	9.1	7.0	7.6	6.2	7.0
McMurdo	24.5	23.4	24.0	25.3	26.1	25.2	29.8	25.8	21.9	23.0	20.4	22.4
Moscow	8.6	6.0	7.8	6.2	6.7	5.4	5.7	4.5	3.7	3.1	3.9	2.7
Mt. Wellington	15.8	14.4	14.6	14.6	11.8	12.0	11.3	10.5	9.3	8.5	9.5	8.5
Newark	7.3	7.6	5.4	6.8	4.8	5.4	3.4	3.6	3.0	2.8	1.1	2.1
Oulu	27.9	25.9	28.8	27.5	27.3	26.6	25.1	26.5	20.4	21.7	20.9	20.8
Potchefstroom	0.6	0.0	2.5	0.1	0.0	0.0	0.0	0.0	0.8	0.0	0.0	0.0
Rome	0.0	0.1	0.0	0.1	0.0	0.0	0.0	0.0	0.0	0.0	0.0	0.0
SANAE [a]	42.2	42.2	39.1	39.0	38.6	38.4	35.2	35.1	26.1	26.0	24.1	24.1
South Pole	28.7	25.6	30.1	27.0	32.0	28.1	32.0	30.2	30.6	29.3	32.3	31.4
Terre Adelie	22.4	24.2	22.1	26.0	25.8	26.0	24.6	26.0	23.4	21.4	21.9	20.5
Thule	32.2	33.5	28.7	29.8	31.1	33.4	28.4	31.4	25.7	27.8	25.3	26.4
Tixie Bay	21.4	23.3	24.8	25.4	21.5	25.4	21.0	26.0	17.3	21.6	17.6	21.0
Tsumeb	0.4	0.0	0.0	0.0	0.2	0.0	0.1	0.0	0.0	0.0	0.0	0.0
Yakutsk	15.9	19.8	16.6	21.1	13.8	21.1	14.2	20.1	11.3	17.9	11.2	16.0

[a] Normalisation station

[b] Actual % increases corrected to standard sea level atmospheric depth.

[c] Calculated % increases

In particular, the model slightly overestimated the neutron monitor response at Mawson and underestimated the neutron monitor response at South Pole. Model fits to observations for time intervals not shown in Tables 3.1 and 3.2 are presented in Appendix A.

3.3.1 *Arrival Directions*

Figure 3.5 illustrates the GSE latitude and longitude of the axis of symmetry of the particle pitch angle distribution (arrival direction), together with the IMF direction. The average GSE longitude of the IMF direction (as measured by *ACE*) was 330°, which implies that (longitudinally) particles were flowing from the Sun close to a nominal Parker spiral. The apparent longitude of the arrival direction between 10:30 and 11:00 UT was centred slightly east of the Sun-Earth line, and is approximately 30° east of the measured field direction. Between 11:10 and 12:40 UT the model shows good agreement with the measured IMF longitude. However, from 12:40 to 15:00 UT, model longitudes move east of the measured field longitude by up to ~120°.

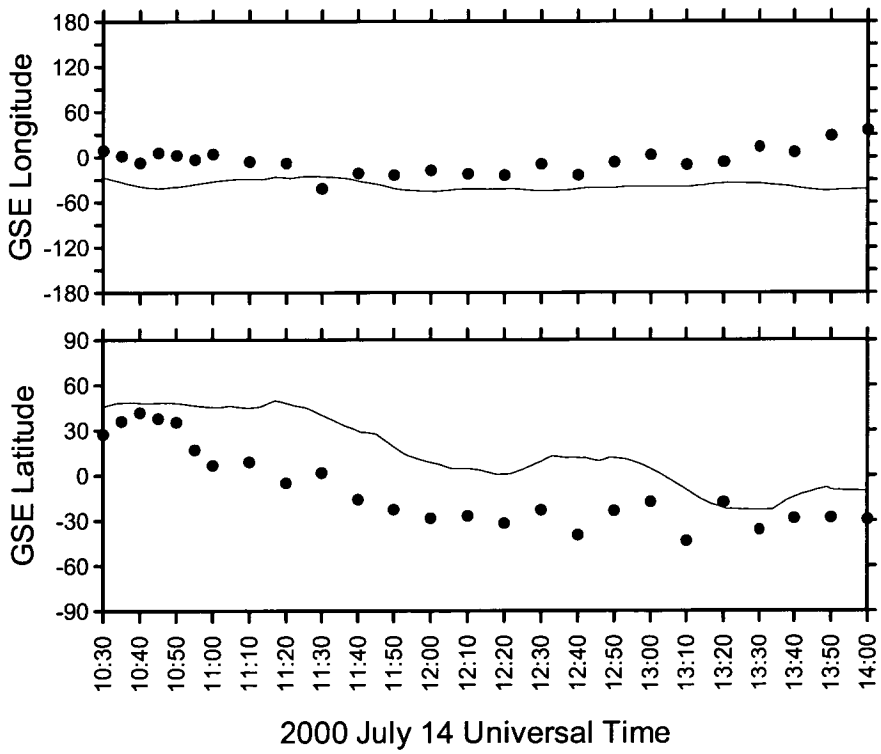

FIGURE 3.5: GSE longitude (*top*) and GSE latitude (*bottom*) of the apparent arrival directions (this study; solid circles) plotted with the negative magnetic field direction (1-hour centred moving averages; line) as measured by the *MAG* instrument onboard the *ACE* spacecraft.

From 10:30 to 10:55 UT the apparent latitude of the arrival direction shows good agreement with the measured field latitude. However, during the decline phase model latitudes are in poor agreement with the measured field latitude, although they do follow the overall southerly trend. As noted by Bieber *et al.* (2002) there is no reason why the magnetic field measured at a point should be the same as the average field sampled by the particle over its orbit. For example, a 2 GV proton has a Larmor radius of ~0.01 AU, which is of the order of the coherence length of interplanetary magnetic turbulence. Therefore, model flow vectors need not align exactly with the measured magnetic field vector.

3.3.2 *Pitch Angle Distributions*

The particle pitch angle α is defined as the angle between the particle velocity and the mean magnetic field. The pitch angle distribution used here is a simplification of the exponential form described by Beeck & Wibberenz (1986) and is defined by parameters A and B (see section 2.2.9). Parameter A has most effect on the width of the anisotropy while B has most effect on the relative flux at pitch angles >90°. The distribution can be considered as having an anisotropic component (representing particles which arrive directly from the Sun) and an isotropic component (where the effects of local scattering dominate the distribution).

The temporal development of the pitch angle distribution between 10:35 and 11:40 UT is illustrated in Figure 3.6 and the fitted parameters are listed in Table 3.3.

TABLE 3.3

PITCH ANGLE DISTRIBUTION PARAMETERS
14 JULY 2000

Time [a] (UT)	A [b]	B [c]
10:35.....	0.012	0.509
10:40.....	0.318	1.171
10:45.....	0.140	1.488
10:55.....	0.030	1.398
11:10.....	0.030	2.350
11:40.....	0.470	3.447

[a] Time refers to the start of a five-minute interval.
[b] Parameter A has most effect on the width of the anisotropy.
[c] Parameter B has most effect on the relative flux in the reverse direction.

Near GLE onset (10:35 UT) the particle arrival was strongly anisotropic. This suggests that, initially, relativistic protons injected into the interplanetary medium arrived directly from the Sun without being affected to significant degrees by local scattering. However, the anisotropy decreased rapidly over the next 20 minutes and remained relatively unchanged thereafter. This indicates that relativistic particles experienced significant scattering.

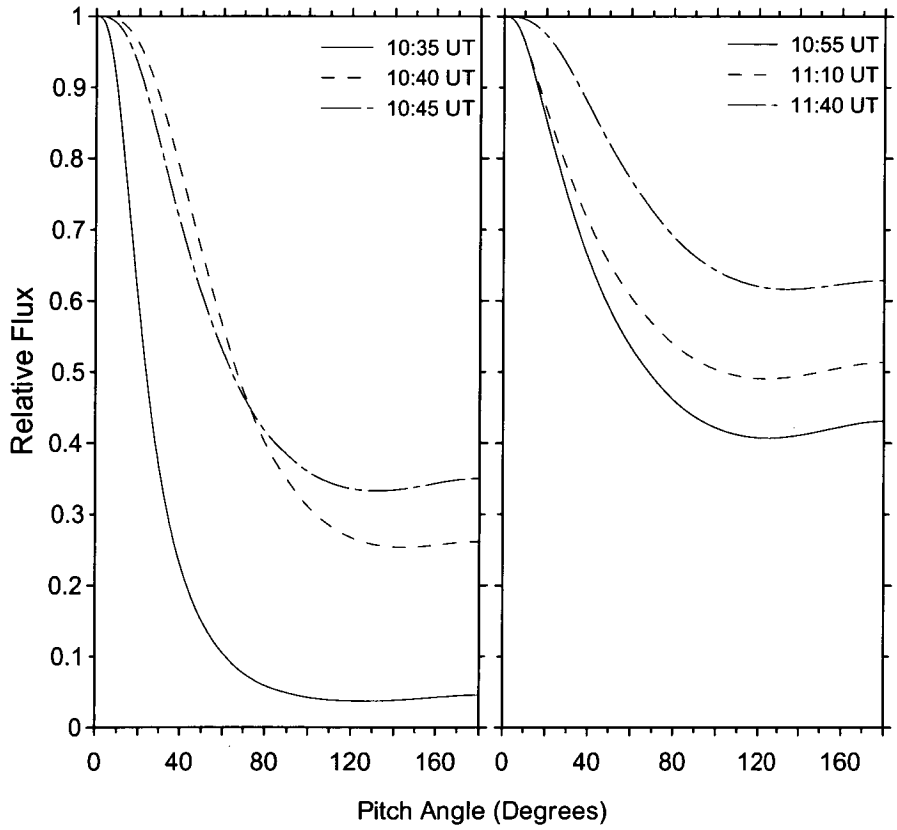

FIGURE 3.6: Derived pitch angle distributions for 10:35, 10:40, 10:45, 10:55, 11:10 and 11:40 UT, during the 14 July 2000 GLE.

3.3.3 *Spectrum*

An advantage of the GLE modelling technique used in this study is the ability to utilize various spectral forms such as pure and modified power laws, as well as theoretical shock acceleration spectra (Ellison & Ramaty, 1985), to achieve the best fit between observed and calculated responses (see section 2.2.10). In contrast, Bieber *et al.* (2002) determined spectral exponents from the ratio of count rates of the standard (NM64) neutron monitor at the South Pole and an unshielded (Polar Bare) neutron monitor at the same site. Their technique utilises the different response

functions of these neutron monitors. The yield function used by Bieber *et al.* (2002) differs from that used in this study (Debrunner, Flückiger & Lockwood 1982). Use of the Debrunner *et al.* function generally produces steeper power law spectra compared to the model of Bieber & Evenson (1991). Lockwood *et al.* (2002) combined the Debrunner *et al.* yield function with the Bieber & Evenson (1991) method to calculate spectral exponents, albeit with Mt. Washington and Durham stations, and also obtained steeper spectral exponents.

TABLE 3.4

MODEL PARAMETERS AND ASSOCIATED SPECTRAL FORMS

		Power Law			Modified Power Law				Modified Ellison & Ramaty			
Time [a]	Inc [b]	J_{II} [c]	γ [d]	wss [e]	J_{II}	γ	$\delta\gamma$ [f]	wss [g]	J_{II}	γ	$\delta\gamma$ [h]	wss [i]
10:30	3.39	2	-4.35	22	2	-4.30	2.35×10^{-3}	22	2	-3.97	0.12	22
10:35	22.12	49	-5.18	221	50	-5.21	5.61×10^{-6}	220	21	-2.97	5.40	218
10:40	29.87	55	-5.76	311	4	-0.01	4.15×10^{0}	274	9	-0.54	15.64	273
10:45	37.38	98	-6.33	173	40	-3.97	2.10×10^{0}	131	19	-0.98	17.76	132
10:50	41.66	120	-6.64	193	100	-5.76	1.01×10^{0}	157	80	-4.63	7.35	152
10:55	42.07	114	-6.86	200	132	-6.89	3.80×10^{-1}	146	86	-5.10	7.38	157
11:00	39.00	101	-6.98	200	142	-7.57	4.78×10^{-3}	138	79	-5.22	7.95	158
11:10	38.43	119	-7.31	290	189	-7.96	6.40×10^{-4}	222	109	-5.93	7.06	253
11:20	35.03	118	-7.54	261	186	-8.43	3.91×10^{-3}	186	116	-5.64	11.73	203
11:30	28.58	98	-7.76	187	179	-8.68	2.71×10^{-9}	117	105	-6.60	7.62	160
11:40	26.00	96	-7.67	233	191	-8.76	8.60×10^{-3}	164	104	-5.53	14.68	180
11:50	23.98	109	-7.91	161	241	-9.19	4.46×10^{-6}	100	129	-6.48	11.00	127
12:00	21.96	106	-8.00	165	239	-9.41	4.61×10^{-4}	107	139	-5.37	24.29	108
12:10	19.46	89	-7.95	158	204	-9.46	3.48×10^{-6}	96	108	-6.58	11.90	135
12:20	17.36	86	-8.14	116	211	-10.00	1.26×10^{-3}	63	116	-5.90	22.60	66
12:30	17.44	89	-8.27	145	212	-9.77	1.34×10^{-3}	95	86	-6.67	16.64	125
12:40	14.70	61	-7.82	139	136	-9.09	1.75×10^{-9}	95	68	-5.72	16.27	109
12:50	15.03	67	-7.97	99	103	-9.33	4.02×10^{-8}	74	80	-6.36	13.36	83
13:00	14.78	66	-7.83	101	147	-9.85	5.49×10^{-2}	75	79	-5.82	15.67	90
13:10	12.36	53	-7.95	90	117	-9.35	1.20×10^{-5}	63	62	-6.28	13.70	83
13:20	12.20	59	-8.03	81	111	-9.29	8.24×10^{-9}	62	54	-6.16	13.02	81
13:30	11.07	49	-7.81	65	89	-8.76	7.72×10^{-6}	56	50	-6.16	10.45	84
13:40	10.58	49	-8.05	76	90	-8.78	6.31×10^{-1}	71	54	-5.62	18.45	64
13:50	10.02	48	-7.97	54	50	-6.21	5.21×10^{0}	49	50	-7.57	2.13	53
14:00	10.02	44	-8.00	53	56	-7.20	2.80×10^{0}	51	47	-5.97	15.72	48

[a] Time (UT) refers to the start of a five-minute interval.
[b] Sea-level corrected percentage increases above the pre-event galactic cosmic ray background of the normalization station, SANAE.
[c] Flux (particles $(cm^2\ s\ sr\ GV)^{-1}$) at 1 GV summed over the forward steradian.
[d] Spectral slope (at 1 GV for modified power law and modified Ellison and Ramaty forms).
[e] Best-fit weighted sum of squares employing the power law spectral form.
[f] Modified power law exponent modifier ($\delta\gamma$).
[g] Best fit weighted sum of squares employing the modified power law spectral form.
[h] Ellison & Ramaty spectral modifier ($\delta\gamma$).
[i] Best fit weighted sum of squares employing the modified Ellison & Ramaty (1985) spectral form.

Modelling results showed that the modified power law spectral form, in general, produced the best fit (Table 3.4). The derived particle spectra are illustrated in Figure 3.7. The spectral slope varied considerably during the rise phase of the event (10:35-10:55 UT). At 10:35 UT the spectrum was represented by a power law but by 10:40 and 10:45 UT the change of slope parameter ($\delta\gamma$) was significant. By 11:00 UT the spectrum again exhibited small values of $\delta\gamma$.

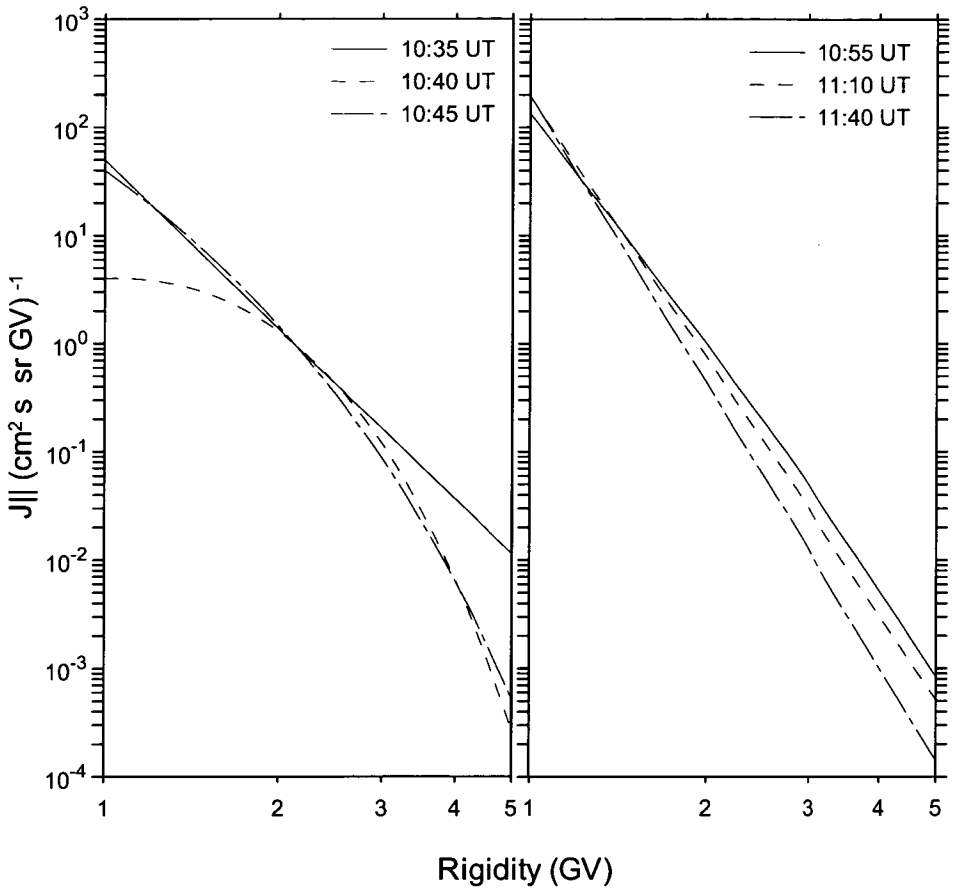

FIGURE 3.7: Derived modified power law rigidity spectra for 10:35, 10:40, 10:45, 10:55, 11:10 and 11:40 UT, during the 14 July 2000 GLE.

3.4 CONFIDENCE LIMITS ON PARAMETERS

Rigorous error analyses of the derived parameters are difficult due to the complexity of the model and the strong interdependence between the parameters of the fit. An attempt to estimate the uncertainty of the derived parameters can be made by considering the relative changes in the sum of squares between the observed and calculated increases for each solution, giving a measure of the significance of the change in the parameters.

Uncertainties for the geographic latitude and longitude of the apparent arrival directions are influenced by the adequacy of the asymptotic direction calculations to describe the actual propagation of the particles through the magnetosphere (Lovell, Duldig & Humble 1998). The degree of anisotropy of the particle distribution is also an important factor. Broader pitch angle distributions result in less confidence in the axis of symmetry. The uncertainty for the particle arrival directions at 10:35 UT is estimated to be ±8° in latitude and ±16° in longitude. At 13:25 UT these

uncertainties are estimated to be ±20° in both latitude and longitude. Uncertainties for parameters at most other times will lie between these values.

The uncertainty of the spectral slope (γ) at 10:35 UT is expected to exceed that at most other times due to the dominance of the particle anisotropy at this time. The very small spatial extent of the particle arrival distribution means that only a few stations with similar asymptotic viewing directions and rigidity apertures observed this part of the event. Consequently, spectral information is restricted to a narrow rigidity range leading to an uncertainty in the slope. The spectral slope (γ) at 10:35 UT is -5.2 ±1.0. At 13:25 UT γ is -8.0 ±0.1. The uncertainty in the change of slope ($\delta\gamma$) at 10:35 UT is small, while at 13:25 UT the uncertainty in $\delta\gamma$ is estimated at ± 0.2. The uncertainty in the calculated flux at 1 GV is less than 10%.

3.5 MODELLING PARTICLE ACCELERATION

Modified power law empirical spectra deduced from the neutron monitors were used to generate the input to the GNLS program at selected energies (spaced evenly on a logarithmic scale) with data points weighted by errors in the flux data. This spectral form was used to avoid a circular argument when fitting the full Ellison & Ramaty (1985) spectral form (equations 2.23 & 2.24) to synthetic neutron monitor data. Best-fit variable model parameters derived from the program were re-input into equations (2.23), (2.27) and (2.28) to generate theoretical shock and stochastic acceleration spectra up to 5 GeV.

3.5.1 *Results*

Tables 3.5, 3.6 and 3.7 present the best fit theoretical spectra for the data generated from the empirical fits to the neutron monitor observations at the rising phase (10:45 UT), peak phase (10:55 and 11:00 UT) and declining phase (11:10 and 11:40 UT). A Kolmogorov-Smirnov test at 95% confidence shows that all post-fit residuals were random, giving confidence in the weighted sum of squares result. Table 3.5 lists the results and standard errors for the variable model parameters (compression ratio and *e*-folding energy E_0) from the shock acceleration non-linear least squares fitting routine.

TABLE 3.5

VARIABLE MODEL PARAMETERS: SHOCK ACCELERATION

14 JULY 2000

Time [a] (UT)	r [b]	E_0 [c] (MeV)	WSS [d]
10:45.....	1.93 ±0.02	1869 ±06	88
10:55.....	1.78 ±0.01	1723 ±55	154
11:00.....	1.76 ±0.02	1527 ±72	209
11:10.....	1.72 ±0.02	1442 ±68	234
11:40.....	1.75 ±0.03	1211 ±46	1047

[a] Time refers to the start of a five-minute interval
[b] Shock compression ratio
[c] *e*-folding energy
[d] Weighted sum of squares

TABLE 3.6

VARIABLE MODEL PARAMETERS: STOCHASTIC ACCELERATION MONOENERGETIC INJECTION

14 JULY 2000

Time [a] (UT)	N [b]	α [c] (s^{-1})	WSS [d]
10:45.....	891 ±225	0.0511 ±0.0020	541
10:55.....	3213 ±128	0.0410 ±0.0004	10
11:00.....	4104 ±349	0.0375 ±0.0007	34
11:10.....	7068 ±646	0.0340 ±0.0007	38
11:40.....	9878 ±1162	0.0291 ±0.0005	115

[a] Time refers to the start of a five-minute interval
[b] Normalization factor
[c] Acceleration efficiency
[d] Weighted sum of squares

TABLE 3.7

VARIABLE MODEL PARAMETERS: STOCHASTIC ACCELERATION NEUTRAL CURRENT SHEET INJECTION

14 JULY 2000

Time [a] (UT)	N [b]	α [c] (s^{-1})	WSS [d]
10:45.....	0.30 ±0.09	0.0301 ±0.0012	671
10:55.....	1.45 ±0.03	0.0234 ±0.0001	2
11:00.....	2.10 ±0.01	0.0215 ±0.0002	11
11:10.....	4.30 ±0.30	0.0195 ±0.0002	12
11:40.....	9.08 ±0.80	0.0164 ±0.0002	35

[a] Time refers to the start of a five-minute interval
[b] Normalization factor
[c] Acceleration efficiency
[d] Weighted sum of squares

The proton spectrum at 10:45 UT is best fitted with this spectral form. The shock compression ratio for this interval is 1.93 ± 0.03 with an *e*-folding energy of 1.87 GeV ± 0.06. This value of the *e*-folding energy corresponds to a rigidity of ~2.7 GV, which is consistent with the maximum proton rigidity of ~3 GV observed for this event.

Tables 3.6 and 3.7 list the results and standard errors for the variable model parameters (normalization factor N and acceleration efficiency α) from the stochastic acceleration mono-energetic continuous injection and NCS injection models. The proton spectra at the peak (10:55 and 11:00 UT) and in the declining phase (11:40 UT) are best fitted with these spectral forms.

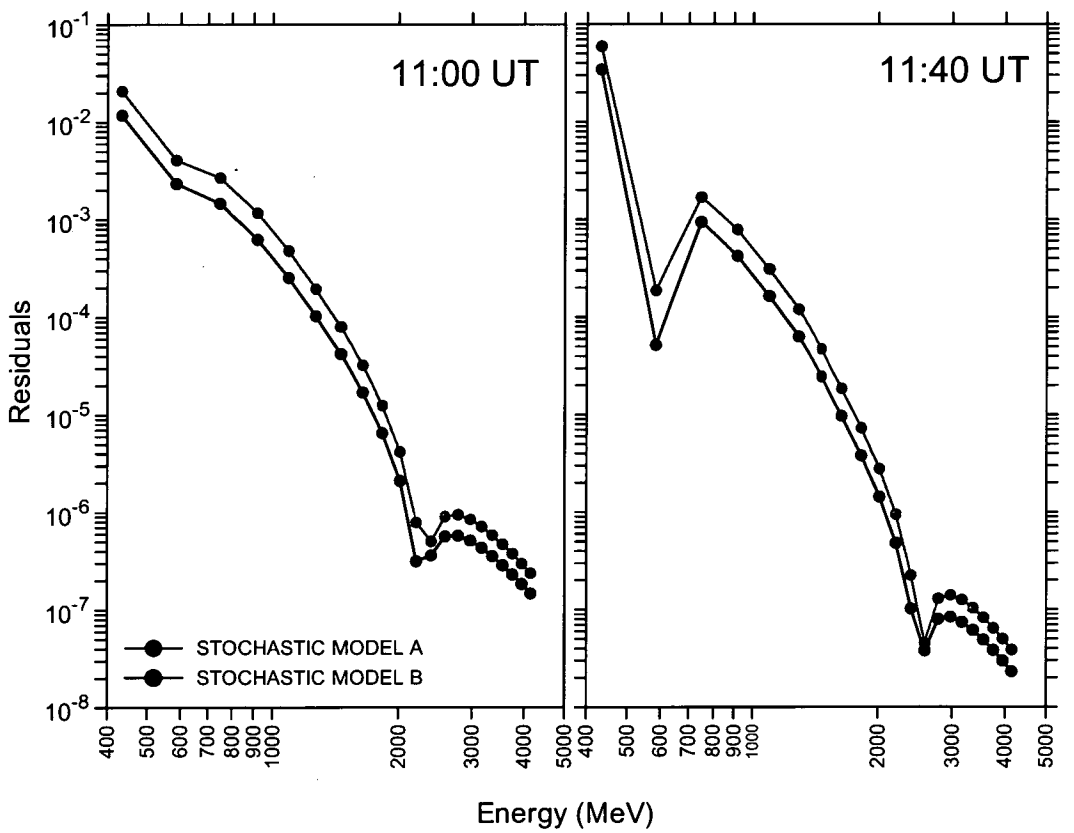

FIGURE 3.8: Least squares Y-residual plotted against kinetic energy for the 14 July 2000 GLE. These plots illustrate more clearly the better fit of stochastic acceleration with NCS injection (*black line*) as opposed to stochastic acceleration with mono-energetic injection (*light grey line*): 11:00 UT peak phase (*left panel*) and 11:40 UT decline phase (*right panel*).

Figure 3.8 shows the residuals calculated from the non-linear least squares fitting routine for two intervals (11:00 and 11:40 UT) plotted against kinetic energy. This figure illustrates more clearly the improved fit of the stochastic acceleration

model via neutral current sheet injection when compared to the stochastic acceleration model via mono-energetic continuous injection. For the time intervals modelled, α ranged from 0.02 to 0.03 s^{-1}, which is consistent with values reported from previous studies (Murphy & Ramaty 1984; Miller, Guessoum & Ramaty 1990; Miller 1991). Because the stochastic acceleration model with NCS injection represents a more realistic injection process; this model is used hereafter.

Figure 3.9 illustrates the results of the shock and stochastic acceleration model spectral fits at the rise (10:45 UT) and peak (10:55 UT) phases of the event.

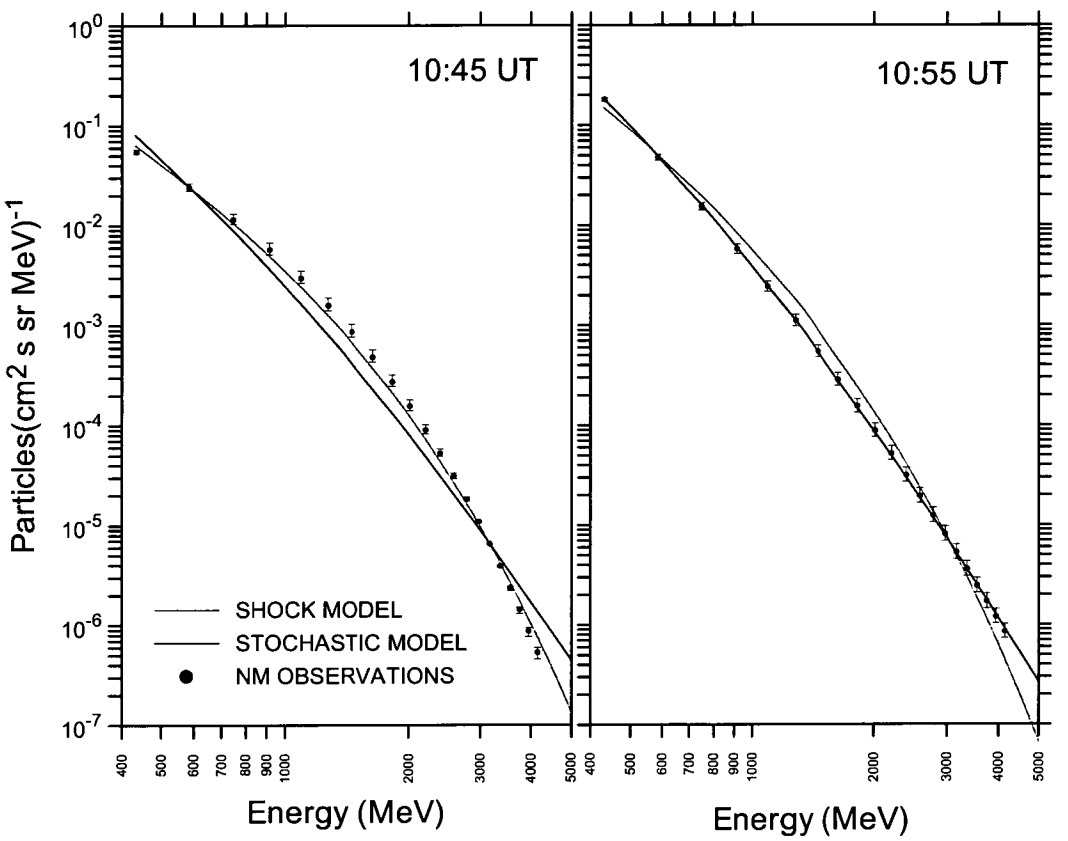

FIGURE 3.9: Energy spectral fits to flux values generated from ground-based neutron monitor observations (ranging from ~400 MeV to 5 GeV) for intervals 10:45 UT (*rising phase*) and 10:55 UT (*peak phase*). Fluxes (*black dots*) are shown with corresponding 1-sigma error bars. Fitted curves are of the Ellison & Ramaty (1985) shock acceleration (*light grey line*) and the Gallegos-Cruz & Perez-Peraza (1995) stochastic acceleration Model B spectral forms (*black line*).

Figure 3.10 shows the residuals calculated from the non-linear least squares fitting routine for intervals 10:45 UT and 10:55 UT plotted against kinetic energy. Figure 3.10 *(left panel)* illustrates the better fit of the Ellison & Ramaty (1985) shock acceleration model compared to the stochastic acceleration model (via NCS

injection) at 10:45 UT (*rising phase*). In contrast, Figure 3.10 *(right panel)* illustrates the converse at 10:55 UT (*peak*).

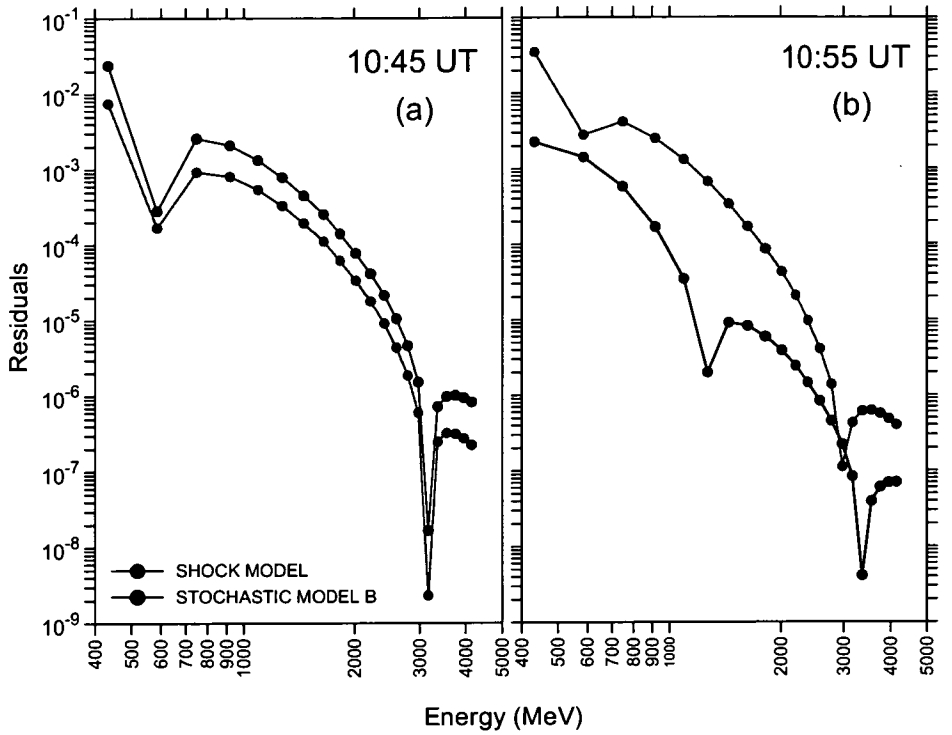

FIGURE 3.10: Least squares Y-residual (GNLS fitting routine) plotted against kinetic energy for the 14 July 2000 GLE. Stochastic acceleration model with NCS injection (*black line*) and Ellison & Ramaty (1985) shock acceleration model (*light grey line*): (*a*) 10:45 UT and (*b*) 10:55 UT.

3.5. SUMMARY

The arrival of relativistic protons at 1 AU for the 14 July 2000 GLE has been modelled using a global analysis technique which deduces the spectrum, arrival direction and anisotropy of high-energy protons. The largest neutron monitor responses were observed at South Pole and SANAE with respective maxima in 5-minute data of 58.3% and 54.5% above the pre-increase levels. Significant increases in neutron monitor responses were also observed at stations viewing in the anti-sunward field direction (e.g., Tixie Bay), including stations viewing perpendicular from the measured sunward field direction (e.g., Inuvik). Particles of at least 3 GV were present because the event was observed by the Climax neutron monitor. The maximum intensity was reached in approximately 20 minutes, indicating that relativistic protons had reasonable access to Sun-Earth connecting field lines. The decay phase lasted several hours. The event was characterised by a strongly anisotropic onset followed by a rapid decrease in anisotropy. This indicates

that initially particles injected into the interplanetary medium propagated to Earth essentially scatter free. However, there is evidence to suggest that particles arriving at Earth shortly after were affected by significant degrees of scattering.

Theoretical shock and stochastic acceleration spectral forms were employed to investigate the acceleration process. The spectrum during the rise phase (10:45 UT) was best fitted with a shock acceleration spectral form; implying relativistic proton acceleration by a coronal shock. In contrast the spectra at the peak (10:55, 11:00 UT) and declining phases (11:10, 11:20 and 11:40 UT) of the event were best fitted by a stochastic acceleration spectral form; implying relativistic proton acceleration by processes associated with magnetic reconnection. This result suggests that two different mechanisms were involved in relativistic proton acceleration during the 14 July 2000 solar event.

THE 15 APRIL 2001 GLE

4.1 INTRODUCTION

The 15 April 2001 solar event produced an X14.4/2B solar flare and associated CME (1200 km s^{-1}) (Figure 4.1) which represented the largest of a series of solar eruptions that occurred during a period of intense solar activity extending from 28 March to 21 April 2001. This period produced seven M-Class and nine X-class flares. Several CMEs were observed with the *LASCO* coronagraphs (C2/C3) on board the *SOHO* spacecraft (Sun *et al.*, 2002). The primary source of this activity was NOAA active region 9415 located near the solar western limb S20°, W85° at the time of the event.

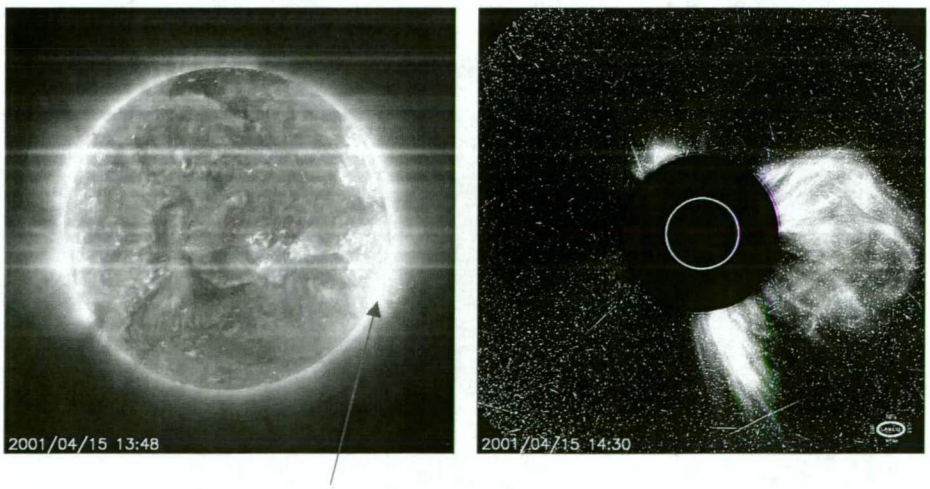

FIGURE 4.1: The 15 April 2001 solar flare as recorded by *EIT* on board *SOHO* at 171 Å (*left*). Source: http://soho.nascom.nasa.gov/hotshots/2001_04_15/eit195f1.gif/. The 15 April 2001 CME as recorded by the *LASCO/C2* coronagraph on board *SOHO* (*right*). Source: see Figure 1.1.

4.2 OBSERVATIONS

Soft X-rays observed by the *GOES 10* geostationary satellite commenced at 13:19 UT, peaking at 13:50 UT (Figure 4.2*a*). The *HXS* instrument on board *Yohkoh* first observed X-rays at 13:36 UT, peaking at 13:50 UT. CME onset (based on CME height-time measurements extrapolated back to the solar surface) is estimated at 13:32 UT (Bieber *et al.,* 2004; Gopalswamy *et al.,* 2003). During its propagation through the solar corona and interplanetary medium, the CME generated decametric to kilometric Type II radio emissions (*Waves* experiment (Bougeret *et al.,* 1995) on board the *Wind* spacecraft) and is interpreted as evidence of a shock. The interplanetary shock was detected *in situ* on 18 April 2001 at 00.50 UT by *Wind.* Gopalswamy *et al.* (2003) reported intense type III radio bursts from 13:40 to 14:54 UT. The *HEPAD* detectors on board *GOES 10* recorded sudden increases in relativistic protons (350-700 MeV) between 13:50 and 13:55 UT (Figure 4.2).

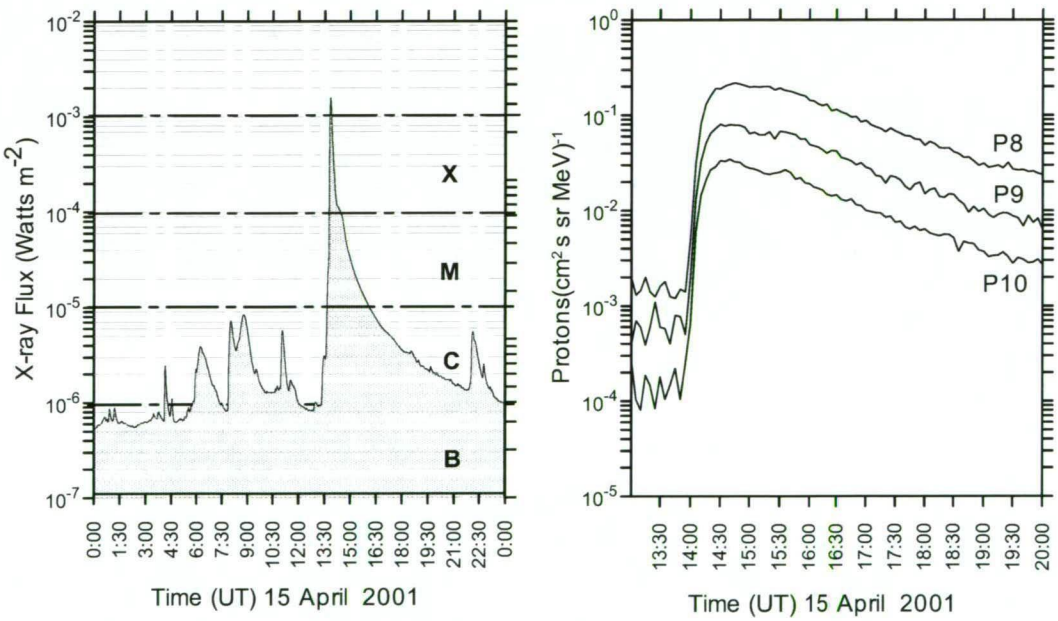

FIGURE 4.2: *GOES 10* observations of soft X-ray emissions at 1-8 Å (low energy channel) (*left*). Five minute *GOES 10* observations of relativistic proton fluxes (*right*). P8 to P10 represents the HEPAD detector differential energy channels (particles (cm^2 s sr MeV)$^{-1}$) with the following characteristics of nominal energy range (MeV): P8 = 350-420; P9 = 420-520; P10 = 510-700.

GLE onset was observed in neutron monitor data in the 1-minute interval commencing at 13:56 UT. The largest response was observed at South Pole with a maximum in 5-minute data of ~225% above the pre-increase level. The 15 April 2001 GLE is the second largest in terms of peak intensity for solar cycle 23. At 21:00 UT the increase above the galactic cosmic ray background was still 10%.

Corrections of observed increases to a standard sea-level atmospheric depth of 1033 g cm^{-2} were made with the following best fit attenuation lengths using the method of McCracken (1962*a*): 115 g cm^{-2} (from 14:00 to 14:15 UT), 110 g cm^{-2} (from 14:20 to 15:15 UT) and 100 g cm^{-2} (from 15:20 to 16:00 UT). GLE intensity/time profiles are presented in Figure 4.3.

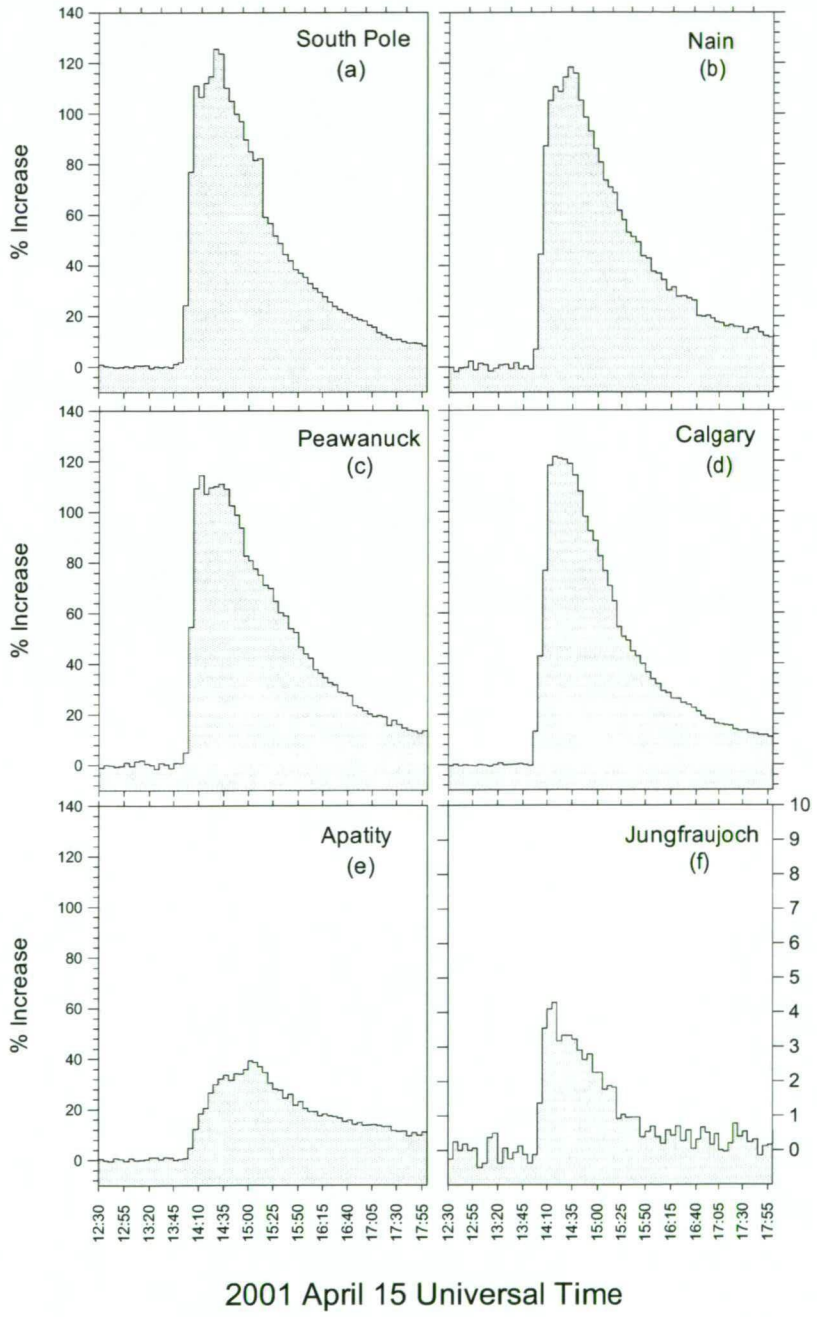

FIGURE 4.3: GLE intensity/time profiles for 15 April 2001 as recorded by (*a*) South Pole, (*b*) Nain, (*c*) Peawanuck, (*d*) Calgary, (*e*) Apatity and (*f*) Jungfraujoch neutron monitors. The viewing directions of the Peawanuck (4.3*c*) and Apatity (4.3*e*) neutron monitors approximately represent the sunward and anti-sunward field direction, respectively. The percentage increase for Jungfraujoch is shown on a different scale.

The rise to maximum intensity at South Pole (126% corrected to standard sea level pressure) took approximately 35 minutes (Figure 4.3*a*), suggesting that relativistic protons had reasonable access to Sun-Earth connecting field lines. The event was seen at Jungfraujoch (Figure 4.3*f*), indicating the presence of particles with rigidity of at least 4.5 GV. The Rome neutron monitor (with a geomagnetic cut-off of 6.3 GV and not shown in Figure 4.3) recorded an increase of marginal significance that may or may not be related to the GLE. Nain was found to have one of the largest responses (118%) and was used as the normalisation station for this analysis.

Figure 4.4 shows the viewing directions (in geographic coordinates) of selected neutron monitors at 14:30 UT. Note that Peawanuck (Figure 4.3*c*), with a viewing direction near the nominal sunward field direction, observed an earlier onset and more rapid rise than did Apatity (Figure 4.3*e*), whose viewing direction was near to the anti-sunward field direction.

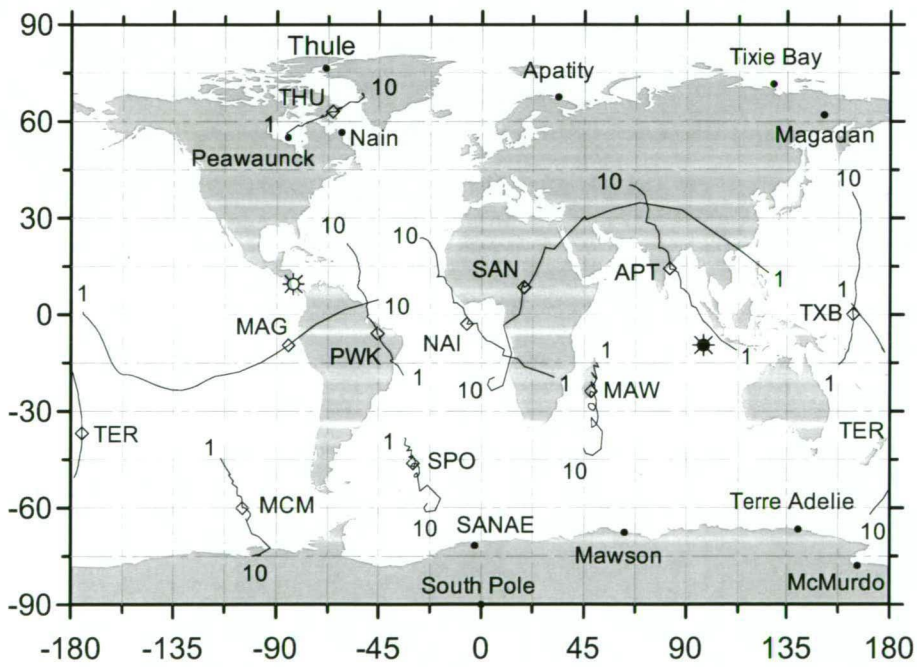

FIGURE 4.4: Viewing directions of neutron monitors in geographic coordinates at 14:30 UT (peak) on 15 April 2001. Geomagnetic conditions were slightly disturbed (Kp = 4; Dst = -15). Lines for each station represent the vertical viewing direction at different rigidities. '10' represents the vertical viewing direction at ~10 GV, while '1' represents the vertical viewing direction at the atmospheric cutoff (~1 GV). The open diamonds show the median rigidity of response to the GLE for each station. Star and filled star designate the position of the nominal and anti-sunward field direction respectively. Station abbreviations are: APT = Apatity, Russia; MAG = Magadan, Russia; MAW = Mawson, Antarctica; NAI = Nain, Canada; PWK = Peawanuck, Canada; MCM = McMurdo, Antarctica; SAN = SANAE, Antarctica; SPO = South Pole, Antarctica; TER = Terre Adélie, Antarctica; THU = Thule, Greenland; TXB = Tixie Bay, Russia.

4.3 MODELLING THE NEUTRON MONITOR RESPONSE

The geomagnetic field model described in section 2.2.4 was used to determine the asymptotic viewing directions of neutron monitors. Observations from 32 neutron monitors were modelled for every five-minute interval between 14:00 and 16:00 UT. Each indicated time represents the start of a five-minute integration interval. Table 4.1 shows the calculated percentage increase for time intervals which represent the rising (14:10 and 14:20 UT), peak (14:30 UT) and decline (14:45 UT) phases of the event along with the actual increases (corrected to a standard sea level atmospheric depth). Good fits to observations were achieved for most stations. However, the model underestimates the responses at Bern, Cape Schmidt, Peawanuck, Terre Adélie and Thule and overestimates the response at Apatity. Model fits to observations for time intervals not shown in Table 4.1 are presented in Appendix B.

4.3.1 *Arrival Directions*

Figure 4.5 illustrates the GSE longitude and latitude of the arrival direction, together with the IMF direction as measured by the *ACE* spacecraft.

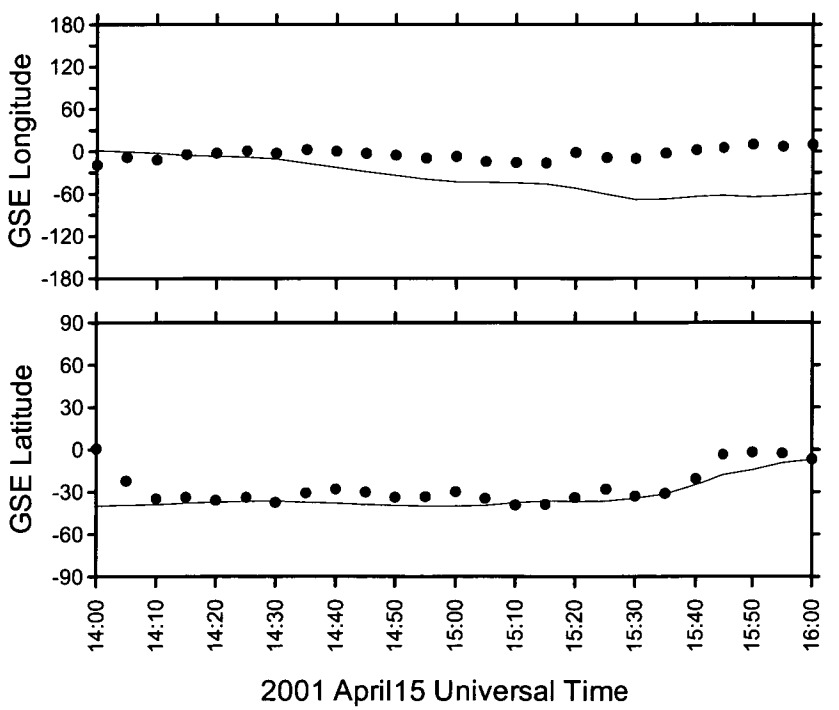

FIGURE 4.5: GSE longitude (*top*) and GSE latitude (*bottom*) of the apparent arrival directions (this study; solid circles) plotted with the negative magnetic field direction (1-hour centred moving averages) as measured by *ACE*.

TABLE 4.1

COMPARISON OF OBSERVED AND CALCULATED INCREASES FOR THE 15 APRIL 2001 GLE FOR THE MODIFIED POWER LAW FIT

Station	Lat.	Lon.	P_c [b]	Alt.	14:10 UT		14:20 UT		14:30 UT		14:45 UT	
	(deg.)	(deg.)	(GV)	(m)	Observed [c]	Calculated [d]	Observed [c]	Calculated [d]	Observed [c]	Calculated [d]	Observed [c]	Calculated [d]
Alma Ata.....	43.25	76.92	6.69	3340	1.4	0.3	1.3	0.2	1.3	0.7	0.7	0.6
Apatity.....	67.55	33.33	0.61	177	18.9	18.1	27.2	39.6	32.8	47.7	34.8	50.0
Athens.....	37.97	23.72	8.72	40	0.0	0.0	1.3	0.0	2.2	0.1	1.5	0.1
Bern.....	46.55	7.98	4.42	570	2.9	3.7	6.2	2.6	5.1	3.9	6.2	3.0
Calgary.....	51.08	245.87	1.09	1128	117.7	103.1	120.4	103.7	118.3	111.9	97.4	94.2
Cape Schmidt.....	68.92	180.53	0.45	0	21.1	14.9	44.3	29	54.0	40.8	60.7	49.7
Fort Smith.....	60.02	248.07	0.30	0	51.2	62.5	65.4	77.9	81.1	90.5	90.5	88.8
Irkustk.....	52.28	104.02	3.66	435	11.1	13.9	11.1	11.0	11.5	12.0	9.1	10.1
Jungfraujoch.....	46.55	7.98	4.48	3475	4.1	3.6	3.2	2.6	3.3	3.7	2.6	2.9
Kerguelen Island..	-49.35	70.25	1.19	33	8.9	11.1	25.6	23.9	38.6	35.0	44.8	39.0
Kiel.....	54.33	10.13	2.29	54	15.2	16.1	20.7	22.7	23.6	23.5	20.8	22.9
Kingston.....	-42.99	147.29	1.88	65	36.5	47.3	54.0	59.5	58.0	62.6	50.1	57.1
LARC.....	-62.20	301.04	2.21	40	16.4	15.4	19.3	18.4	18.6	19.6	13.6	15.9
Lomnický Štít.....	49.20	20.22	4.00	2634	5.2	6.5	5.2	5.5	4.7	6.6	3.7	5.6
Magadan.....	60.12	151.02	2.10	220	35.3	44.4	44.8	54.6	48.4	59.3	44.6	56.1
Mawson.....	-67.60	62.88	0.22	30	68.4	64.2	96.9	85.8	101.6	94.4	94.4	81.4
McMurdo.....	-77.85	166.72	0.01	48	76.7	77.1	78.9	85.4	94.1	96.6	76.0	86.7
Moscow.....	55.47	37.32	2.46	200	17.2	17.5	23	26.7	26.0	26.9	23.0	24.2
Nain [a].....	56.55	298.32	0.45	0	104.8	104.9	108.2	108.2	117.8	117.9	98.0	98.0
Newark.....	39.68	284.25	1.97	50	27.9	36.3	30	36.5	29.9	39.0	28.0	29.7
Norlisk.....	69.26	88.05	0.63	0	5.3	8.5	17.7	19.3	25.5	29.5	31.2	33.8
Novosibirsk.....	54.80	83.00	2.91	163	16.1	20.6	17.3	21.9	17.2	22.1	16.1	21.2
Oulu.....	65.05	25.47	0.81	15	27.3	21.2	45.5	43.2	53.4	50.8	45.8	51.6
Peawanuck.....	54.98	274.56	0.27	52	114.3	103.9	110.2	98.1	111.6	100.2	99.2	80.9
Potchefstrom.....	-26.68	27.10	7.30	1351	0.0	0.3	2.2	0.2	1.2	0.6	0.5	0.5
Rome.....	41.86	12.47	6.32	60	1.4	0.3	2.4	0.3	1.5	0.7	1.6	0.6
SANAE.....	-71.67	357.15	1.06	856	78.2	79.9	96.4	90.4	102.2	95	97.2	82.9
South Pole.....	-90.00	0.00	0.10	2820	111.2	112.7	112.6	110.3	126.2	121.6	105.4	99.7
Terre Adélie.....	-66.67	140.02	0.01	45	32.7	23.7	45.1	36.8	60.6	46.2	65.8	49.5
Thule.....	76.50	291.30	0.00	260	56.9	33.7	72.2	55.7	81.0	64.2	78.9	72.8
Tixie Bay.....	71.58	128.92	0.53	0	5.5	8.8	17.7	19.0	30.5	29.7	37.2	35.1
Yakutsk.....	62.03	129.73	1.70	105	16.5	21.4	40.7	40.6	41.0	52.5	44.8	58.3

[a] Normalisation station

[b] Nominal vertical geomagnetic cutoff rigidities represent the minimum rigidities below which particles do not have access to a particular site on the Earth's surface. The cut-off at the geomagnetic equator is ~ 17 GV, decreasing to zero at the geomagnetic poles.

[c] Actual % increases corrected to standard sea level atmospheric depth.

[d] Calculated % increases

The method of Bieber *et al.* (2002) was replicated to permit direct comparisons with *ACE* measurements. The average GSE longitude of the IMF direction as measured by *ACE* during the GLE was ~ 320°, which implies that particles were flowing (longitudinally) from the Sun close to a nominal Parker spiral (i.e., 315°, GSE coordinates). Between 14:00 and 14:30 UT the apparent longitude of the arrival direction is in good agreement with the measured field longitude. From 14:40 UT onwards, model longitudes begin to move east of the Sun-Earth line and by 16:00 the model longitudes are 60° east of the measured field longitude.

The latitude of the arrival direction near event onset (14:00 UT) was approximately 40° north of the measured field latitude. However, from 14:10 UT model latitudes are in good agreement with measured field latitudes. It is important to mention that model flow vectors need not align exactly with the measured magnetic field vector (see section 3.3.1). The uncertainty for the particle arrival direction at 14:15 UT is estimated to be ±2° in latitude and ±3° in longitude. At 16:00 UT these uncertainties are estimated to be ±12° in latitude and ±8° in longitude. Uncertainties for parameters at most other times will lie between these values.

4.3.2 *Pitch Angle Distributions*

The development of the pitch angle distribution during the 15 April 2001 GLE is presented in Figure 4.6 and the fitted parameters are listed in Table 4.2.

TABLE 4.2

PITCH ANGLE DISTRIBUTION PARAMETERS
15 APRIL 2001

Time [a] (UT)	A [b]	B [c]
14:00.....	0.387	0.512
14:10.....	0.753	0.591
14:15.....	1.112	0.720
14:20.....	1.564	0.836
14:30.....	1.611	1.043
14:45.....	2.990	1.366

[a] Time refers to the start of a five-minute interval.
[b] Parameter A has most effect on the width of the anisotropy.
[c] Parameter B has most effect on the relative flux in the reverse direction.

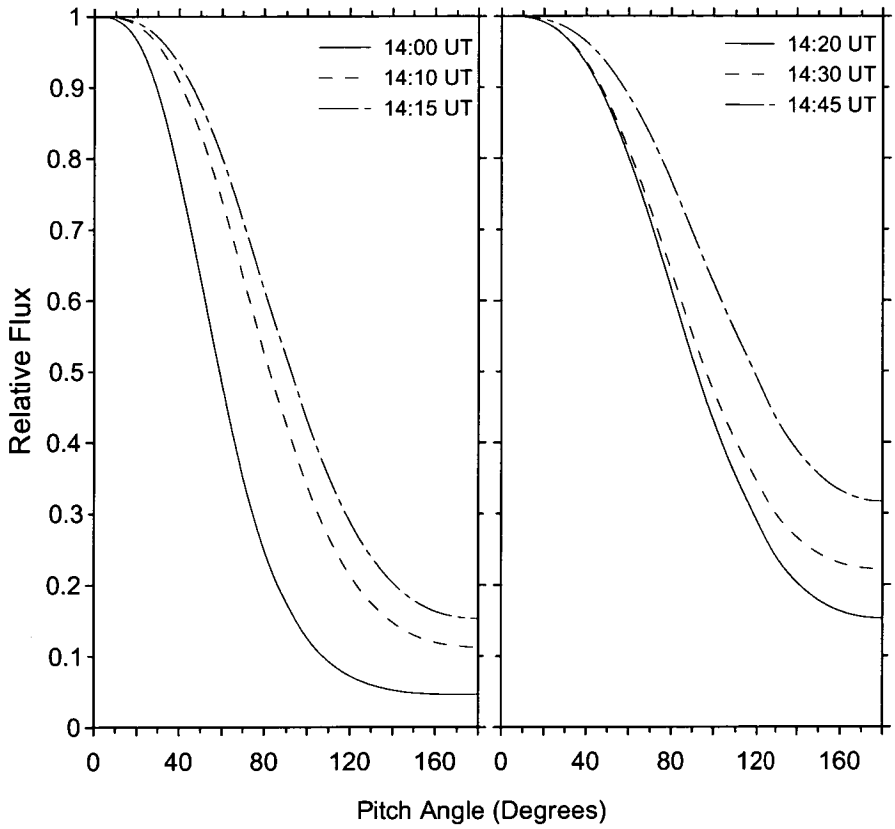

FIGURE 4.6: Derived pitch angle distributions for 14:00, 14:10, 14:15, 14:20, 14:30 and 14:45 UT during the GLE of 15 April 2001.

The particle arrival near onset (14:00 UT) was strongly anisotropic. The anisotropy decreased, albeit slowly, from 14:00 to 14:45 UT and remained relatively unchanged until at least 16:00 UT. This suggests that relativistic protons injected into the interplanetary medium were only moderately affected by local scattering associated with the IMF.

4.3.3 *Spectrum*

The spectral form used in this analysis was a modified power law in rigidity. The derived spectral parameters from 13:55 to 16:00 UT are presented in Table 4.3. A selection of the spectra is presented in Figure 4.7. At 14:00 UT (near onset) the spectral index was initially hard at -0.43 with a change of slope parameter ($\delta\gamma$) of 1.15. At 14:15 UT (rise phase) the spectral index was -2.70 with a $\delta\gamma$ of 1.43. At 14:30 UT (peak) the spectral index was softer at -4.76 with a $\delta\gamma$ of 0.60 and at 14:45 UT (fifteen minutes into the decline phase) the spectral index was -5.19 with a $\delta\gamma$ of 0.52.

TABLE 4.3

DERIVED SPECTRAL PARAMETERS

Time [a]	Inc [b]	$J_{\parallel}$ [c]	γ [c]	$\delta\gamma$ [e]
13:55.....	7.0	0.02	-0.41	0.39
14:00.....	44.3	0.62	-0.43	1.15
14:05.....	86.9	2.12	-0.01	2.06
14:10.....	104.8	6.73	-0.87	2.06
14:15.....	110.2	24.47	-2.70	1.43
14:20.....	108.2	31.64	-2.93	1.55
14:25.....	113.8	40.03	-3.12	1.61
14:30.....	117.8	90.07	-4.76	0.60
14:35.....	115.4	103.13	-4.91	0.69
14:40.....	104.7	83.25	-4.64	0.85
14:45.....	98.0	100.03	-5.19	0.52
14:50.....	92.5	117.82	-5.50	0.51
14:55.....	85.7	131.03	-5.90	0.29
15:00.....	80.4	118.48	-5.72	0.49
15:05.....	73.3	105.45	-5.60	0.62
15:10.....	70.5	113.79	-5.75	0.61
15:15.....	68.4	155.46	-6.62	0.00
15:20.....	61.8	116.95	-5.91	0.80
15:25.....	58.2	116.07	-6.16	0.47
15:30.....	53.1	90.38	-5.58	1.08
15:35.....	51.4	83.72	-5.62	0.89
15:40.....	49.3	81.99	-5.62	0.99
15:45.....	43.9	167.12	-6.83	0.11
15:50.....	42.9	190.10	-7.11	0.01
15:55.....	37.8	153.39	-6.99	0.01
16:00.....	37.0	149.02	-7.01	0.00

[a] Time (UT) refers to the start of a five-minute interval.
[b] Sea-level corrected percentage increases above the pre-event galactic cosmic ray background of the normalization station, Nain.
[c] Flux (particles $(cm^2 s\ sr\ GV)^{-1}$) at 1 GV summed over the forward steradian.
[d] Spectral slope (γ).
[e] Modified power law exponent modifier ($\delta\gamma$).

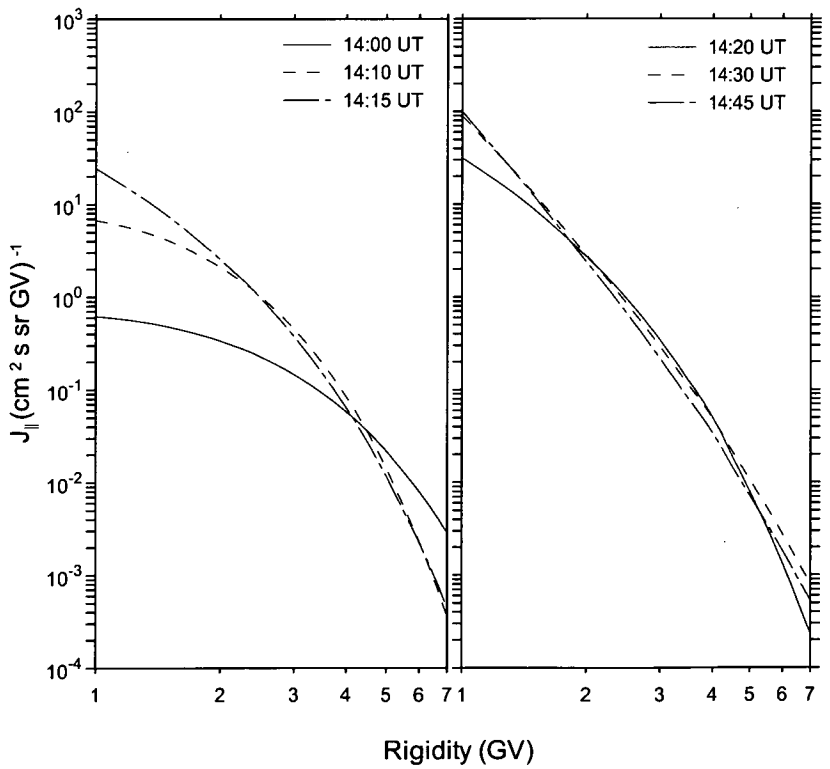

FIGURE 4.7: Derived modified power law rigidity spectra for 14:00, 14:10, 14:15, 14:20, 14:30 and 14:45 UT during the GLE of the 15 April 2001.

The uncertainty of the spectral slope (γ) at 14:15 UT is expected to exceed that at most other times due to the dominance of the particle anisotropy at this time. The spectral slope (γ) at 14:15 UT was -2.70 ±0.8 while at 16:00 UT γ was -7.1 ±0.3. The uncertainty in the change of slope ($\delta\gamma$) at 14:15 UT is 1.43 ±0.6. The uncertainty in the calculated flux at 1 GV is ~ 6%.

4.4 MODELLING PARTICLE ACCELERATION

The analytical spectra deduced from the neutron monitors were used to generate the input to the GNLS program with data points weighted by errors in the flux data. Best-fit variable model parameters derived from the program were used to generate theoretical shock and stochastic acceleration spectra up to 10 GeV.

4.4.1 *Results*

Tables 4.4 and 4.5 present the results of the analytical shock and stochastic (model B) acceleration model spectral fits to the data generated from the analytical fits to the neutron monitor observations at the rise (14:00, 14:10 and 14:20 UT), peak (14:30 UT), and decline (14:45 UT) phases. Figure 4.8 illustrates the results of these spectral fits at the rise (14:20 UT) and peak (14:30 UT) phases of the event. A Kolmogorov-Smirnov test at 95% confidence shows that all post-fit residuals were random, giving confidence in the weighted sum of squares result.

Table 4.4 lists the results and standard errors for the variable model parameters (compression ratio and *e*-folding energy E_0) from the shock acceleration non-linear least squares fitting routine.

TABLE 4.4 VARIABLE MODEL PARAMETERS:
SHOCK ACCELERATION, 15 APRIL 2001

Time [a] (UT)	r [b]	E_0 [c] (MeV)	WSS [d]
14:10.....	2.60 ±0.02	2667 ±107	835
14:20.....	2.05 ±0.02	3045 ±57	51
14:30.....	1.86 ±0.01	4104 ±30	10
14:45.....	1.83 ±0.01	3559 ±29	31

[a] Time refers to the start of a five-minute interval
[b] Shock compression ratio
[c] *e*-folding energy
[d] Weighted sum of squares

TABLE 4.5: VARIABLE MODEL PARAMETERS

STOCHASTIC ACCELERATION: NCS INJECTION

15 APRIL 2001

Time [a] (UT)	N [b]	α [c] (s^{-1})	WSS [d]
14:10	0.01 ±0.01	0.045 ±0.008	2976
14:20	0.05 ±0.01	0.041 ±0.002	251
14:30	0.20 ±0.03	0.036 ±0.001	84
14:45	0.30 ±0.01	0.035 ±0.001	54

[a] Time refers to the start of a five-minute interval
[b] Normalisation factor
[c] Acceleration efficiency
[d] Weighted sum of squares

The proton spectra during all phases of this event are best fitted with this spectral form, as is clear from a comparison with the weighted sums of squares for the stochastic acceleration model fits in Table 4.5.

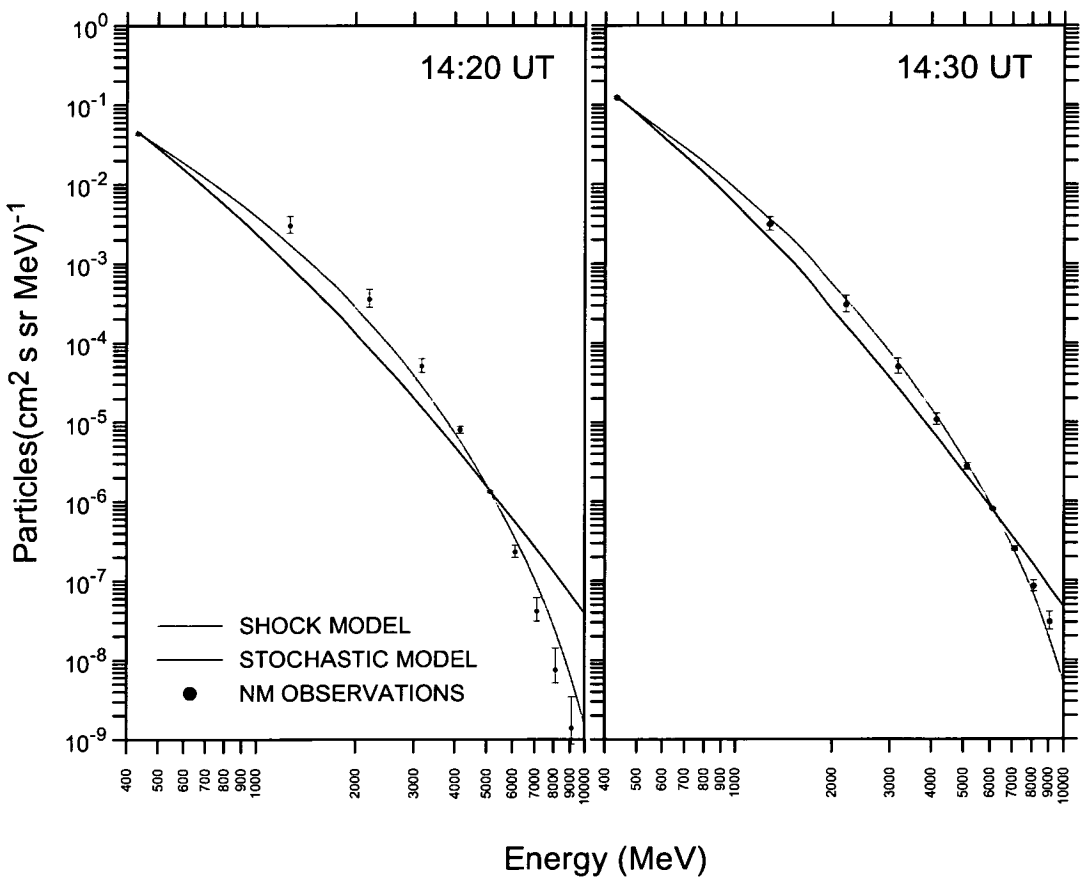

FIGURE 4.8: Energy spectral fits to flux values generated from ground-based neutron monitor observations (ranging from ~400 MeV to 10 GeV) for intervals 14:20 UT (*rising phase*) and 14:30 UT (*peak*). Fluxes (*black dots*) are shown with corresponding 1-sigma error bars. Fitted curves are of the Ellison & Ramaty (1985) shock acceleration (*light grey line*) and Gallegos-Cruz & Perez-Peraza (1995) stochastic acceleration (NCS injection) spectral forms (*black line*).

Figure 4.9 shows the residuals (calculated from the non-linear least squares fitting routine) plotted against kinetic energy and illustrates more clearly the improved fit of the Ellison & Ramaty (1985) shock acceleration model when compared to the Gallegos-Cruz & Perez-Pereza (1995) stochastic acceleration model (via NCS injection).

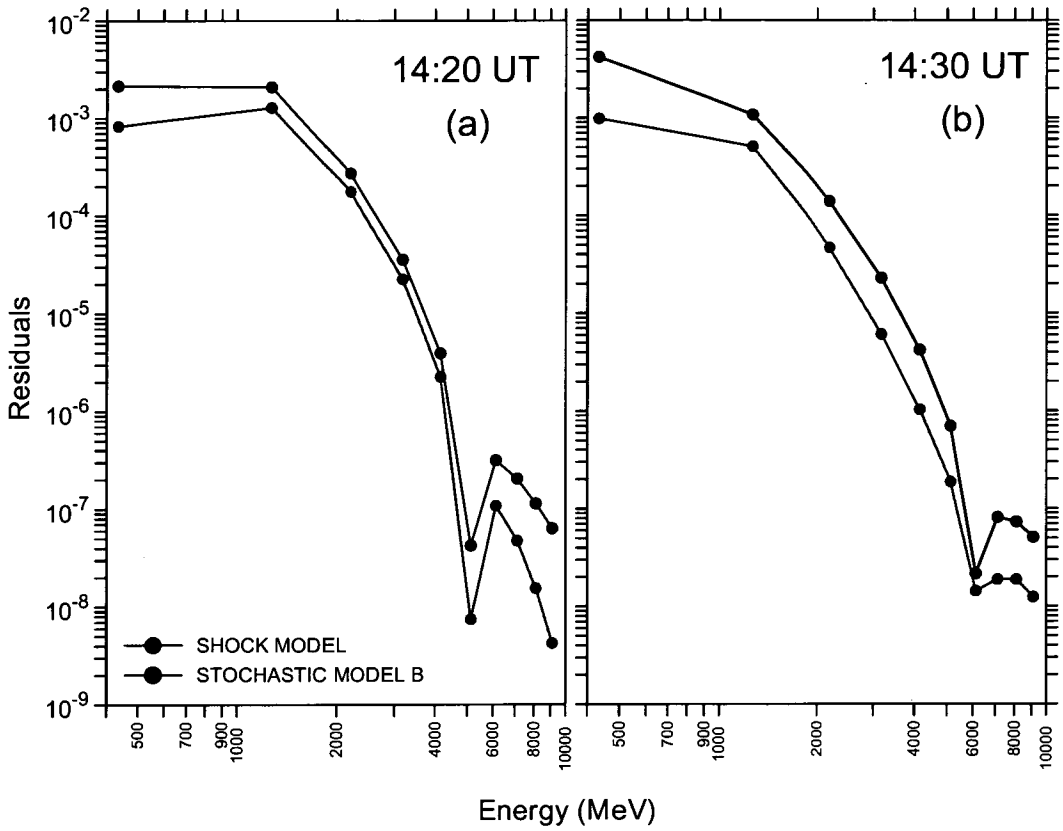

FIGURE 4.9: Least squares Y-residual plotted against kinetic energy for the 15 April 2001 GLE. These plots illustrate the better fit of the Ellison & Ramaty (1985) shock acceleration model (*light grey line*) as opposed to stochastic acceleration (NCS injection) model (*black line*): (*a*) 14:20 UT (*rising phase*), (*b*) 14:30 UT (*peak*).

4.5. SUMMARY

The arrival of relativistic protons at 1 AU for the 15 April 2001 GLE has been modelled using the global analysis technique described in Chapter 2. The largest neutron monitor response was observed at South Pole with a maximum in 5-minute data of ~225% above the pre-increase level. The event was seen at Jungfraujoch indicating the presence of particles with rigidity of at least 4.5 GV. The maximum intensity was reached in approximately 35 minutes. The event was marked by an anisotropic onset followed by a comparatively slow decrease in anisotropy. This

suggests that relativistic protons injected into the interplanetary medium were affected by minor degrees of local scattering.

Theoretical shock and stochastic acceleration spectral forms were employed to investigate the acceleration process. The spectra up to 10 GeV during the rising (14:10 UT), peak (14:30 UT) and declining (14:45 UT) phases of the event are best fitted by a shock acceleration spectral form. This implies that for the 15 April 2001 solar event protons were accelerated to relativistic energies by a CME-driven shock.

THE 20 JANUARY 2005 GLE

5.1 INTRODUCTION

The 20 January 2005 solar event produced the highest intensity of relativistic solar particles since the famous event on 1956 February 23. The largest 1-minute record at Terre Adélie was ~46 times the pre-event level. This is the largest sea-level increase since 1956 (Leeds ~47 times in 15-minute data). Furthermore, the location of X-ray and γ-ray emission was near to Sun-Earth connecting magnetic field lines (N14° W61°) providing the opportunity to directly observe the acceleration source from Earth.

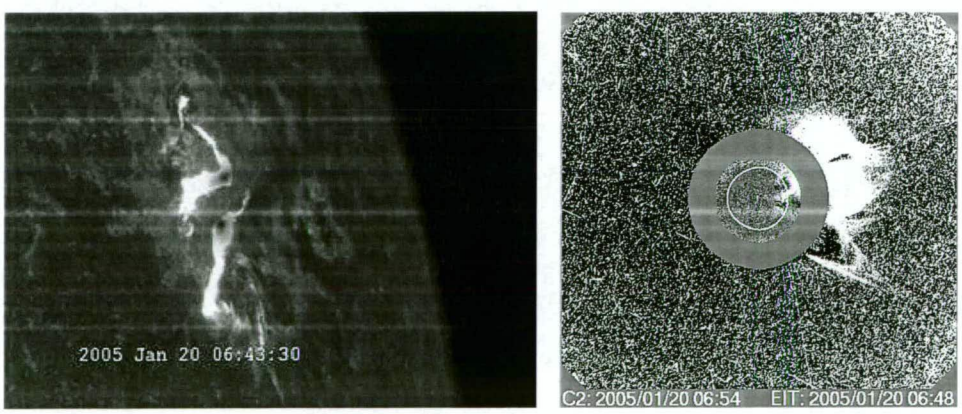

FIGURE 5.1: The 20 January 2005 solar flare as imaged by *TRACE* (*left*). Source: http://svs.gsfc.nasa.gov/vis/a000000/a003100/a003162/fast_closeHR.0141_web.jpg/. The 20 January 2005 CME as imaged by *LASCO/C2* coronagraph on board *SOHO* (*right*). Source: courtesy *ESA/NASA*

5.2 OBSERVATIONS

The 20 January 2005 solar event was associated with a *GOES*-classified X7.1/2B solar flare and fast CME (Figure 5.1). This event represented the largest of a series of solar eruptions that occurred during a period of intense solar activity

extending from 14 to 20 January. The primary source of this activity was NOAA active region 10720. The X-ray flare began at 06:36 UT and peaked at 07:01 UT (Figure 5.2). The CME was first detected by the *LASCO* instrument on board *SOHO* at 06:54 UT. Simnett (2006) estimated CME onset and speed at approximately 06:40 UT and 2500 km s^{-1} respectively. *RHESSI* (in Earth orbit) observed a peak in γ-ray emissions in the 4 to 7 MeV energy region at approximately 06:46 UT (Simnett 2006). The *SONG* instrument on board *CORONAS-F* observed γ-ray emissions with a time profile similar to *RHESSI*. Kuznetsov *et al.* (2005) suggested that protons with energies >300 MeV were accelerated at the Sun between 06:38:30 and 06:42:30 UT. The *HEPAD* detectors on board the *GOES 11* geostationary satellite recorded sudden increases in relativistic protons (510-700 MeV) between 06:45 and 06:50 UT (Figure 5.2).

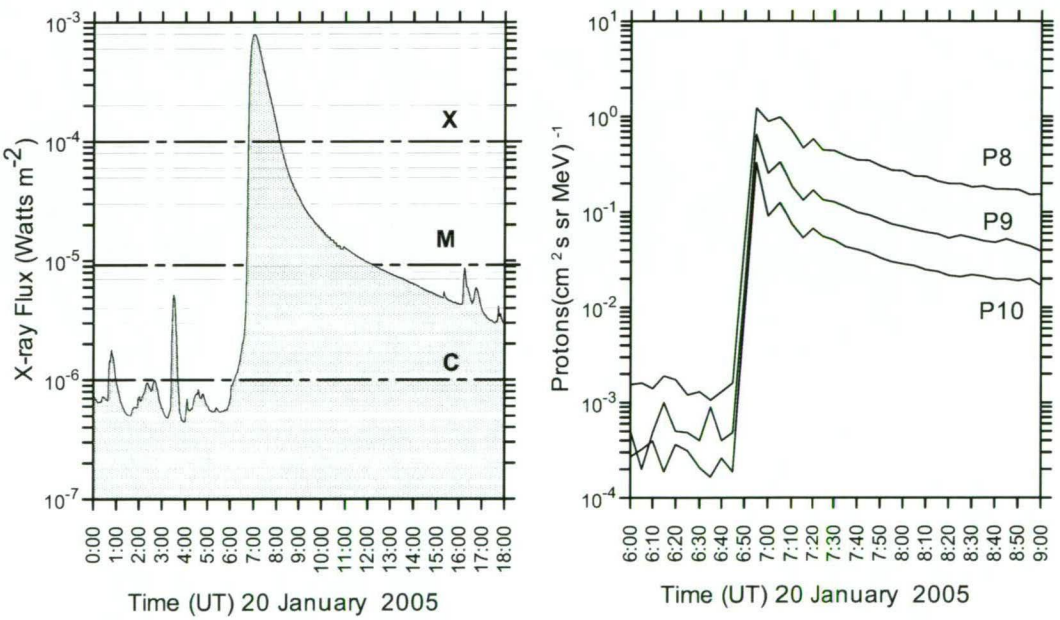

FIGURE 5.2: *GOES 11* observations of soft X-ray emissions at 1-8 Å (low energy channel) (*left*). Five-minute *GOES 11* observations of relativistic protons (*right*). P8 to P10 represent the *HEPAD* detector differential energy channels (particles (cm^2 s sr $MeV)^{-1}$) with the following characteristics of nominal energy range (MeV): P8 = 350-420; P9 = 420-520; P10 = 510-700.

GLE onset occurred at 06:48 UT in 1-minute neutron monitor data. The event had a rapid rise, peaking within 5 minutes at many stations, followed by a decay lasting many hours. At 14:00 UT the increase above the galactic cosmic ray background was still ~10% at Terre Adélie. The largest neutron monitor response was observed at the high-altitude station South Pole with a maximum in 1-minute

data of ~ 5440 % above the pre-increase level. The impulsive nature of the neutron monitor intensity/time profiles for Terre Adélie, McMurdo and South Pole, and the rapid rise (5 minutes) to maximum, is typical of well-connected events.

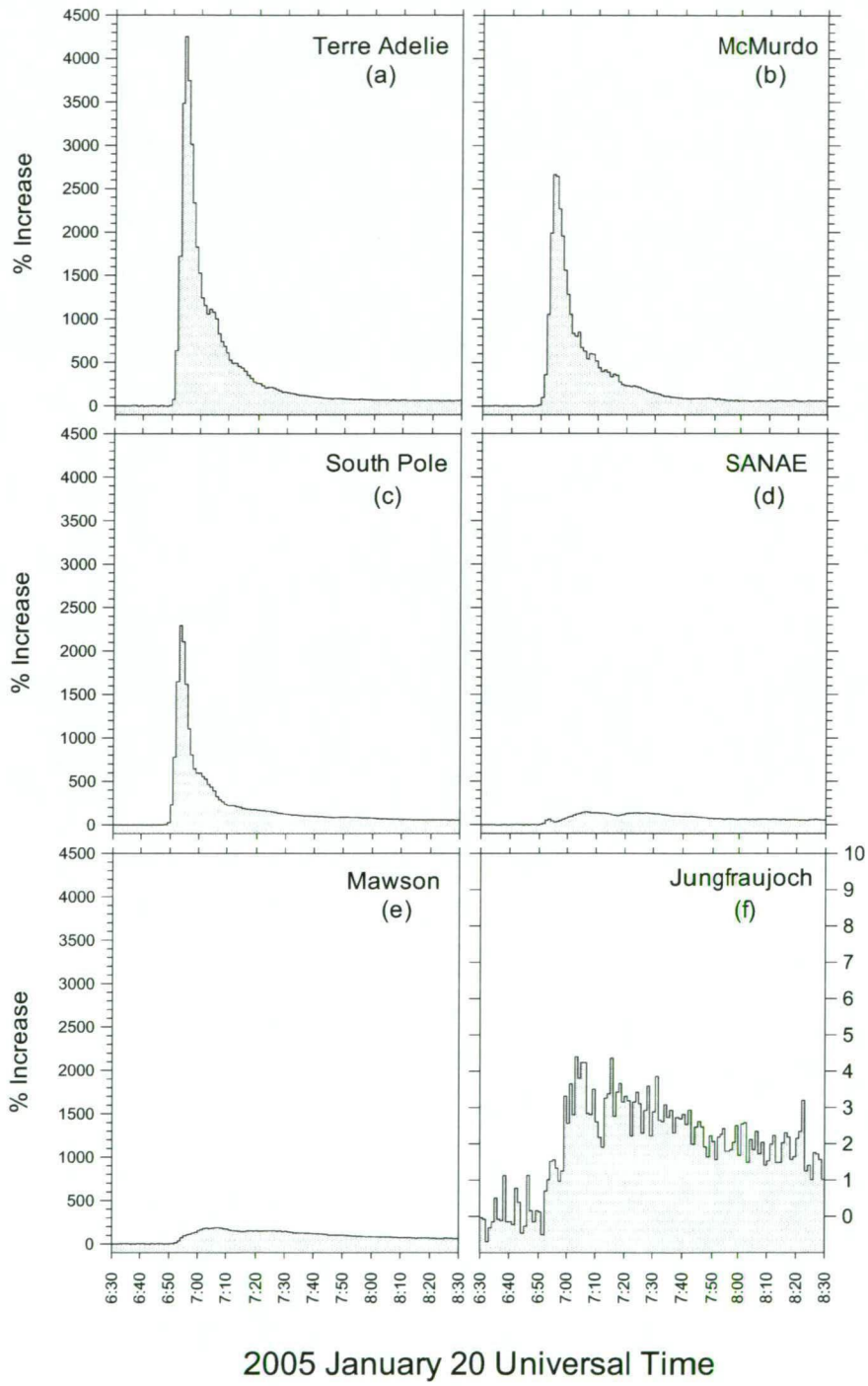

FIGURE 5.3: GLE profiles (corrected to sea-level pressure) for 20 January 2005 as recorded by the Terre Adélie, McMurdo, South Pole, SANAE, Mawson and Jungfraujoch neutron monitors. The percentage increase for Jungfraujoch is shown on a different scale.

The rapid rise seen in the Terre Adélie, McMurdo and South Pole neutron monitor intensity/time profiles (Figures 5.3*a*, *b* and *c*) indicates that relativistic protons had rapid access to Sun-Earth connecting field lines. Other neutron monitors recorded different responses (e.g. Figures 5.3*d*, *e* and *f*). The Erevan neutron monitor (cut-off 7.6 GV, altitude 3200 m) recorded a small but significant increase. Small increases were also seen by the Tibet neutron monitor (cut-off 14.1 GV, altitude 4300 m) (Myasaki *et al.,* 2005), the GRAND muon telescope (D'Andrea & Poirer 2005) and the Aragats muon detector (Bostanjyan *et al.*, 2007), indicating the presence of very low fluxes of particles >15 GeV.

The modelling of the sea-level neutron monitor response incorporated the Debrunner *et al.* (1982) yield function. Application of this function indicates that the low fluxes of higher rigidity particles observed in muons and at Tibet will not produce significant responses at other neutron monitors with high cut-offs. This is consistent with the results for spectra, pitch angle distributions and arrival directions obtained here.

Corrections of observed increases to a standard sea-level atmospheric depth of 1033 g cm^{-2} were made using the two-attenuation length method of McCracken (1962*a*). An attenuation length of 100 g cm^{-2} was derived from a comparison of Mt. Washington and Durham neutron monitors. The results presented in the following section were relatively insensitive to changes in the attenuation length (e.g., 90, 95 and 110 g cm^{-2}). After correcting the observed increases to standard sea-level atmospheric depth, Terre Adélie was found to have the largest response (Figure 5.3*a*) and was used as the normalisation station for this analysis. Figure 5.4 shows the viewing directions (in geographic coordinates) of selected neutron monitors at 06:55 UT (*peak*). *ACE* measurements indicate that the IMF direction was located at high southern latitudes (as indicated by the large black circle in Figure 5.4). This explains the substantial increases observed at Terre Adélie, McMurdo and South Pole stations (Figures 5.3*a*, *b* and *c*), whilst the very much smaller increases observed at SANAE and Mawson (Figures 5.3*d* and *e* respectively) indicate pitch angle distributions that are both extremely anisotropic and asymmetric.

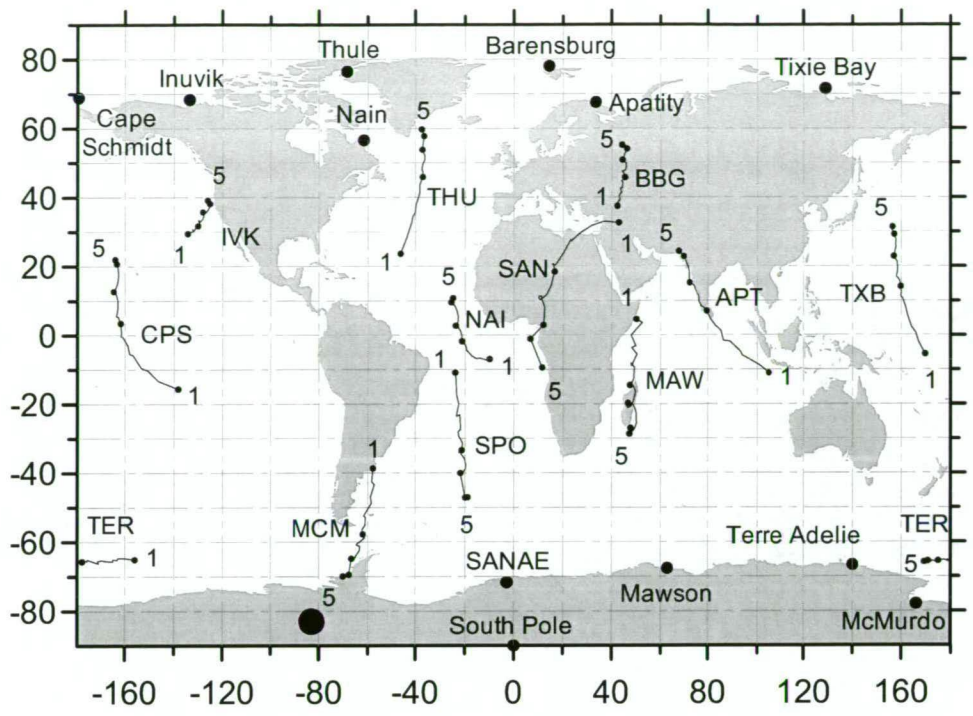

FIGURE 5.4: Viewing directions of neutron monitors in geographic coordinates at 06:55 UT (peak) on 20 January 2005. Geomagnetic conditions were relatively quiet (Kp = 2; Dst = -58). Lines for each station represent the vertical viewing direction at different rigidities. '5' represents the vertical viewing direction at maximum rigidity (~5 GV), while '1' represents the vertical viewing direction at the atmospheric cutoff (~1 GV). The small filled black circles represent 1 GV increments. The large filled black circle represents the IMF direction as measured by *ACE* at 06:55 UT. Station abbreviations are: APT = Apatity, Russia; BBG = Barentsburg, Russia; CPS = Cape Schmidt, Russia; IVK = Inuvik, Canada; MAW = Mawson, Antarctica; NAI = Nain, Canada; MCM = McMurdo, Antarctica; SAN = SANAE, Antarctica; SPO = South Pole, Antarctica; TER = Terre Adélie, Antarctica; THU = Thule, Greenland; TXB = Tixie Bay, Russia.

5.3 MODELLING THE NEUTRON MONITOR RESPONSE

The geomagnetic field model described in section 2.2.4 was used to determine the asymptotic viewing directions of the neutron monitors. Observations from 41 neutron monitors were modelled every five minutes between 06:50 and 08:00 UT. Tables 5.1, 5.2 and 5.3 show the observed percentage increase (corrected to standard sea-level atmospheric depth) for 5-minute time intervals over this period, along with the calculated increases. For the 5-minute interval 06:55 to 07:00 UT (Table 5.1) good fits to observations were achieved for stations which recorded large increases (e.g., McMurdo, South Pole and Nain). However, a number of stations are poorly modelled due to the difficulty the model had in accounting for the extreme asymmetric anisotropy of the event during this time interval. From 07:00 to 08:00 UT reasonable fits to observations were achieved.

TABLE 5.1

COMPARISON OF OBSERVED AND CALCULATED INCREASES FOR THE 20 JANUARY 2005 GLE FOR THE MODIFIED POWER LAW FIT

Station	Lat.	Lon.	P_c [b]	Alt.	06:50 UT		06:55 UT		07:00 UT		07:05 UT	
	(deg.)	(deg.)	(GV)	(m)	Observed [c]	Calculated [d]	Observed [c]	Calculated [d]	Observed [c]	Calculated [d]	Observed [c]	Calculated [d]
Alma Ata	43.25	76.92	6.69	3340	0	2.1	0.0	0.0	0.5	0.5	0.4	1.1
Apatity	67.55	33.33	0.61	177	10.2	9.5	107.7	112.5	169.5	183.5	164.4	167.6
Athens	37.97	23.72	8.72	40	0.2	0.8	2.5	0.0	1.2	0.1	0.9	0.3
Baksan	43.28	42.69	5.70	1700	0.3	2.2	0.0	0.0	2.1	0.8	1.3	1.7
Barentsburg	78.06	14.22	0.07	0.0	0.0	0.0	10.6	0.5	88.1	63.2	83.2	104.2
Bern	46.55	7.98	4.42	570	2.3	5.3	3.8	0.2	7.1	2.4	8.4	4.6
Calgary	51.08	245.87	1.09	1128	17.7	94.0	103	109.4	104.9	176.1	121.2	187.1
Cape Schmidt	39.37	253.82	3.03	3400	1.0	13.5	7.8	100.7	164.5	206.3	288.0	296.7
Climax	68.92	180.53	0.45	0.0	121.9	48.6	63.6	3.2	37.7	16.9	24.4	20.7
Durham	43.10	289.17	1.58	0.0	169.0	58.9	103.0	20.0	119.9	68.1	110.8	83.9
Erevan	40.50	44.17	7.58	3200	0.2	1.1	0.4	0.0	0.5	0.2	0.6	0.6
Fort Smith	60.00	258.10	0.30	0.0	23.1	2.7	128.9	38.3	233.0	146.6	253.5	215.0
Hermanus	-34.42	19.22	4.90	26	2.1	2.2	1.5	0.1	3.8	2.4	6.7	4.5
Inuvik	68.35	226.28	0.18	21	4.3	14.3	6.3	0.9	10.8	8.8	11.4	14.8
Irkustk	52.28	104.02	3.66	435	0.3	0.0	27.1	0.4	218.9	76.6	282.7	146.3
Jungfraujoch	46.55	7.98	4.48	3475	0.6	5.0	1.7	0.2	3.5	2.3	3.5	4.0
Kerguelen Island	-49.35	70.25	1.19	33	3.6	3.3	57.5	18.5	136.2	104.1	165.9	156.9
Kiel	54.33	10.13	2.29	54	12.2	18.7	47.7	5.6	83.7	34.5	87.5	50.2
Kingston	-42.99	147.29	1.88	65	2.3	10.0	21.2	20.5	75.4	75.3	116.1	96.3
LARC	-62.20	301.04	2.21	40	7.5	4.7	32.3	2.2	39.1	17.6	43.3	21.5
Lomnický Štít	49.20	20.22	4.00	2634	0.7	6.6	3.5	0.4	7.3	5.2	9.1	8.4
Magadan	60.12	151.02	2.10	220	0.8	78.4	14.5	24.7	50.9	84.6	90.3	119.5
Mawson	-67.60	62.88	0.22	30	25.4	265.6	114.3	213.2	172.7	233.7	183.4	172.0
McMurdo	-77.85	166.72	0.01	48	1234.6	1953.5	1946.1	2095	843.4	888.1	578.1	585.3
Mexico City	19.33	260.80	8.61	2274	0.6	1.9	0.3	0.0	1.0	0.2	0.9	0.4
Moscow	55.47	37.32	2.46	200	1.4	18.8	20.1	7.2	52.5	39.3	93.8	60.3
Mt. Washington	44.30	288.70	1.46	1909	169.6	74.1	125.9	36.3	134.5	104.7	124.8	101.1
Nain	56.55	298.32	0.45	0	67.9	37.2	268.3	273.6	218.2	207.6	211.1	168.5
Newark	39.68	284.25	1.97	50	87.2	42.5	68.3	8.6	82.3	38.0	75.5	41.3
Norlisk	69.26	88.05	0.63	0	9.9	6.2	66.8	70	126.0	180.1	128.6	207.9
Novosibirsk	54.80	83.00	2.91	163	0.0	20.0	7.7	3.4	23.1	26.2	53.3	42.8
Oulu	65.05	25.47	0.81	15	25.5	26.2	174.7	144.7	252.9	223.3	216.9	201.3
Potchefstrom	-26.68	27.10	7.30	1351	1.5	1.8	0.0	0.0	0.2	0.4	0.0	0.8
Rome	41.86	12.47	6.32	60	0.8	2.2	0.0	0.0	0.5	0.6	0.5	1.1
SANAE	-71.67	357.15	1.06	856	36.5	34.3	51.4	11.7	110.7	95.2	142.6	116.3
South Pole	-90.00	0.00	0.10	2820	1408.4	996.0	952.1	888.5	513.3	446.7	301.0	287.2
Terre Adélie[a]	-66.67	140.02	0.01	45	2034.5	2034.6	2490.5	2490.6	1130.3	1130.4	773.6	773.7
Thule	76.50	291.30	0.00	260	0.0	0.0	7.2	3.2	17.5	67.6	41.2	110.5
Tsumeb	-19.20	17.58	9.29	1240	0.1	0.4	0.0	0.0	0.0	0.1	0.4	0.2
Tixie Bay	71.58	128.92	0.53	0	0.0	1.7	52.1	28.2	179.1	145.2	203	211.1
Yakutsk	62.03	129.73	1.70	105	8.2	81.6	42.5	49.8	108.2	144.5	146.4	200.5

[a] Normalisation station. [b] Nominal vertical geomagnetic cutoff rigidities represent the minimum rigidities below which particles do not have access to a particular site on the Earth's surface. The cut-off at the geomagnetic equator is ~ 17 GV, decreasing to zero at the geomagnetic poles. [c] Actual % increases corrected to standard sea level atmospheric depth. [d] Calculated % increases

TABLE 5.2

COMPARISON OF OBSERVED AND CALCULATED INCREASES FOR THE 20 JANUARY 2005 GLE FOR THE MODIFIED POWER LAW FIT

Station	07:10 UT		07:15 UT		07:20 UT		07:25UT		07:30 UT		07:35 UT	
	Observed [b]	Calculated [c]	Observed [b]	Calculated [c]	Observed [b]	Calculated [c]	Observed [b]	Calculated [c]	Observed [b]	Calculated [c]	Observed [b]	Calculated [c]
Alma Ata	0.4	1.0	0.7	0.8	0.8	0.6	0.7	0.4	0.4	0.3	0.6	0.3
Apatity	147.1	146.0	133.2	133.6	139.6	134.8	126.9	130.7	109.6	118.6	98.8	108.1
Athens	0.0	0.3	1.8	0.2	1.1	0.2	1.4	0.1	0.0	0.1	0.0	0.1
Baksan	1.9	1.5	2.0	1.2	2.2	1.0	1.3	0.8	0.0	0.5	1.1	0.4
Barentsburg	87.2	111.2	94.3	111.3	110.4	124.2	117.6	114.5	104.5	100.9	92.1	89.5
Bern	5.4	4.1	5.5	3.7	3.7	3.3	5.6	2.6	4.8	1.9	4.8	1.7
Calgary	145.4	165.8	161.9	154.0	144.0	140.6	119.8	122.5	103.7	105.1	91.2	92.4
Cape Schmidt	205.7	221.4	176.7	183.8	137.0	134.5	121.6	116.7	104.4	100.1	88.1	84.1
Climax	15.9	19.7	12.3	18.6	9.0	16.5	7.9	14.6	7.0	11.0	6.2	9.8
Durham	94.6	72.5	87.0	64.3	80.3	66.2	72.5	63.4	64.2	54.5	55.7	46.8
Erevan	0.9	0.6	0.7	0.4	0.6	0.3	0.6	0.2	0.4	0.2	0.5	0.1
Fort Smith	198.3	180.7	164.4	164.4	150.2	132.4	127.4	115.0	108.9	99.1	87.5	83.4
Hermanus	7.0	3.9	6.4	3.2	6.1	2.7	3.0	2.1	2.6	1.5	4.3	1.2
Inuvik	8.5	13.5	7.9	11.3	7.7	9.9	6.1	7.4	5.8	5.4	5.2	4.4
Irkustk	222.1	136.7	176.7	131.6	137.7	124.5	114	114.3	93.3	99.8	80.8	83.4
Jungfraujoch	2.7	3.7	3.5	3.2	3.1	2.8	2.8	2.2	3.0	1.6	2.7	1.3
Kerguelen Island	150.4	141.6	150.0	131.0	135.5	126.8	119.5	113.6	101.1	100.1	88.0	85.8
Kiel	66.1	46.5	51.6	38.3	42.4	35.2	35.1	31.1	31.5	23.6	26.6	20.6
Kingston	96.0	88.5	85.4	79.7	75.9	72.1	63.1	61.2	51.7	56.5	47.4	45.8
LARC	32.0	22.1	26.8	20.5	23.6	19.1	22.6	16.1	20.4	14.0	18.9	12.7
Lomnický Štít	6.4	7.9	6.3	7.1	5.9	6.5	4.4	4.8	4.0	3.6	4.2	3.1
Magadan	76.6	97.0	65.4	84.9	57.8	69.5	46.4	59.0	37.6	49.3	32.3	42.9
Mawson	156.1	152.6	146.9	139.6	149.0	146.2	148.4	145.9	134.4	132.4	123.7	123.9
McMurdo	397	388.8	297.5	285.3	225.2	217.4	174.8	164.8	126.3	129.3	97.0	108.5
Mexico City	0.1	0.3	0.7	0.3	1.0	0.2	0.9	0.2	0.8	0.1	0.9	0.1
Moscow	80.9	50.9	58.0	43.7	49.6	40.7	40.2	32.3	32.8	26.4	28.5	24.6
Mt. Washington	105.2	95.0	97.0	88.4	97.3	93.8	88.7	78.6	80.0	74.8	69.2	66.5
Nain	187.3	152.5	171.8	145.4	171.5	145.4	157.2	131.6	141.2	114.6	130.2	104.0
Newark	59.4	38.9	51.7	36.6	46.8	35.6	39.3	29.3	34.9	25.8	30.1	22.2
Norlisk	129.0	167.7	125.7	146.1	108.3	131.7	98.6	121.5	83.9	106.7	72.3	92.6
Novosibirsk	39.6	37.1	32.3	30.2	27.2	26.7	22.0	21.5	18.8	16.1	16.4	14.8
Oulu	168.2	164.8	150.6	145.2	149.4	138.2	140.4	133.0	124.1	119.5	115.3	107.6
Potchefstrom	1.5	0.8	1.0	0.6	1.2	0.5	1.3	0.4	0.0	0.3	0.0	0.2
Rome	2.2	1.2	1.9	0.9	2.2	0.8	2.3	0.6	0.3	0.4	1.0	0.4
SANAE	131.0	118.6	110.8	117.3	134.6	129.0	133.3	120.7	120.5	107.1	102.1	98.1
South Pole	216.3	224.9	179.4	193.5	161.5	174.4	137.1	150.9	115.3	126.0	102.9	111.5
Terre Adélie[a]	479.7	479.8	319.9	320.0	223.6	223.6	174.8	174.8	136.8	136.8	111.0	111.1
Thule	71.7	114.9	86.3	115.4	100.7	124.8	114.4	113.9	114.5	98.9	103.7	83.8
Tsumeb	1.0	0.2	0.1	0.2	0.6	0.1	0.6	0.1	0.0	0.1	0.0	0.1
Tixie Bay	165.6	170.4	135.7	148.8	110.2	128.7	89.9	116.3	81.2	101.0	70.7	85.8
Yakutsk	124.4	159.2	111.8	139.5	99.2	116.0	83.9	101.9	67.9	85.1	55.6	75.7

[a] Normalisation station. [b] Actual % increases corrected to standard sea level atmospheric depth. [c] Calculated % increases

TABLE 5.3:
COMPARISON OF OBSERVED AND CALCULATED INCREASES FOR THE 20 JANUARY 2005 GLE FOR THE MODIFIED POWER LAW FIT

Station	07:40 UT		07:45 UT		07:50 UT		07:55UT		08:00 UT	
	Observed [b]	Calculated [c]	Observed [b]	Calculated [c]	Observed [b]	Calculated [c]	Observed [b]	Calculated [c]	Observed [b]	Calculated [c]
Alma Ata	0.6	0.2	0.2	0.2	0.3	0.3	0.2	0.4	0.2	0.5
Apatity	91.5	97.0	80.4	84.9	75.0	76.1	71.9	73.4	73.3	70.8
Athens	0.0	0.1	0.0	0.1	0.0	0.1	0.4	0.1	0.0	0.1
Baksan	1.7	0.4	0.3	0.3	0.9	0.4	1.2	0.6	0.7	0.7
Barentsburg	77.0	82	63.9	71.0	55.8	65.1	49.8	63.4	51.0	63.4
Bern	4.0	1.4	3.9	1.4	4.2	1.5	4.3	2.0	3.5	2.3
Calgary	82.9	83.4	74.1	74.4	66.1	69.2	63.1	65.9	62.3	63.5
Cape Schmidt	73.3	71.4	62.7	63.0	58.9	59.9	60.3	59.2	65.3	59.3
Climax	6.3	9.4	4.4	8.9	4.9	8.7	3.3	10.9	5.3	10.4
Durham	49.9	41.2	45.0	36.0	41.7	37.7	41.4	36.6	42.0	36.8
Erevan	0.1	0.1	0.3	0.1	0.4	0.1	0.1	0.2	0.2	0.3
Fort Smith	76.1	71.3	69.4	63.0	70.1	60.0	67.4	59.2	64.3	59.3
Hermanus	3.7	1.2	3.5	1.0	2.6	1.2	4.0	1.6	2.7	1.9
Inuvik	5.5	4.1	5.1	3.8	5.9	4.1	6.1	4.9	5.3	6.0
Irkustk	71.8	71.4	65.8	62.7	66.0	60.7	61.3	59.7	62.0	60.1
Jungfraujoch	2.5	1.2	2.2	1.2	2.1	1.2	2.0	1.9	2.1	2.1
Kerguelen Island	79.1	74.8	72.6	64.9	66.8	61.9	68.3	60.7	64.9	60.2
Kiel	23.6	17.9	22.0	15.5	20.8	16.1	21.2	18.1	23.5	19.6
Kingston	39.1	38.8	35.9	37.2	36.5	34.1	38.0	35.7	37.8	37.7
LARC	17.2	10.1	13.8	10.1	15.9	10.4	14.9	11.6	13.4	11.7
Lomnický Štít	3.3	2.6	3.3	2.7	4.2	2.9	4.8	3.7	4.5	4.3
Magadan	30.0	38.9	28.0	38.3	29.6	36.3	31.7	34.0	32.2	36.2
Mawson	114.9	114.9	102.9	103.1	95.2	97.4	85.1	88.8	79.7	82.2
McMurdo	85.6	92.8	86.6	85.6	78.0	79.9	65.2	74.3	60.1	66.8
Mexico City	1.3	0.1	0.6	0.1	1.5	0.1	0.4	0.2	0.6	0.2
Moscow	24.6	20.9	22.5	18.4	22.2	19.5	22.9	21.9	24.3	20.5
Mt. Washington	61.7	63.1	53.8	49.9	50.9	51.7	46.8	50.7	44.6	50.6
Nain	117.4	97.3	107.7	87.9	99.4	81.9	90.8	74.8	83.6	69.6
Newark	29.1	20.7	27.0	18.1	23.0	18.4	25.3	19.8	25.3	21.4
Norlisk	64.0	79.2	59.6	69.4	58.4	63.6	56.4	63.0	56.1	62.3
Novosibirsk	14.4	12.1	13.4	12.5	13.7	12.6	17.0	13.8	16.8	13.9
Oulu	105.7	95.2	93.4	83.8	86.8	75.7	86.3	73.4	78.4	70.6
Potchefstrom	0.2	0.2	0.4	0.2	0.5	0.2	1.1	0.3	0.0	0.4
Rome	0.3	0.3	0.1	0.3	1.4	0.4	1.7	0.5	1.7	0.6
SANAE	93.5	92.4	79.5	81.1	69.2	74.5	65.4	70.9	63.6	69.0
South Pole	93.8	101.1	85.8	93.0	85.6	88.5	80.5	79.9	71.9	71.6
Terre Adélie[a]	90.8	90.8	83.1	83.1	76.0	76.1	72.8	72.8	66.1	66.1
Thule	86.5	73.4	68.4	64.5	64.8	60.8	61.8	59.7	61.3	59.7
Tsumeb	0.3	0.0	0.0	0.0	0.1	0.1	0.3	0.1	0.0	0.1
Tixie Bay	61.5	72.8	53.7	64.0	45.9	60.2	48.3	59.7	49.7	59.7
Yakutsk	47.9	65.6	44.1	58.2	43.5	56.2	48.2	54.5	50.9	53.7

[a] Normalisation station. [b] Actual % increases corrected to standard sea level atmospheric depth. [c] Calculated % increases

5.3.1 *Arrival Directions*

Figure 5.5 illustrates the GSE longitude and latitude of the arrival directions, together with the IMF direction as measured by *ACE*. The average GSE longitude of the IMF direction as measured by *ACE* during the first 35 minutes of the event was ~ -60°. This implies that particles were flowing from the Sun (longitudinally) close to a nominal Parker spiral (i.e., -45°, GSE coordinates). At 06:55 and 07:00 UT the apparent arrival longitude is in good agreement with the measured field longitude. However, there is inconsistency between the apparent and the measured longitude of the field direction from 07:05 UT onwards. By 07:30 UT the model longitude is approximately 60° east of the measured field longitude.

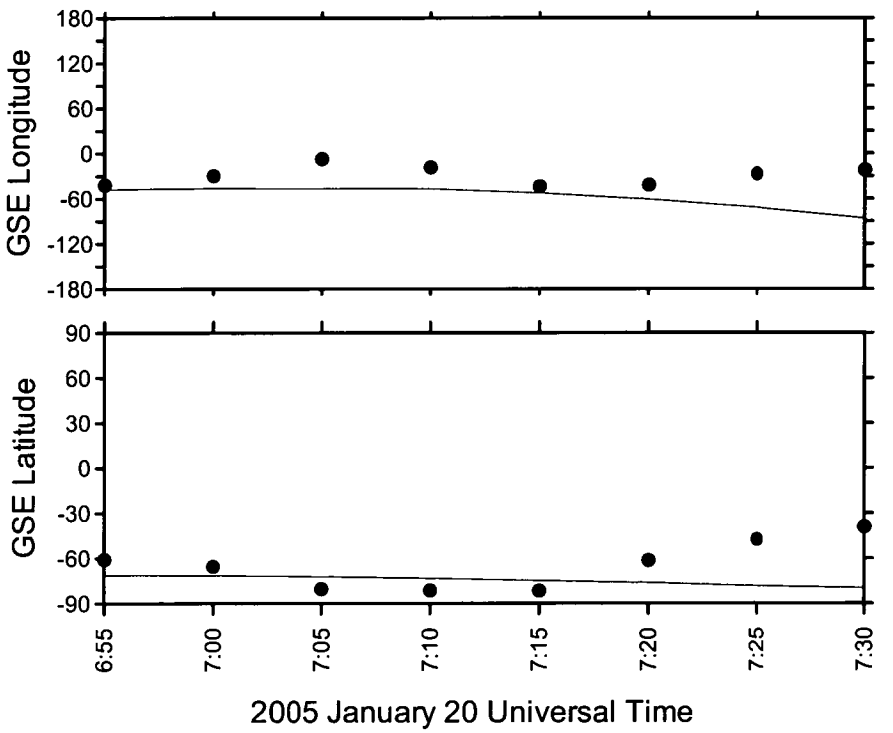

FIGURE 5.5: GSE longitude (*top*) and GSE latitude (*bottom*) of the arrival directions (*solid circles*) plotted with the negative magnetic field direction (1-hour centred moving averages) as measured by the *ACE* spacecraft (*solid line*).

From 06:55 to 07:15 UT the latitude of the arrival direction is in good agreement with the measured field latitude (i.e., centred at high southern latitudes in GSE coordinates). However, from 07:15 UT the apparent latitude began to move north, and by 07:30 UT the apparent latitude is approximately 45° north of the measured field latitude. It is important to mention that model flow vectors need not

align with the measured magnetic field vector (see section 3.3.1). The uncertainty for the particle arrival direction at 06:55 UT is estimated to be ±1° in latitude and ±18° in longitude. At 08:00 UT the uncertainty is estimated to be ±10° in latitude and ±21° in longitude. Uncertainties for parameters at most other solutions will lie between these values.

5.3.2 *Pitch Angle Distributions*

The temporal development of the pitch angle distribution during GLE is presented in Figure 5.6 and the fitted parameters are listed in Table 5.4. The particle distribution can be divided into an anisotropic component (representing particles which arrive directly from the Sun) and an isotropic component (where the effects of local scattering dominate the distribution). The particle arrival at the peak (06:55 UT) was strongly anisotropic (Figure 5.6). This suggests that initially relativistic protons injected into the interplanetary medium arrived directly from the Sun without being affected by local scattering. However, the degree of anisotropy decreased and by 08:00 UT, well into the decline phase, there is evidence for significant scattering.

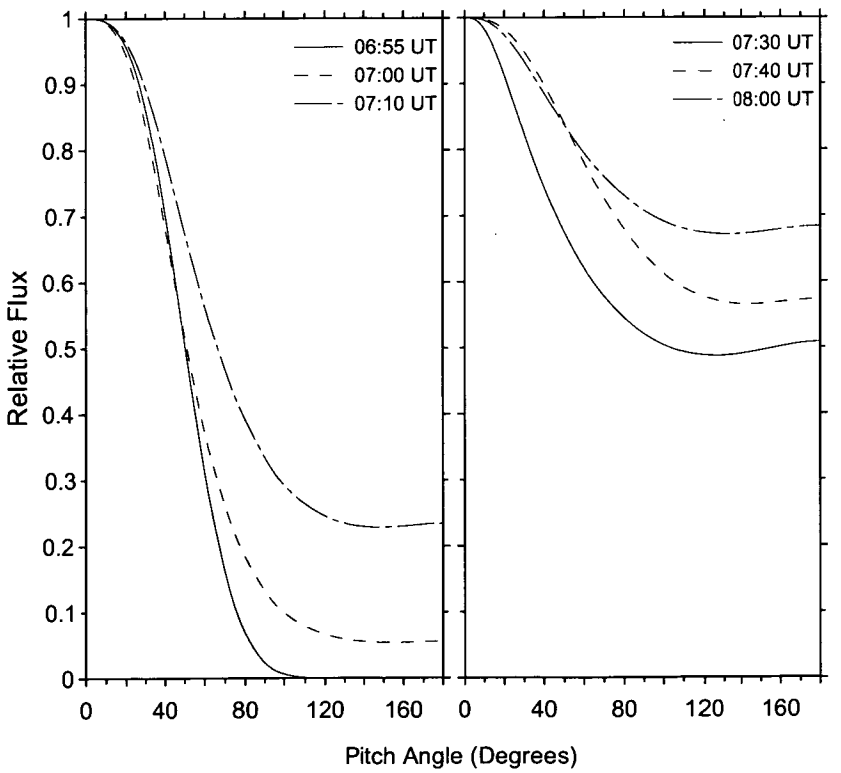

FIGURE 5.6: Derived pitch angle distributions for 06:55, 07:00, 07:10, 07:30, 07:40 and 08:00 UT, during the GLE of 20 January 2005.

TABLE 5.4

PITCH ANGLE DISTRIBUTION PARAMETERS
20 JANUARY 2005

Time [a] (UT)	A [b]	B [c]
06:55.....	0.319	0.010
07:00.....	0.287	0.504
07:10.....	0.354	1.082
07:30.....	0.085	2.321
07:40.....	0.713	2.820
08:00.....	0.408	4.128

[a] Time refers to the start of a five-minute interval.
[b] Parameter A has most effect on the width of the anisotropy.
[c] Parameter B has most effect on the relative flux in the reverse direction.

5.3.3 *Spectrum*

The spectral form used in this analysis is a modified power law in rigidity, as described in section 2.2.10. Particle spectra derived between 06:50 and 07:15 UT are illustrated in Figure 5.7 and fitted parameters are presented in Table 5.5.

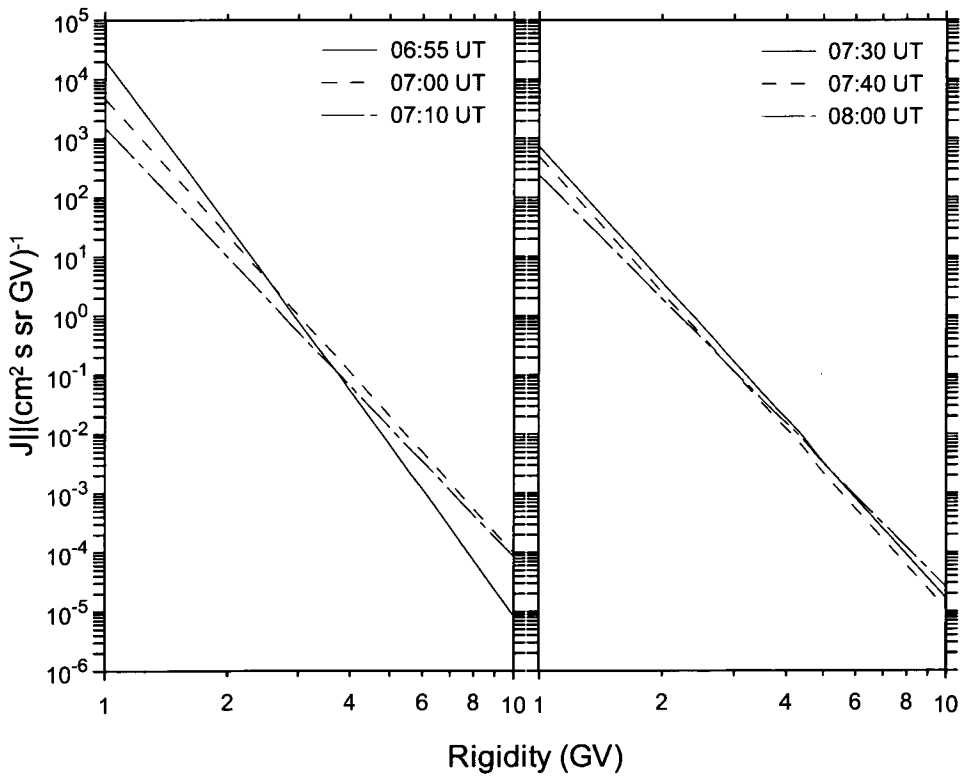

FIGURE 5.7: Derived modified power law rigidity spectra for 06:55, 07:00, 07:10, 07:30, 07:40 and 07:15 UT, during the GLE of 20 January 2005.

Model fits to observations for the 06:50 to 06:55 UT interval (rising phase) had large residuals for some stations, due to the extreme asymmetric anisotropy. Nonetheless, the model produced a spectral index (γ) of -5.5 with a small change of slope parameter ($\delta\gamma$) of 0.04. At 06:55 UT (peak) the spectral index was very soft at -9.2±0.6, again with a small change of slope parameter ($\delta\gamma$) of 0.07. The index hardened during the declining phase, ranging from -7.7±0.5 at 07:00 UT to -7.0±0.4 an hour later, with $\delta\gamma$ having insignificant values. These spectra agree with results reported by Bütikofer *et al.* (2006) and Plainaki *et al.* (2007). The uncertainty of the spectral index (γ) at 06:55 UT (peak) is expected to exceed that at most other times due to the dominance of the particle anisotropy at this time (see discussion section 3.4). The uncertainty in the change of slope ($\delta\gamma$) for this period was negligible. The uncertainty in the calculated flux at 1 GV is less than 10 %.

TABLE 5.5

DERIVED SPECTRAL PARAMETERS

Time [a]	Inc [b]	J_{II} [c]	γ [c]	$\delta\gamma$ [e]
06:50.....	2034.5	2244.2	-5.54	0.04
06:55.....	2490.5	20451.4	-9.19	0.07
07:00.....	1130.3	4694.3	-7.68	0.00
07:05.....	773.6	2531.8	-7.35	0.00
07:10.....	479.7	1505.1	-7.25	0.00
07:15.....	319.9	1058.4	-7.31	0.01
07:20.....	223.6	825.1	-7.28	0.02
07:25.....	174.8	823.3	-7.47	0.00
07:30.....	136.8	723.4	-7.64	0.00
07:35.....	111.0	562.0	-7.64	0.00
07:40.....	90.8	489.8	-7.65	0.00
07:45.....	79.5	440.2	-7.59	0.00
07:50.....	69.2	402.8	-7.40	0.00
07:55.....	72.8	306.8	-7.16	0.00
08:00.....	66.1	239.2	-7.00	0.00

[a] Time (UT) refers to the start of a five-minute interval.
[b] Sea-level corrected percentage increases above the pre-event galactic cosmic ray background of the normalization station, Terre Adélie.
[c] Flux in particles $(cm^2\ s\ sr\ GV)^{-1}$ at 1 GV summed over the forward steradian.
[d] Spectral slope (γ).
[e] Modified power law exponent modifier ($\delta\gamma$).

5.4 MODELLING PARTICLE ACCELERATION

The analytical spectra deduced from the neutron monitors were used to generate the input to a generalised non-linear least squares program with data points weighted by errors in the flux data. Best-fit variable model parameters derived from this program were re-input into the Ellison and Ramaty (1985) theoretical shock acceleration model (equation 2.23) and the Gallegos-Cruz & Perez-Pereza (1995)

theoretical stochastic acceleration model B (equation 2.28) to generate analytical spectra up to 10 GeV.

5.4.1 *Results*

Tables 5.6 and 5.7 present the results of the spectral fits to the data generated from the analytical fits to the neutron monitor observations for this GLE, at the peak (06:55 UT) and declining (07:10 UT) phases, while Figure 5.8 illustrates these results.

TABLE 5.6: VARIABLE MODEL PARAMETERS:
SHOCK ACCELERATION, 20 JANUARY 2005

Time [a] (UT)	r [b]	E_0 [c] (MeV)	WSS [d]
06:55.....	1.417 ±0.002	5116 ± 500	28
07:00.....	1.491 ±0.003	9372 ± 1213	36
07:10.....	1.559 ±0.005	6383 ± 685	53
07:20.....	1.602 ±0.006	4432 ± 402	78
07:30.....	1.609 ±0.007	3525 ± 309	116
07:45.....	1 514 ±0.010	3075 ± 258	142
08:00.....	1.723 ±0.013	3371 ± 282	174

[a] Time refers to the start of a five-minute interval
[b] Shock compression ratio
[c] e-folding energy
[d] Weighted sum of squares

TABLE 5.7: VARIABLE MODEL PARAMETERS
STOCHASTIC ACCELERATION
NEUTRAL CURRENT SHEET INJECTION, 20 JANUARY 2005

Time [a] (UT)	N [b]	α [c] (s^{-1})	WSS [d]
06:55.....	1985 ±96	0.0146 ±0.0001	2
07:00.....	72 ±4.0	0.0215 ±0.0003	6
07:10.....	14 ±1.0	0.0242 ±0.0003	6
07:20.....	8 ±1.0	0.0238 ±0.0002	6
07:30.....	11 ±1.0	0.0218 ±0.0002	6
07:45.....	2 ±0.4	0.0221 ±0.0002	6
08:00.....	8 ±0.1	0.0263 ±0.0003	8

[a] Time refers to the start of a five-minute interval
[b] Normalisation factor
[c] Acceleration efficiency
[d] Weighted sum of squares

A Kolmogorov-Smirnov test at 95% confidence shows that all post-fit residuals were random, giving confidence in the weighted sum of squares result. Table 5.7 lists

the results and standard errors for the variable model parameters (normalisation factor N and acceleration efficiency α) from the stochastic acceleration non-linear least squares fitting routine. The proton spectra during the peak (06:55 UT) and decline (07:00 to 08:00 UT) phases are best fitted with this spectral form, implying proton acceleration by processes resulting from magnetic reconnection.

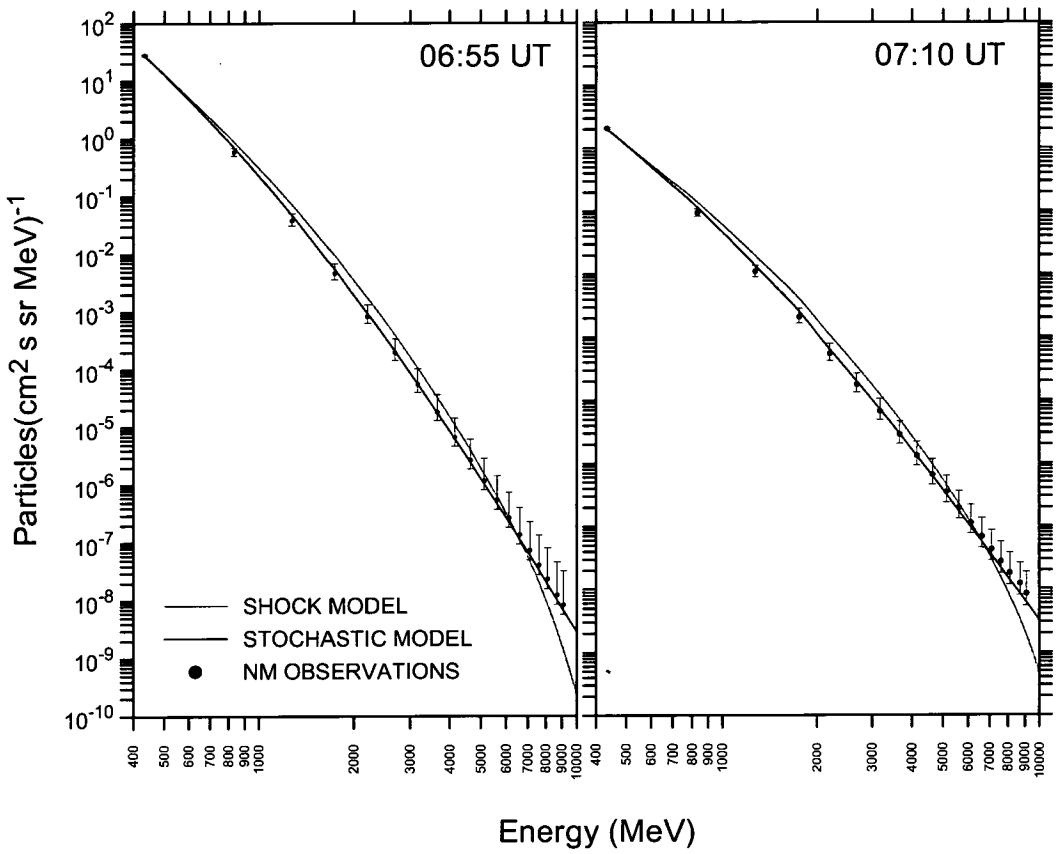

FIGURE 5.8: Energy spectral fits to flux values generated from ground-based neutron monitor observations (ranging from ~400 MeV to 10 GeV) for intervals 06:55 UT (*peak*) and 07:10 UT (*declining phase*). Fluxes (*black dots*) are shown with corresponding 1-sigma error bars. Fitted curves are of the Ellison & Ramaty (1985) shock acceleration (*light grey line*) and the Gallegos-Cruz & Perez-Peraza (1995) stochastic acceleration (NCS injection) spectral forms (*black line*).

Figure 5.9 shows the residuals (calculated from the GNLS fitting routine) plotted against particle energy and illustrate more clearly the better fit of the stochastic acceleration model compared to the shock acceleration model. For the time intervals modelled, the acceleration efficiency α ranged from 0.01 to 0.03 s^{-1}, which is consistent with values reported in previous studies (Miller, Guessoum & Ramaty 1990; Miller 1991).

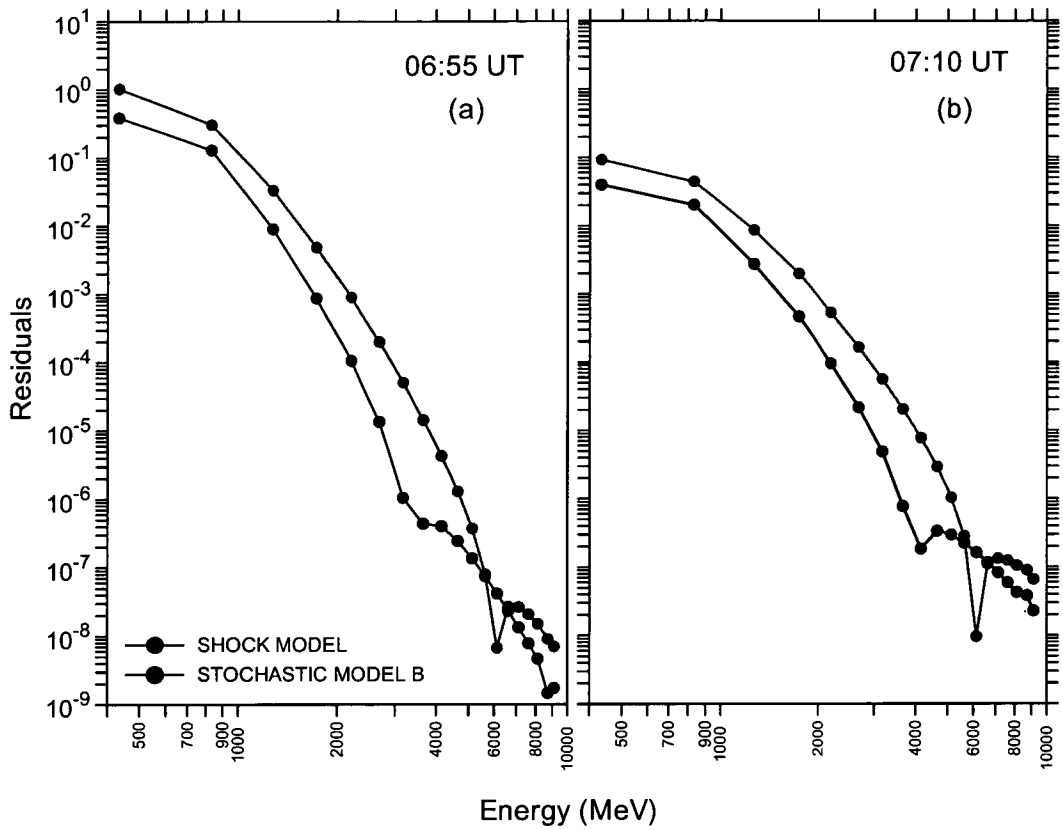

FIGURE 5.9: Least squares Y-residual plotted against kinetic energy for the 20 January 2005 GLE. These plots illustrate the better fit of the Gallegos-Cruz & Perez-Peraza (1995) stochastic acceleration model (*black line*) as opposed to the Ellison & Ramaty (1985) shock acceleration model (*light grey line*): (*a*) 06:55 UT (*peak*), (*b*) 07:10 UT (*declining phase*).

5.5. SUMMARY

The 20 January 2005 GLE had an extremely impulsive onset as shown by the neutron monitor intensity/time profiles and a rapid rise to maximum (approximately 5 minutes). The GLE event was marked by a highly anisotropic onset followed by a fairly rapid decrease in anisotropy. This indicates that initially, particles injected into the interplanetary medium propagated to Earth essentially scatter-free. However, there is evidence to suggest that particles arriving at Earth shortly after were affected by significant degrees of scattering.

Model-derived and *ACE* measurements of the IMF direction indicate an initial source of relativistic particles arriving at high southern latitudes. This explains the substantial increases observed at Terre Adélie, McMurdo and South Pole stations, whilst the very much smaller increases observed at SANAE and Mawson indicate pitch angle distributions that were both extremely anisotropic and asymmetric.

Theoretical shock and stochastic acceleration spectral forms were employed to investigate the acceleration process. The spectra at all phases of the event are best fitted with a stochastic acceleration spectral form. This result suggests that a stochastic process associated with magnetic reconnection was a source of relativistic protons.

DISCUSSION

6.1 INTRODUCTION

The major aim of this study was to gain insight into the acceleration process/es responsible for the production of relativistic protons which led to the 14 July 2000, 15 April 2001 and 20 January 2005 GLEs. To achieve this, analytical and numerical spectral forms representing shock and stochastic acceleration mechanisms were fitted to ground-based measurements of relativistic proton fluxes, covering the energy spectrum up to 10 GeV. This chapter considers the results presented in Chapters 3, 4 and 5 in terms of interplanetary conditions at the time of each GLE, the impact of transport processes on low-energy proton intensities, and the source mechanisms responsible for relativistic particle acceleration.

6.2 STATE OF THE INTERPLANETARY MEDIUM

6.2.1 *14 July 2000*

A period of intense solar activity from 10 to 15 July 2000 produced the Bastille Day GLE from an eruption on 14 July 2000. Several shocks and associated magnetic structures are apparent from *ACE* measurements, indicating that the IMF had experienced sizeable disturbances from 11 to 16 July (Figure 6.1).

Particle pitch angle distributions at Earth during a GLE provide information about the interplanetary medium through which the particles have travelled. Figure 6.2 illustrates the distributions during the rise and peak phases of this GLE. The particle arrival near onset (10:35 UT) was strongly anisotropic, indicating focussed transport conditions and thus implying minimal particle scattering.

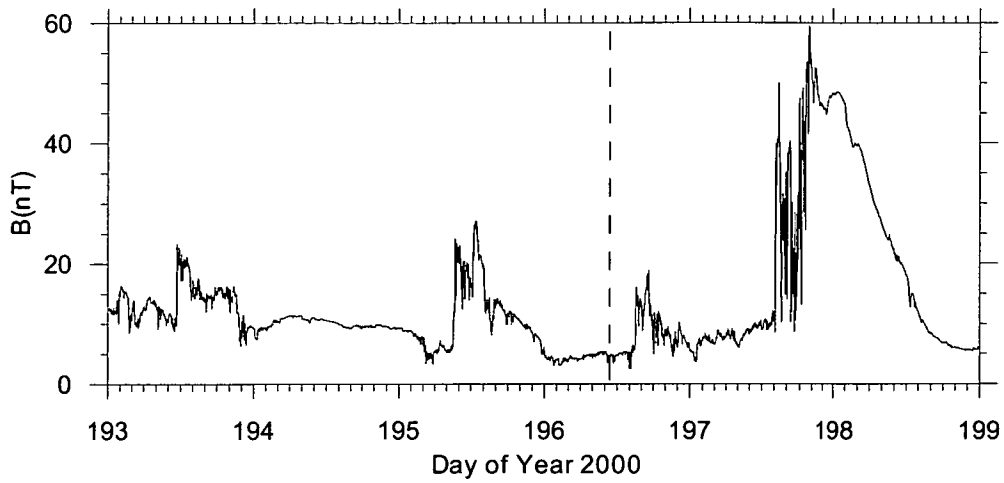

FIGURE 6.1: Magnitude of the magnetic field intensity as measured by *ACE* from 11 to 17 July 2000 (Days 193-199). Dashed line indicates the onset time of GLE 59 (10:32 UT in 1-minute data) at Earth.

However, at 10:40 UT the field-aligned component of the pitch angle distribution (i.e., particles moving in the forward direction) began to broaden and local scattering began to increase. Pitch angle distributions from 10:40 UT also show enhancements above 90°, implying the possibility of particle propagation in the reverse direction (i.e., bi-directional flow). Bi-directional flow can result from: (1) enhanced turbulence in the interplanetary medium or a shock beyond Earth's orbit which results in the back-scattering of particles; or (2) particles arriving from the Sun along two different paths of a closed interplanetary magnetic loop (Ruffolo *et al.*, 2006). This was examined by incorporating a modification of the pitch angle distribution function (see section 2.2.9). Results indicated no evidence for an excess of reverse-propagating particles (i.e., a significant peak in the pitch angle distribution above 90° at the intervals examined).

Bieber *et al.* (2002) proposed that the rapid decrease in anisotropy for this event was strongly influenced by a magnetic disturbance located 0.3 AU beyond the Earth, which reflected ~85% of the relativistic solar protons back toward the Earth. Their hypothesis is supported by *ACE* and *Wind* spacecraft observations of shocks and associated magnetic structures which passed the Earth on 13 July 2000, as well as the rapid increase in the neutron monitor response of stations viewing in the anti-sunward field direction (see Figure 3.3). However, significant increases in neutron monitor responses at 10:40 UT (approximately 10 minutes after GLE onset) were not only observed at stations viewing in the anti-sunward field direction (e.g., Tixie Bay,

12.8%), but also at stations viewing perpendicular to the nominal sunward field direction (Apatity, 30.6%, and Inuvik, 15.3%). Therefore, the underlying isotropic component (Figure 6.2) is associated with local turbulence in the IMF.

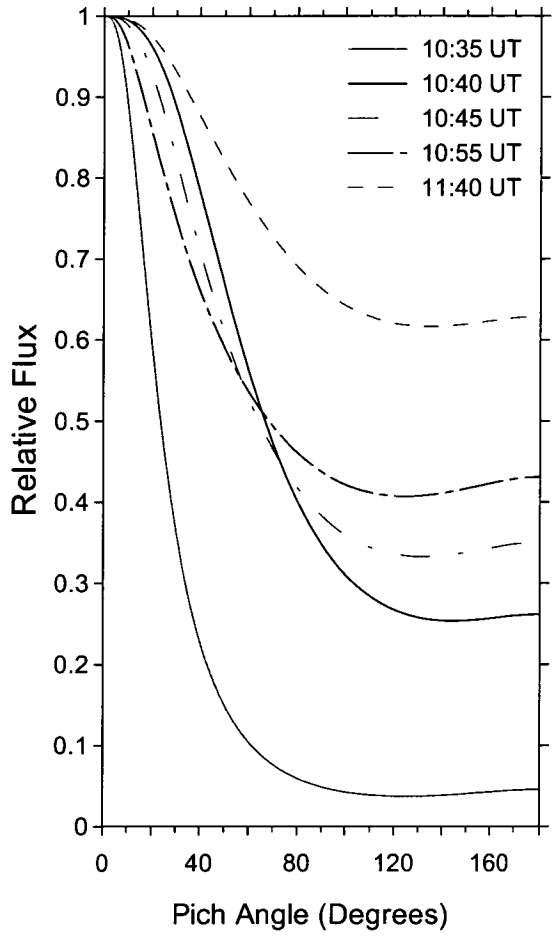

FIGURE 6.2: Derived pitch angle distributions at 10:35, 10:40, 10:55, 11:10 and 11:40 UT during the 14 July 2000 GLE.

Measurements of the IMF intensity several hours after GLE onset provide information on the state of the medium into which the particles were injected. *ACE* detected a moderate magnetic disturbance (15 nT) at 14:55 UT (Smith *et al.*, 2001).

The broadening of the width of the pitch angle distribution in the forward direction, as illustrated in Figure 3.6, suggests that relativistic particles may have encountered this disturbance (i.e., a shock/magnetic cloud structure) en-route to earth.

6.2.2 *15 April 2001*

The 15 April 2001 solar event was the largest of a series of solar eruptions that occurred during a period of intense solar activity extending from 28 March to 21 April. However, *ACE* observations suggest that interplanetary conditions and the medium into which the particles were injected were relatively quiet (Figure 6.3). For example, the average solar wind speed was ~400 km/s and the average magnetic field strength for this period was ~5 nT, which is typical for a quiet-time solar wind. Figure 6.4 shows that the particle arrival near GLE onset (14:00 UT) was anisotropic, indicating focussed transport conditions with minimal particle scattering. The anisotropy decreased relatively slowly from 14:00 to 14:45 UT and then remained unchanged until at least 16:00 UT. Pitch angle distributions from 14:30 UT show enhancements above 90°, implying the possibility of particle propagation in the reverse direction (i.e., bi-directional flow). Again this was examined using the method described in section 2.2.9. The results indicated no evidence for an excess of reverse-propagating particles.

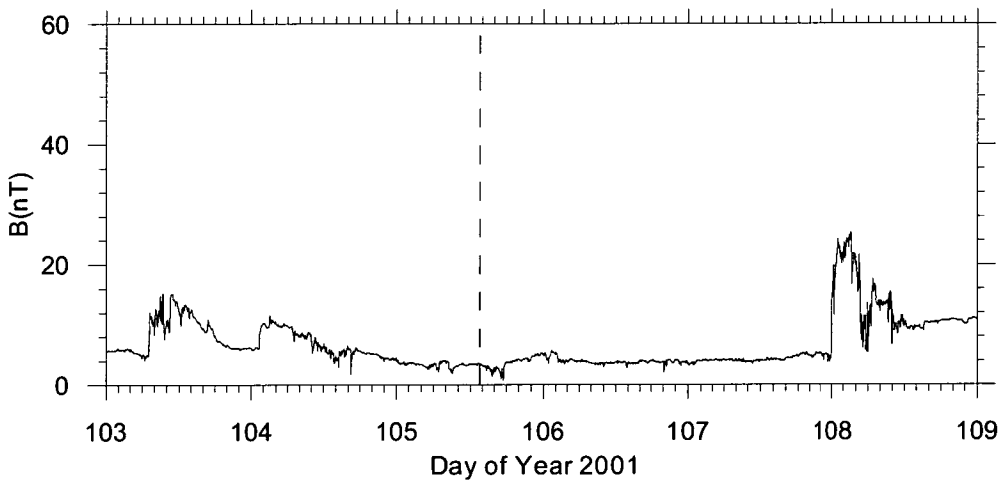

FIGURE 6.3: Magnitude of the magnetic field intensity as measured by *ACE* for the period 13 to 18 April 2001 (Days 103 to 109). Dashed line indicates the onset time of GLE 60 (13:55 UT in 5-minute data) at Earth.

Whilst *ACE* measurements of the IMF strength indicate the passage of shocks and associated magnetic structures for the period 13 to 14 April (Figure 6.3), the low magnetic strength of these disturbances suggest that they were unlikely to produce a significant reflective magnetic barrier beyond Earth. Therefore, the small underlying

isotropic component in pitch angle distributions (Figure 6.4) is probably the result of limited local IMF scattering effects.

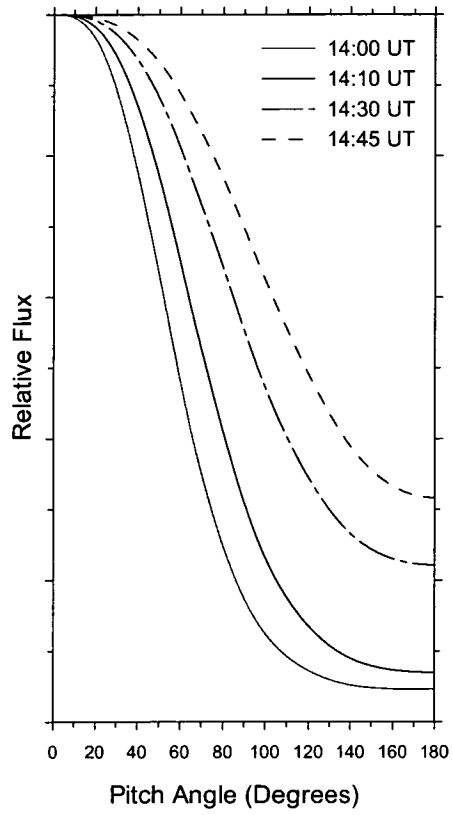

FIGURE 6.4: Derived pitch angle distributions for 14:00 UT (*near onset*), 14:10 UT (*rising phase*), 14:30 UT (*peak*) and 14:45 UT (*declining phase*).

6.2.3 *20 January 2005*

A series of solar eruptions occurred during a period of intense solar activity extending from 14 to 20 January 2005. The largest of these eruptions produced the 20 January 2005 GLE. Figure 6.5 shows that *ACE* measurements of the IMF strength from 16 to 19 January indicate the passage of several strong shocks and associated magnetic structures which may have resulted in a sizable magnetic disturbance beyond the Earth. However, by the time the GLE commenced the IMF had recovered somewhat. The magnitude of the IMF intensity between GLE onset and the arrival of the shock at Earth (~36 hours), gives an indication of the state of the medium into which the particles were injected. The average IMF intensity as measured by *ACE* for this period was ~5 nT (Figure 6.5).

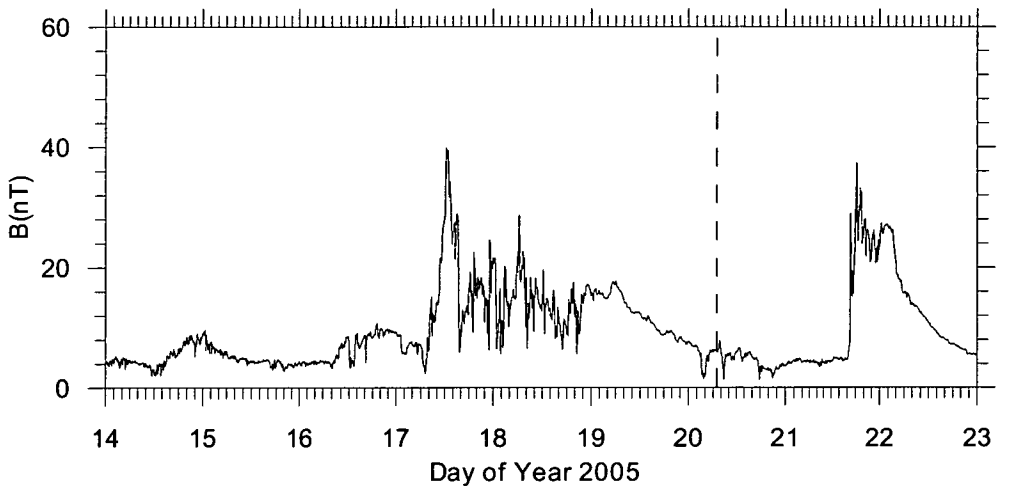

FIGURE 6.5: Magnitude of the magnetic field intensity as measured by *ACE* from 14 to 23 January 2005 (Days 14-23). Dashed line indicates the onset time of GLE 69 (06:48 UT in 1-minute data) at Earth.

Solar wind speed measurements from *Wind* and *ACE* were not available as the intense particle emission saturated their detectors. However, the *CELIAS* proton detector on board the *SOHO* spacecraft was unaffected and its measurements indicated the solar wind speed ranged from 600 to 800 km s^{-1} (hourly averages). This suggests that relativistic particles were injected into a relatively smooth interplanetary medium with a slightly smaller than nominal path length as a result of the higher solar wind speed.

The particle arrival at 06:50 UT (onset) and 06:55 UT (peak) (Figure 6.6) were strongly anisotropic, indicating focussed transport conditions with minimal particle scattering. After ~07:00 UT the field-aligned component of the pitch angle distribution in the forward direction began to broaden and local scattering began to increase. By 07:40 UT there is evidence for significant particle pitch angle scattering above 90°; therefore, the possibility of bi-directional flow was examined.

Modelling shows that by 07:40 UT (Figure 6.6, *right*) there is evidence of an excess of reverse-propagating particles (i.e., a significant enhancement in the pitch angle distribution above 90°). Table 6.1 shows the improved fits to observations when bi-directional flow parameters (section 2.2.9) are included in the modelling. This enhancement could be attributed to a shock or strong turbulence in the disturbed interplanetary medium beyond Earth's orbit resulting from previous solar activity described above, which resulted in the back-scattering of relativistic protons. Alternatively, bi-directional flow could be attributed to particles arriving from the

Sun along two different paths in a closed interplanetary magnetic loop configuration. However, the author is unaware of any evidence in the literature to support the existence of a closed interplanetary magnetic loop configuration for this event. This suggests that back-scattering from a reflecting boundary beyond Earth is a more likely cause for the bi-directional flow.

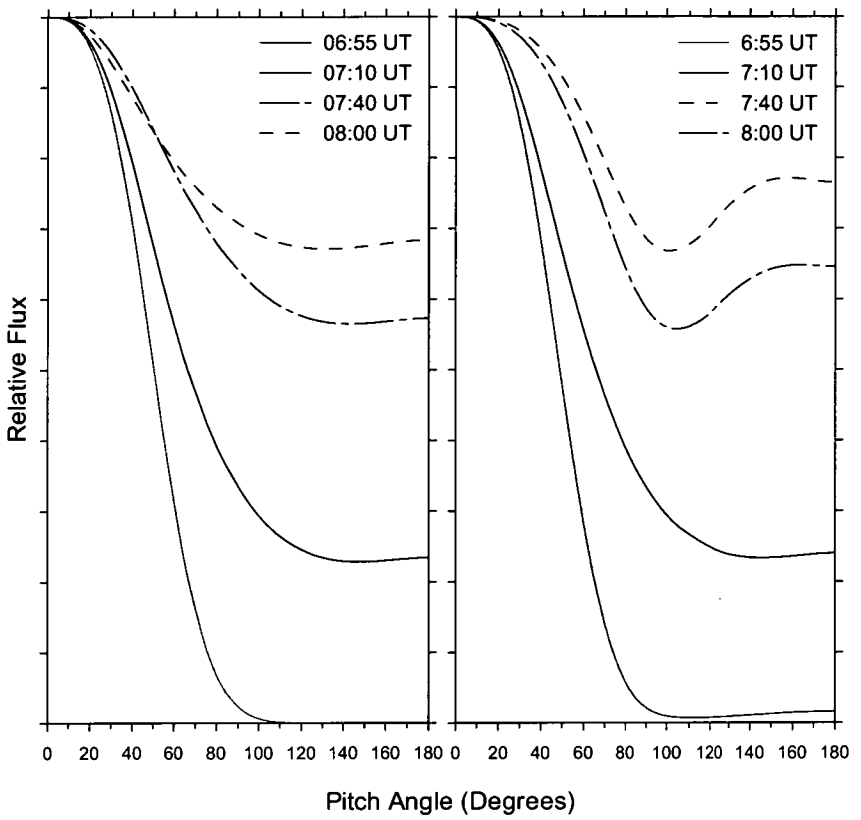

FIGURE 6.6: Derived pitch angle distributions for the 20 January 2005 GLE at 06:55 (*peak*) and 07:10, 07:40, 08:00 UT decline phases (*left*) and for the same intervals incorporating a modification of the pitch angle distribution function to model bi-directional flow (*right*).

TABLE 6.1

PITCH ANGLE DISTRIBUTION
EFFECT OF BI-DIRECTIONAL FLOW

Time [a] (UT)	Standard Pitch Angle (WSS)	Bi-directional Flow (WSS)
07:40....	2500	2440
07:50....	1720	1500
08:00....	1120	910

[a] Time refers to the start of a five-minute interval.

6.3 TRANSPORT PROCESSES AND LOW-ENERGY PROTON INTENSITIES

If the path length through the IMF during a GLE is known, one can calculate the expected proton arrival times at the Earth for any energy. This allows one to determine whether interplanetary transport processes (see Section 1.3) affected the propagation of low-energy protons en-route to Earth, thereby delaying their arrival.

The time Δt required for particles to travel along the IMF is:

$$\Delta t = s / \beta c \tag{6.1}$$

where s is the distance from the Sun along a nominal IMF line to Earth and β is the particle speed in units of the speed of light c.

Following Lockwood *et al.* (1990), the distance depends on the solar wind speed V_{SW} and the angular speed Ω of the Sun and is given by:

$$s = \frac{r\left(1+\alpha^2 r^2\right)^{0.5}}{2} + \frac{\ln\left\{\alpha r + \left(1+\alpha^2 r^2\right)^{0.5}\right\}}{2\alpha} \tag{6.2}$$

with $\alpha = \Omega \cos\Lambda / V_{SW}$, where Λ is the heliographic latitude and r is the heliocentric radial distance. The value of Λ is taken to be the heliographic latitude of the foot point of the nominal Sun-Earth field line. The angular speed of the Sun varies from 2.9×10^{-6} to 2.7×10^{-6} s^{-1} between 0° and 30° heliolatitude.

Equation (6.2) provides a first-order approximation of the path length. Using a zero proton pitch angle (because of the rapid focussing of a particle spiralling in a divergent field) the path length for the 14 July 2000 GLE is estimated at 1.1 AU, based on a mean solar wind speed V_{SW} of ~600 km s^{-1}. For this event no significant flux above 3 GV (2.2 GeV) was detected by neutron monitors at sea level and the injection time at the Sun was calculated using this maximum energy (i.e., β = 0.95). The proton travel time is calculated to be 565 ±40 seconds. To estimate the injection time at the Sun the travel time is simply subtracted from the onset time of the 14 July 2000 GLE (10:32 UT ±30 seconds, 1-minute data), to give 10:23 UT ±50 seconds. This calculation includes a 10% uncertainty in the mean solar wind speed. For the 15 April 2001 GLE, the path length along the IMF is

estimated at 1.2 AU, based on a mean solar wind speed V_{SW} of ~400 km s^{-1}. This result is in agreement with Bieber *et al.* (2004). In contrast, Sáiz *et al.* (2005a), using the "inverse velocity method", calculated a path length of 1.7 AU. However, they did not have confidence in this result and considered the result of Bieber *et al.* (2004) (which uses a detailed interplanetary transport model) to be more accurate. No significant flux above 6.3 GV (5.4 GeV) (i.e., β = 0.99) was detected by neutron monitors at sea level. For a path length of 1.2 AU, the travel time at this energy is calculated to be 590 ±85 seconds. From the neutron monitor onset time of 13:55 UT ±30 seconds, the injection time at the Sun is estimated at 13:45 UT ±90 seconds.

For the 20 January 2005 GLE, the path length along the IMF is estimated at 1.1 AU, based on a mean solar wind speed V_{SW} of ~600 km s^{-1}. No significant flux above 7.6 GV (6.7 GeV) was detected by sea-level neutron monitors. The proton travel time at this energy (i.e., β = 0.99) is calculated to be 540 ±40 seconds. Based on a neutron monitor onset time of 06:48 UT ±30 seconds, the injection time at the Sun is estimated at 06:39 UT ±50 seconds. Bieber *et al.* (2004) and Sáiz *et al.* (2005*a*, 2005*b*) derived relativistic proton injection times for the 15 April 2001 and 20 January 2005 GLEs within 3 minutes of the estimates calculated here.

6.3.1 *Comparisons with GOES observations*

Spacecraft data have been corrected for arrival-time velocity dispersion by simply shifting the GOES proton time-lines backwards by the difference in transit time estimates. Figure 6.7 shows that for all three GLE events the particle intensities at spacecraft energies (from ~30 to ~100 MeV) are considerably lower than predicted from fitted spectra. Using the 15 April 2001 GLE as an example, a 30-MeV particle injected into a smooth interplanetary medium at approximately 13:45 UT would require a travel time of approximately 41 minutes, arriving at 1 AU at ~14:26 UT. Figure 6.7*b* shows that at 14:45 UT, 30-MeV proton intensities remain significantly lower than expected values.

After correction for dispersion, further delays in the arrival time or suppression of release of low-energy protons also apply to the 14 July 2000 and 20 January 2005 GLEs. This suggests that for each of these events, the propagation of low-energy

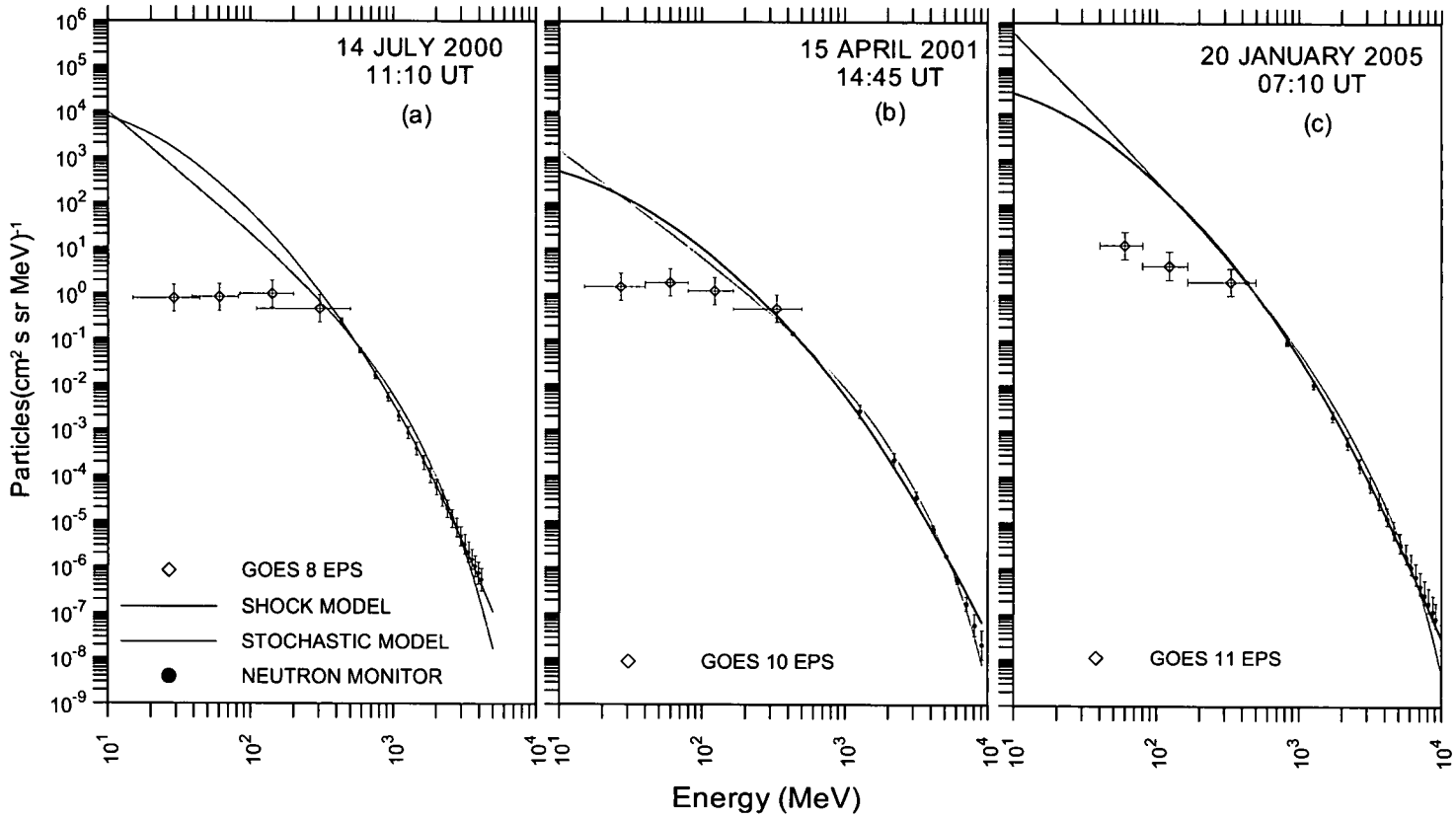

FIGURE 6.7: Energy spectral fits to flux values generated from ground-based neutron monitor observations during the decline phases of the three events: *(a)* 14 July 2000 GLE, 11:10 UT, *(b)* 15 April 2001 GLE, 14:45 UT and *(c)* 20 January 2005 GLE, 07:10 UT. Five-minute proton data (*open triangles*) from *GOES 8, 10* and *11* energetic particle sensors (EPS) are shown for comparison and have been corrected for arrival time velocity dispersion; energy range is ~30 to ~330 MeV. Neutron monitor derived data for *(small black circles)* for: *(a)* ~400 MeV to 5 GeV; *(b)* and *(c)* ~ 400 MeV to 10 GeV. Fitted curves are of the Ellison & Ramaty (1985) shock acceleration (*light grey line*) and the Gallegos-Cruz & Perez-Peraza (1995) stochastic acceleration (NCS injection, equation (2.28)) spectral forms (*black line*).

protons en-route to Earth was probably affected by processes which resulted in the trapping of particles at the source and/or other interplanetary transport effects, as outlined in section 1.3. By excluding spacecraft data, the impact of such effects on spectral analyses is minimised (Bombardieri *et al.*, 2008, ApJ, submitted).

6.4 SOURCE MECHANISMS

6.4.1 *14 July 2000 GLE*

Bombardieri *et al.* (2006) showed that during the rising phase of the 14 July 2000 GLE, the form of the spectrum varied considerably suggesting a change in the source of relativistic particles (Figure 6.8). Best-fit spectra at 10:45 UT suggest protons were accelerated to relativistic energies at the bow shock of the 14 July 2000 CME. This is supported by the detection of Type II decametric to kilometric radio emissions as the shock propagated through the corona (Reiner *et al.*, 2001).

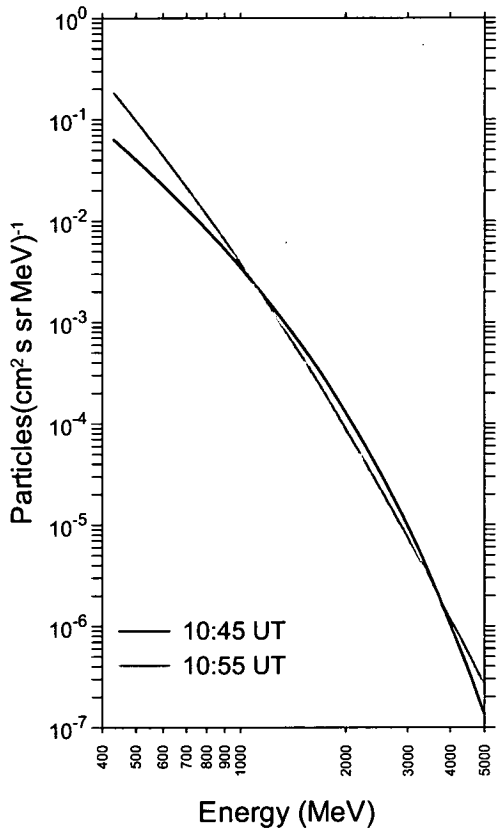

FIGURE 6.8: Best fit particle acceleration spectra (ranging from ~400 MeV to 5 GeV) for the 14 July 2000 GLE. Fitted curve for 10:45 UT (*black line*) is the Ellison & Ramaty (1985) shock acceleration model (*black line*). Fitted curve at 10:55 UT (*peak*) is the Gallegos-Cruz & Perez-Peraza (1995) stochastic acceleration model, equation (2.28) (*grey line*).

Estimates place the initial speed of the CME at between ~1800 km s^{-1} and 2800 km s^{-1} (Reiner *et al.,* 2001). The maximum energy produced by the shock, as characterised by the *e*-folding energy (Ellison & Ramaty 1985), is ~2 GeV. This is very close to the maximum energy observed by sea-level neutron monitors. However, the neutron monitor spectrum at the peak of the GLE is best fitted by a stochastic acceleration spectral form. This implies that resonant wave-particle interaction resulting from magnetic reconnection was an additional source of relativistic protons. Reconfiguration of the coronal magnetic field in the wake of the CME involved magnetic reconnection, where dissipating current sheets formed high-velocity plasma outflow jets. Such jets could be the source of the MHD turbulence which initiated stochastic acceleration (Innes 1997; Miller *et al.,* 1997; Priest & Forbes 2002). With the advent of the *RHESSI* spacecraft there is now strong observational evidence supporting the importance of current sheets in major solar eruptive episodes (e.g., Ciaravella *et al.* (2002); Ko *et al.* (2003); Sui & Holman (2003); Webb *et al.* (2003); Gary & Moore (2004); Sui, Holman & Dennis, (2004), Lin *et al.* (2005)).

Bombardieri *et al.* (2006) found that MHD turbulence was important in relativistic particle acceleration for the 14 July 2000 GLE. Further investigation by Bombardieri *et al.* (2007) using a more realistic stochastic acceleration model support these initial findings.

Klein *et al.* (2001) provided additional evidence to support relativistic proton acceleration by dissipating neutral current sheets in the wake of the CME. Using radio, X-ray, EUV and visible light observations, they were able to trace the non-radial propagation path of a filament to the north-western solar quadrant. Klein *et al.* (2001) proposed that this filament interacted with coronal structures (large-scale coronal loops) near to Sun–Earth connecting magnetic field lines (i.e., near 60° western heliolongitude). This interaction involved reconfiguration of the coronal magnetic field in the wake of the erupting filament (CME). They based this finding on radio observations of a prominent bright continuum radio source, accompanied by a group of intense Type III radio bursts from microwave to hectometric wavelengths, which coincided with a rise in neutron monitor count rates. Klein *et al.* (2001) proposed that the reconfiguration of the coronal magnetic field led to relativistic proton production and that the major driver of these changes was the ejected magnetic field configuration around the erupting filament which was part of

the CME. In part, the work of Klein *et al.* (2001) is supported by results presented here, which suggests that the bow-shock of the 14 July 2000 CME was not the only source of relativistic particles for this event and that MHD turbulence from magnetic reconnection, created by reconfiguration of the coronal magnetic field in the wake of the CME, was also a potential source.

6.4.2 *15 April 2001 GLE*

The high to moderate degrees of anisotropy during the early stages of the 15 April 2001 GLE and the relatively stable interplanetary conditions affords the opportunity to investigate the acceleration process more effectively, particularly during the early stages of the event. Bombardieri *et al.* (2007) showed that the spectra up to 10 GeV at the rise (14:10 UT), peak (14:30 UT) and decline (14:45 UT) phases of GLE 60 were best fitted by a shock acceleration spectral form.

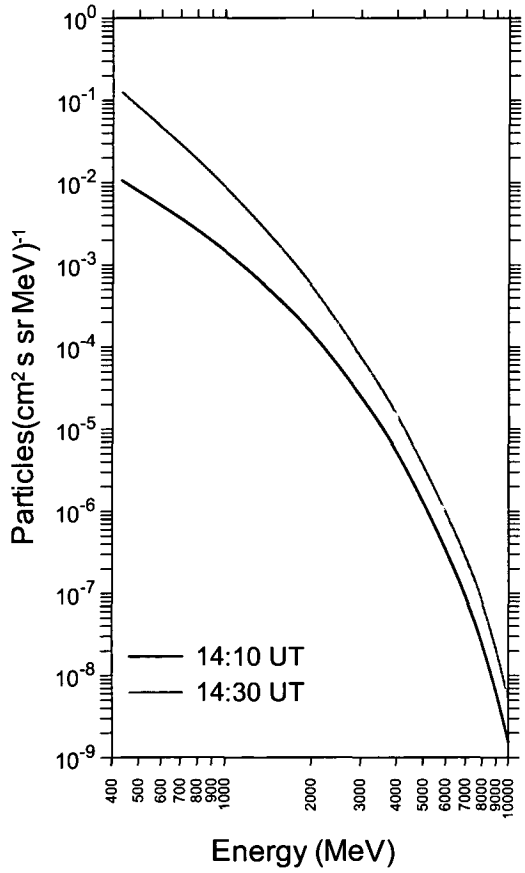

FIGURE 6.9: Best-fit particle acceleration spectra (ranging from ~400 MeV to 10 GeV) for the 15 April 2001 GLE. Fitted curve for 14:10 UT (*rising phase*) and 14:30 UT (*peak*) is the Ellison & Ramaty (1985) shock acceleration model.

The most likely acceleration source was the bow shock of the 15 April 2001 CME. This result is supported by the detection of Type II decametric to kilometric

radio emissions as the shock propagated through the corona and is in agreement with investigations by Tylka *et al.* (2002), Gopalswamy *et al.* (2003) and Bieber *et al.* (2004). Estimates place the initial speed of the CME at ~1200 km/s (Tylka *et al.*, 2002), greater than the ~750 km/s required to produce SEPs (Reames 1999). The *e*-folding energy at 14:30 UT (*peak*) is ~4.1 GeV, which is near to the maximum energy (~5 GeV) observed by sea-level neutron monitors for this GLE. Bombardieri *et al.* (2007) report no significant change in the spectrum (Figure 6.9) at the time intervals modelled, suggesting that the 15 April CME-driven shock was dominant in relativistic particle acceleration. This is in contrast to the 14 July 2000 GLE where the spectrum varied significantly during the rise phase of the event (Figure 6.8).

6.4.3 *20 January 2005 GLE*

The location of the intense emissions (N14° W61°) for the 20 January 2005 solar eruption must have been close to the nominal Sun-Earth connecting magnetic field line. The extremely rapid rise (~5 minutes to peak intensity) in neutron monitor count rates is evidence for excellent connectivity. The strong anisotropy near GLE onset indicates that relativistic particles travelled along the IMF essentially scatter-free. Bieber *et al.* (2005) noted that over a 6-minute interval the neutron monitor count rate (in 1-minute data) at South Pole, McMurdo and Terre Adélie increased by factors of 56, 30 and 46 respectively. For the same interval other stations observed increases of only a factor of 3. This suggests that relativistic protons arriving at 1 AU were initially confined to a narrow beam. These characteristics provide a rare opportunity to directly observe the acceleration source from Earth during the initial phase of the event.

Of the models employed, results show that the proton spectra from the peak (06:55 UT) to the decline (07:30 UT) phases of the event are best fitted by the stochastic acceleration model (Bombardieri *et al.*, 2008, ApJ, *in press*). Furthermore, the overall form of the spectrum is similar for all the intervals modelled. This suggests that resonant wave-particle interaction resulting from magnetic reconnection was a potential source of relativistic protons. Mechanisms for relativistic particle production involving magnetic reconnection include solar flares and coronal neutral current sheet reconnection behind an erupting CME (e.g., Lin & Forbes (2000); Klein *et al.* (2001); and Lin *et al.* (2005)).

The 20 January 2005 solar eruption was associated with a very fast CME with an estimated speed of 2500 km s^{-1} (Simnett 2006). The role played by this CME in relativistic proton acceleration is unclear. Chenglong Shen *et al.* (2007) found that CME speed alone does not reflect the real strength of a CME-driven shock. They showed that the 15 September 2001 CME, with a speed of 750 km s^{-1}, produced a larger SEP event (i.e., drove a stronger shock) than the 15 June 2000 CME with a speed of ~1400 km s^{-1}. Chenglong Shen *et al.* (2007) argue that the plasma density upstream of a shock, as well as the magnetic field strength, are important factors when considering shock strength. Therefore, the fact that the 20 January 2005 CME was fast does not necessarily mean it was capable of driving a shock strong enough to accelerate particles to energies > 10 GeV. However, one must be cautious not to rule out entirely the role of the 20 January 2005 CME in relativistic particle acceleration for this event.

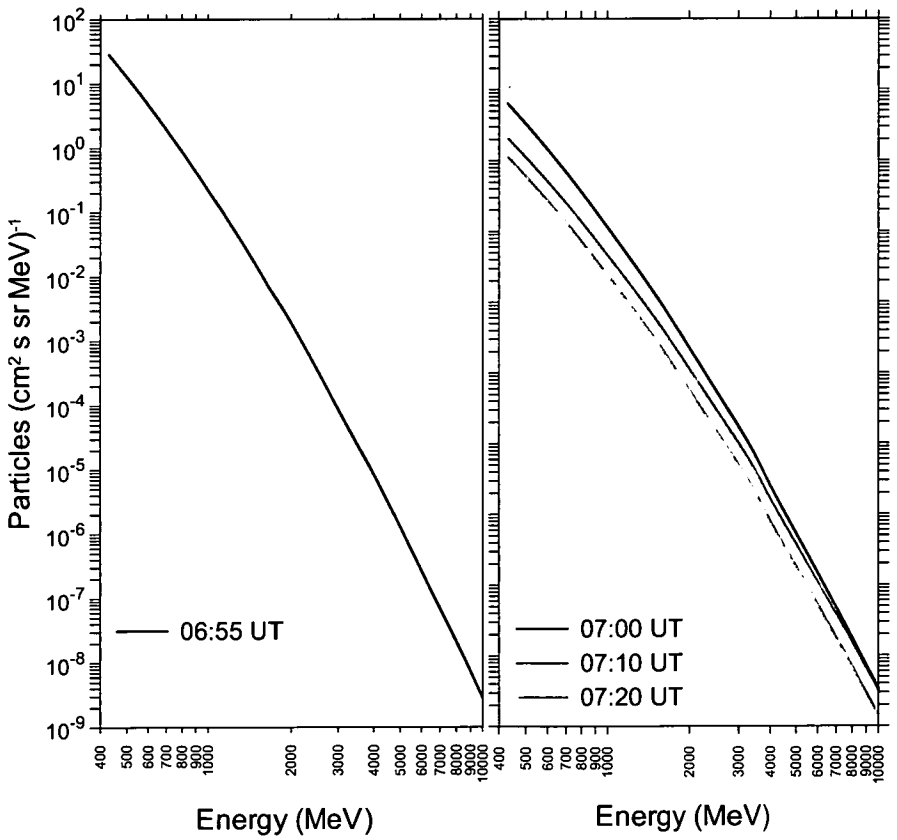

FIGURE 7.10: Best fit particle acceleration spectra (ranging from ~400 MeV to 10 GeV) for the 20 January 2005 GLE. Fitted curves for the peak (06:55 UT) (*left*) and decline phases (07:00, 07:10 and 07:20 UT) (*right*) of the event, are from the Gallegos-Cruz & Perez-Peraza (1995) stochastic acceleration model, equation (2.28).

The values of *e*-folding energy derived from the shock acceleration model (Table 5.4) are larger than those found for the 14 July 2000 and 15 April 2001 GLEs. This suggests that spectra with rapid roll-off below 10 GeV cannot fit the spectrum derived from neutron monitor observations. Therefore, for the time intervals modelled, the stochastic acceleration spectral form gives a better representation of the neutron monitor response.

6.5 *Summary*

This chapter has examined the results presented in Chapters 3, 4 and 5 with particular focus on the state of the IMF at the time of each GLE and possible source mechanisms for relativistic proton acceleration. Each GLE was marked by a strong anisotropic onset, implying that initially particle propagation was essentially scatter-free. However, for the 14 July 2000 and 15 April 2001 GLEs there is evidence for significant scattering several minutes after their respective onsets. In the case of the 14 July 2000 GLE, the broadening of the pitch angle distributions in the forward direction and the isotropic component (at pitch angles greater than 90°) is probably due to scattering effects associated with the IMF and relativistic particles encountering a shock en-route to earth. For the 20 January 2005 GLE, part of the underlying isotropic component in pitch angle distributions is attributed to bi-directional flow. Back-scattering from a reflecting boundary beyond Earth is a likely cause. For the 15 April 2001 GLE, the comparatively smaller isotropic component in the pitch angle distributions is probably the result of limited local scattering associated with the IMF. Low-energy proton intensities for each GLE are considerably lower than predicted from fitted spectra. This implies that trapping at the source and/or transport processes affected the propagation of low-energy protons en-route to Earth. For the 14 July 2000 GLE sources of relativistic particle acceleration include: 1) a coronal shock driven by the 14 July 2000 CME and 2) MHD turbulence resulting from coronal current sheet magnetic reconnection created by reconfiguration of the magnetic fields in the wake of a CME. In the case of the 15 April 2001 GLE protons were accelerated to relativistic energies by a coronal shock driven by the 15 April 2001 CME. For the 20 January 2005 GLE a stochastic process cannot be ruled out as a mechanism for accelerating protons to relativistic energies. Possible sources include the 20 January 2005 solar flare or sites of magnetic reconnection formed in the wake of the 20 January 2005 CME.

CONCLUSION

The ground level response of the relativistic protons which gave rise to the 14 July 2000, 15 April 2001 and 20 January 2005 GLEs have been analysed to better understand the role of flares and CMEs in relativistic proton acceleration.

The global analysis technique described in Chapter 2 was used to derive the spectrum, the axis of symmetry of the particle arrival and anisotropy of relativistic solar protons that give rise to the increased neutron monitor response. The modelling procedure employs a least-squares method to efficiently analyse parameter space for optimum solutions. The modified power law spectral form, used in the analyses presented in Chapters 3-5, was generally found to produce the best fit between observed and calculated neutron monitor responses. An exponential function was used for pitch angle distributions and a modification of this function was used to model bi-directional flow. The geomagnetic field model of Tsyganenko (1989), with International Geomagnetic Reference Field (IGRF) 2005 parameters and adjustments for geomagnetic disturbance as measured by Kp, was employed to determine the asymptotic viewing directions of ground-based instruments. This model was upgraded to include the Dst (disturbance storm time) index, allowing for a more accurate determination of viewing directions for appropriate levels of geomagnetic disturbance (Boberg et al., 1995).

To investigate the mechanisms responsible for relativistic proton acceleration, analytical and numerical spectra representing shock and stochastic acceleration processes were fitted to neutron monitor observations of high-energy protons. The Ellison & Ramaty (1985) analytical expression was used for shock acceleration. This widely-used model describes the ability of a particle to gain energy by scattering multiple times between magnetic field irregularities, both upstream and

downstream of a coronal shock. The Gallegos-Cruz & Perez-Pereza (1995) numerical expression was used for stochastic acceleration, whereby energy from turbulence resulting from magnetic reconnection is transferred to particles through the process of wave-particle resonant interactions. The analytical spectra deduced from the neutron monitors were used to generate the input to a generalized non-linear least squares program with synthetic data points weighted by errors in the flux data. Analysis was restricted to protons of energy ≥450 MeV to avoid complications from interplanetary processes which can depress the intensity of low-energy protons at Earth.

For the 14 July 2000 GLE, the particle arrival at 1 AU was strongly anisotropic. This suggests that relativistic particles were affected by limited scattering en-route to Earth. However, several minutes after onset, the field-aligned component of the pitch angle distribution began to broaden and local scattering began to increase. The broadening of the distribution in the forward direction and the overall isotropic component is due to scattering effects associated with the local IMF and relativistic particles encountering a shock en-route to earth. This is consistent with spacecraft observations suggesting that the medium through which the particles propagated was relatively disturbed. The spectrum at 10:45 UT (rise phase) is best fitted with a shock acceleration spectral form. In contrast the spectra at the peak (10:55 UT) and declining phases (11:10 and 11:40 UT) are best fitted by a stochastic acceleration spectral form. This change in spectral form implies more than one source of relativistic protons. Sources include: 1) a coronal shock driven by the 14 July 2000 CME and 2) MHD turbulence resulting from coronal current sheet magnetic reconnection created by reconfiguration of the magnetic fields in the wake of a CME.

The particle arrival at onset for the 15 April 2001 GLE was again strongly anisotropic, suggesting that relativistic particles were affected by limited scattering en-route to earth. Whilst the field-aligned component of the pitch angle distribution did broaden, the overall isotropic component was notably smaller compared to that modelled for the 14 July 2000 and 20 January 2005 GLEs. This result is probably due to limited local scattering associated with the IMF and is consistent with spacecraft observations suggesting that the medium through which the particle propagated was relatively undisturbed. Neutron monitor observations up to 10 GeV at the rise (14:10 UT), peak (14:30 UT) and decline (14:45 UT) phases of the event are best fitted by a shock acceleration spectral form. The form of these spectra did

not vary considerably, suggesting that the acceleration mechanism did not change. This implies that a coronal shock was the most likely mechanism for producing relativistic protons at 1 AU and the most likely source for this shock was the 15 April 2001 CME.

The 20 January 2005 solar eruption produced the highest intensity of relativistic solar particles since the famous event on 23 February 1956. For the 2005 GLE the rise to maximum was extremely rapid (~5 minutes). The event was marked by a highly anisotropic onset followed by a fairly rapid decrease in anisotropy. Part of the underlying isotropic component in pitch angle distributions is attributed to bi-directional flow. Back-scattering from a reflecting boundary beyond Earth is a likely cause. *ACE* measurements of the IMF indicate that relativistic particles were injected into a relatively smooth medium. However, measurements of the IMF prior to the GLE indicate the passage of shocks and associated magnetic structures which could have contributed to enhanced turbulence beyond the Earth. From 06:55 UT (peak phase) to 07:30 UT (decline phases), the spectrum derived from neutron monitor observations is best fitted by a stochastic acceleration spectral form. This result suggests that a stochastic process cannot be ruled out as a mechanism for accelerating protons to relativistic energies. Possible sources include the 20 January 2005 solar flare and coronal neutral current sheet reconnection in the wake of the associated CME.

Future investigations should compare the Lee (2005) and Giacalone (2005) models of diffusive shock acceleration with the widely-used Ellison and Ramaty (1985) model. These recent studies show that, for a range of shock normal angles, the high-energy part of the spectrum will be dominated by particles produced when a shock is quasi-perpendicular. Importantly, these authors argue that the rollover at higher energies is not an exponential as assumed by the Ellison and Ramaty shock model, particularly in the case of quasi-perpendicular shocks. Therefore, for events where modified power law spectra show very little roll-over (e.g., the 20 January 2005 GLE) it is possible that such shock models could potentially provide better fits to neutron monitor observations than that achieved by the E&R model. Incorporation of these new models and those used in this study into the global analysis technique would enable a direct fit to neutron monitor observations, instead of the two-stage approach that was employed in this study. Furthermore, the

inclusion of the most recent Tsyganenko magnetospheric model will further improve the accuracy of trajectory calculations.

In conclusion, the major finding of this study indicates that, along with CME–driven shocks, sites of magnetic reconnection in the solar corona are a potential source of relativistic protons that give rise to GLEs.

REFERENCES

Ahluwalia, H.S., & McCracken, K. G. 1965, Proc. 9th Int. Cosmic-Ray Conf. (London), **1**, 568

Akasofu, S.-I. 2001, in Space Weather, Geophysical Monograph 125, Predicting Geomagnetic Storms as a Space Weather Project, ed. P. Song et al. (Washington: AGU), 329

Axford, W. I., Lear, E., & Skadron, G. 1977, Proc. 15th Int. Cosmic-Ray Conf. (Plodiv), **11**, 132

Badhwar, G. D., & O'Neill, P. M. 1996, Adv. Space Res., **17**, 7

Beeck, J., & Wibberenz, G. 1986, Astrophys. J., 311, **437**

Belov, A. V., et al. 2001, Proc. 27th Int. Cosmic-Ray Conf. (Hamburg), **8**, 3446

Bemporad, A. et al. 2006, Astrophys. J., **638**, 1110

Bieber, J. W. & Evenson, P. 1991, Proc. 22nd Int. Cosmic-Ray Conf. (Dublin), **3**, 129

Bieber, J. W., et al. 2002, Astrophys. J., **567**, 622

Bieber, J. W., et al. 2004, Astrophys. J., **601**, L103

Bieber, J. W., et al. 2005, Proc. 29th Int. Cosmic-Ray Conf. (Pune), **1**, 237

Bierman, L. 1957, Observatory, **77**, 109

Blandford, R. D., and Ostriker, J. P. 1978, Astrophys. J., **221**, L29

Boberg, P. R., et al. 1995, Geophys. Res. Lett., **22**, 1133

Bombardieri, D. J., et al. 2006, Astrophys. J., **644**, 565

Bombardieri, D. J., et al. 2007, Astrophys. J., **655**, 813

Bombardieri, D. J., et al. 2008, Astrophys. J., **682**, in press

Bostanjyan, N. Kh., et al. 2007, Adv. Space Res., **39**, 1454

Bougeret, J.-L., et al. 1995, Space Sci. Rev, **71**, 231

Bütikofer, R., et al. 2006, in Proc. 20th European Cosmic-Ray Conf. (Lisbon: Inst. Superio Technico), http://www.lip.pt/events/2006/ecrs/posters

Cane, H. V., et al. 2006, J. Geophys. Res., **111**, A06S90

Carmichael, H. 1968, in Annals of the IQSY, Volume 1- Geophysical Measurements : Techniques, Observational Schedules and Treatments of Data, ed, C. M. Minnis (United States: MIT Press)

Chenglong Shen, et al. 2007, Astrophys. J., **670**, 849

Ciaravella, A., et al. 2002, Astrophys. J., **575**, 1116

Cooke, D. J., et al. 1991, Il Nuovo Cimento C, **14**, 213

Cramp, J. L. 1996, PhD Thesis, University of Tasmania

Cramp, J. L., Duldig, M. L., & Humble, J. E. 1997, J. Geophys. Res., **102**, 4919

Cramp, J. L., et al. 1997, J. Geophys. Res., **102**, 24237

D'Andrea, C., & Poirier, J. 2005, Geophys. Res. Lett., **32**, L14102, doi: 10.1029/2005GL023336

Debrunner, H., Flückiger, E. O., & Lockwood, J. A. Presented at the 8th European Cosmic Ray Conference, Rome, 1982

Debrunner, H., *et al.* 1997, Astrophys. J., **479**, 997

Dryer, M., et al. 2001, Space Sci., **204**, 267

Duldig, M. L. 1994, Proc. Astron. Soc. Aust., **11**, 110

Ellison, D. C., & Ramaty, R. 1985, Astrophys. J., **298**, 400

Ellison, D. C., & Double, G. P. 2002, Astroparticle Phys, **18**, 213

Falcone, A., et al. 2003, Astrophys. J., **588**, 557

Firor, J. 1954, Phys. Rev., **94**, 1017

Flückiger, E., & Köbel, E. 1990, J. Geomag. Geoelect., **42**, 1123

Gall, R., J. Jiménez, J., & Camacho, L. 1968, J. Geophys. Res., **73**, 1593

Gall, R., J. Jiménez, J., & Orozco, A. 1969, J. Geophys. Res., **74**, 3529

Gall, R., J. Smart, D. F., & Shea, M. A. 1971, Planetary Space Sci., **19**, 1419

Gallegos-Cruz, A., & Perez-Pereza, J. 1995, Astrophys. J., **446**, 400

Galsgaard, K., et al. 2005, Astrophys. J., **618**, L153

Gary, A. J., & Moore, R. L. 2004, Astrophys. J., **611**, 545

Giacalone, J. 2005, Astrophys. J., **298**, 400

Gopalswamy, N.et al. 2003 Adv. Space Res., **32**, 2613

Hatton, C.J. 1971, in Progress in Elementary Particle and Cosmic Ray Physics, The Neutron Monitor, ed. J. G, Wilson & S. A. Wouthuysen (Amsterdam: North Holland Publishing Co.), **20**, 1

Humble, J. E., et al. 1991, Geophys. Res. Lett., **18**, 737

Innes, D. E., et al. 1997, Nature, **386**, 811

Jones, F. C., & Ellison, D. C. 1991, Space, Sci. Rev., **58**, 256

Kahler, S. W. 1994, Astrophys. J., **428**, 837

Klein, K.L., et al. 2001, A&A, **373**, 1073

Ko, Y.-K., et al.. 2003, Astrophys. J., **594**, 1068

Kobel, E. 1989, Masters Thesis, Physikalisches Institut, Universität, Bern

Kodama, K.P. 1992, EOS Transactions, **73**, 182

Kudela, K., & Usoskin, I.G. 2004, Czech. J. Phys, **54**, 239

Kuznetsov, S.N., et al. 2005, Proc. 29th Int. Cosmic-Ray Conf. (Pune), **1**, 49

Lee, M.A. 2005, Astrophys. J. Supplementary, **158**, 38

Lin, J., & Forbes, T. G. 2000, J. Geophys. Res., **105**, 2375

Lin, J., Soon, W., & Baliunas, S. L. 2003, New A. Rev., **47**, 53

Lin, J., et al. 2005, Astrophys. J., **622**, 1251

Lockwood, J. A., et al. 1990, Astrophys. J., **355**, 287

Lockwood, J. A., et al. 2002, Sol. Phys., **208**, 113

Lovell, J. L., Duldig, M. L., & Humble, J. E. 1998, J. Geophys. Res., **103**, 23733

Mazur, J. E., et al. 1992, Astrophys. J., **401**, 398

McCracken, K. G., Rao, U. R., Shea, M. A. 1962, Technical Report, 77, (NYO-2670), (Cambridge: MIT)

McCracken, K. G. 1962a, J. Geophys. Res., **67**, 423

McCracken, K. G. 1962b, J. Geophys. Res., **67**, 447

McDonald, F. B. 2000, Space Sci. Rev., **93**, 263

McDonald, J. R. 1974, Nuclear Instr. & Math., **121**, 203

Mewaldt, R. A., et al. 2005, J. Geophys. Res., **110**, 09S18

Miller, J. A. 1991, Astrophys. J., **376**, 342

Miller, J. A., Guessoum, N., & Ramaty, R. 1990, Astrophys. J., **361**, 701

Miller, J. A., et al. 1997, J. Geophys. Res., **102**, 14631

Miyasaka, H., et al. 2005, Proc. 29th Int. Cosmic-Ray Conf. (Pune), **1**, 241

Mooral, H., Belov, A., & Clem, J. M. 2000, Space Sci. Rev., **93**, 285

Murphy, R. J., & Ramaty, R. 1984, Adv. Space Res., **4**, 127

Ness, N. F., Scearce, C. S., & Seek, J. B. 1964, J. Geophys. Res., **69**, 3531

Paker, E. N. 1958, Astrophys. J., **128**, 664

Paker, E. N. 1961, Astrophys. J., **133**, 1014

Perez-Pereza, J., & Gallegos-Cruz, A. 1994, Astrophys. J. Supplementary, **90**, 669

Perez-Peraza, J., et al. 2006, Adv. Space Res., **38**, 418

Plainaki, C., et al. 2007, J. Geophys. Res., **112**, A04102, doi:10.1029/2006 JA011926

Powell, D. R., & Macdonald, J.R. 1972, Computer J., **15**, 148

Priest, E. R., & Forbes, T. G. 2000, in Magnetic Reconnection: MHD Theory and Applications, (Cambridge, UK: Cambridge University Press)

Priest, E. R., & Forbes, T. G. 2002, Astron. Astrophys. Rev., **10**, 313

Rao, U. R., McCracken, K. G., & Venkatesan D. 1963, J. Geophys. Res., **68**, 345

Ramaty, R. 1979, in Particle Acceleration Mechanisms in Astrophysics, ed J. Arons C. Max, & C. McKee, (New York: AIP), 135

Reames, D, V. 1999, Space Sci. Rev., **90**, 413

Reiner, M. J., et al. 2001, Space Science Rev., **204**, 121

Ruffolo, D., et al. 2006, Astrophys. J., **639**, 1186

Sáiz, A., et al. 2005a, Astrophys. J., **626**, 1131

Sáiz, A., et al. 2005b, Proc. 29th Int. Cosmic-Ray Conf. (Pune), **1**, 229

Share, G.H., et al. 2001, Sol. Phys., **204**, 43

Simnett, G. M. 2006, A&A, **445**, 715

Shea, M. A., & Smart, D. F. 1982, Space Sci. Rev., **32**, 251

Smart, D. F., Shea, M. A., & Flückiger, E. 2000, Space Sci. Rev., **93**, 305

Smart, D. F., Shea, M. A. 1990, Proc. 21st Int. Cosmic-Ray Conf. (Adelaide), **5**, 257

Smart, D. F., Shea, M. A., & Gall, R., 1969, J. Geophys. Res., **74**, 4731

Smith, C. W. et al. 2001, Sol. Phys., **204**, 229

Stoer, J., & Bulirsch, R. 1980, in Introduction to Numerical Analysis (New York: Springer-Verlag), 7

Sui, L., & Holman, G. D. 2003, Astrophys. J., **596**, L251

Sui, L., Holman, G.D., & Dennis, B.R. 2004, Astrophys. J., **612**, 546

Sun, W., et al. 2002, Ann. Geophys., **20**, 937

Swinson, D. B., & Shea, M. A., 1990, Geophys. Re. Lett., **17**, 1073

Tsyganenko, N. A. 1989, Planet. Sp. Sci., **37**, 5

Tsyganenko, N. A. 1990, Space. Sci. Rev., **54**, 75

Tylka, A. J., & Lee, M. A. 2006, Astrophys. J., **646**, 1319

Tylka, A. J., et al. 2000, in AIP Conf. Proc. 528, Acceleration and Transport of Energetic Particles in the heliosphere, ed. R. A. Mewaldt et al. (Melville: AIP), 147

Tylka, A. J., et al. 2001, Astrophys. J., **558**, L59

Tylka, A. et al. 2002, Astrophys. J., **581**, L123

Tylka, A. J., et al. 2005, Astrophys. J., **625**, 474

Vashenyuk, E. V., Balabin, Y. V., & Gvozdevsky, B. B. 2003, Proc. 28th Int. Cosmic-Ray Conf. (Tsukuba), **6**, 3401

Webb, D. F., et al. 2003, J. Geophys. Res., **108**, 1440

Wilcox, J. M., Hoeksema, J. T. & Scherrer, P. H. 1980, Science, **209**, 603

Wilson, B. G., Mathews, T. & Johnson, R. H. 1967, Phys. Rev. Lett., **18**, 675

APPENDIX A

RESULTS: 14 JULY 2000

TABLE A1

COMPARISON OF OBSERVED AND CALCULATED INCREASES FOR THE 14 JULY 2000 GLE

Station	Lat.	Lon.	P_c [b]	Alt.	10:30 UT		12:00 UT	
	(deg.)	(deg.)	(GV)	(m)	Observed [c]	Calculated [d]	Observed [c]	Calculated [d]
Apatity	67.55	33.33	0.61	177	5.8	4.7	18.4	18.5
Aragats	40.50	44.17	7.60	3200	0.0	0.2	0.0	0.0
Climax	39.37	253.82	3.03	3400	1.6	0.9	1.5	0.6
Goose Bay	53.27	299.60	0.52	46	1.7	1.6	21.8	23.9
Haleakala	20.27	203.73	13.3	3033	0.0	0.1	0.0	0.0
Hermanus	-34.42	19.22	4.90	26	1.1	0.7	0.0	0.0
Hobart	-42.90	147.33	1.88	18	1.3	0.6	7.7	8.0
Inuvik	68.35	226.28	0.18	21	0.8	0.6	20.7	16.1
Jungfraujoch	46.55	7.98	4.48	3475	0.2	0.4	0.0	0.0
Kerguelen Island	-49.35	70.25	1.19	33	0.8	1.9	19.1	17.4
Kiel	54.33	10.13	2.29	54	0.9	1.3	1.9	1.5
Kingston	-42.99	147.29	1.88	65	0.9	0.5	7.1	8.1
LARC	-62.20	301.04	2.21	40	2.1	2.2	2.6	0.4
Lomnický Štít	49.20	20.22	4.00	2634	0.6	0.5	0.3	0.1
Magadan	60.12	151.02	2.10	220	0.0	0.6	6.3	5.9
Mawson	-67.60	62.88	0.22	30	3.8	1.4	23	23.1
McMurdo	-77.85	166.72	0.01	48	0.0	0.5	18.6	20.4
Moscow	55.47	37.32	2.46	200	2.2	1.1	2.2	2.2
Mt. Wellington	-42.92	147.23	1.89	725	1.6	0.6	8.1	7.3
Newark	39.68	284.25	1.97	50	0.8	1.3	2.0	1.8
Oulu	65.05	25.47	0.81	15	2.7	4.0	19.7	18.6
Potchefstroom	-26.68	27.10	7.30	1351	0.1	0.3	0.8	0.0
Rome	41.86	12.47	6.32	0	0.0	0.2	0.0	0.0
SANAE [a]	-71.67	357.15	1.06	856	3.4	3.4	22	22.0
South Pole	-90.00	0.00	0.10	2820	0.2	0.6	31.3	30.6
Terre Adelie	-66.67	140.02	0.01	45	0.0	0.6	18.3	18.4
Thule	76.50	291.30	0.00	260	2.8	2.8	22.9	23.1
Tixie Bay	71.58	128.92	0.53	0	1.4	0.8	15.3	18.8
Tsumeb	-19.20	17.58	9.29	1240	0.0	0.2	0.0	0.0
Yakutsk	62.03	129.73	1.70	105	0.0	0.6	10.3	15.7

[a] Normalisation station.

[b] Nominal vertical geomagnetic cutoff rigidities represent the minimum rigidities below which particles do not have access to a particular site on the Earth's surface. The cut-off at the geomagnetic equator is ~ 17 GV, decreasing to zero at the geomagnetic poles.

[c] Actual % increases corrected to standard sea level atmospheric depth.

[d] Calculated % increases.

TABLE A4

COMPARISON OF OBSERVED AND CALCULATED INCREASES FOR THE 14 JULY 2000 GLE

Station	12:10 UT.		12:20 UT		12:30 UT		12:40 UT		12:50 UT		13:00 UT	
	Observed [b]	Calculated [c]	Observed [b]	Calculated [c]	Observed [b]	Calculated [c]	Observed [b]	Calculated [c]	Observed [b]	Calculated [c]	Observed [b]	Calculated [c]
Apatity	17.2	17.1	16.1	15.9	15.4	14.9	15.4	13.8	13.2	13	11.5	11.4
Aragats	0.0	0.0	0.0	0.0	0.0	0.0	0.0	0.0	0.0	0.0	0.0	0.0
Climax	0.8	0.5	0.2	0.3	1.2	0.3	0.4	0.5	0.8	0.4	1.0	0.5
Goose Bay	18.5	20.7	16.7	18.3	15.5	18.3	15.2	15.6	13	15.8	12.8	15.5
Halcakala	0.0	0.0	0.0	0.0	0.0	0.0	0.0	0.0	0.0	0.0	0.0	0.0
Hermanus	0.4	0.0	0.7	0.0	0.0	0.0	0.0	0.0	0.0	0.0	0.2	0.0
Hobart	7.2	7.0	7.0	5.4	4.6	5.1	4.8	5.4	6.7	5.0	7.2	4.6
Inuvik	18.5	15.1	16.3	13.9	16.3	12.6	16.7	12.7	14.5	11.4	12.6	9.9
Jungfraujoch	0.0	0.0	0.3	0.0	0.2	0.0	0.3	0.0	0.0	0.0	0.0	0.0
Kerguelen Island	18.1	15.6	16.2	14.4	14.6	13.6	14.4	13.0	12.8	12.1	12.6	11.3
Kiel	2.7	1.5	1.8	0.9	1.7	0.9	3.1	1.3	2.0	1.0	1.9	1.1
Kingston	5.7	7.2	5.5	5.7	3.4	5.6	6.6	5.4	4.7	5.4	3.1	4.6
LARC	0.8	0.5	0.0	0.3	0.3	0.3	0.0	0.5	1.9	0.4	1.5	0.4
Lomnický Štít	0.4	0.1	0.0	0.0	0.5	0.1	0.5	0.1	0.0	0.1	0.1	0.1
Magadan	5.2	5.4	3.7	4.3	3.6	4.2	3.6	4.4	2.3	4.2	4.4	4.5
Mawson	21.2	20.1	20.3	18.2	14.6	18.2	15.1	15.1	13.9	15.5	13.0	14.6
McMurdo	17.8	19.3	16.8	18.3	14.6	16.0	14.8	15.9	13.3	14.1	11.7	11.8
Moscow	2.8	1.9	0.6	1.2	1.6	1.5	0.9	1.8	1.6	1.5	1.1	1.7
Mt. Wellington	7.1	6.6	5.2	4.9	5.9	5.0	5.8	5.4	5.4	4.5	5.2	5.0
Newark	3.1	1.5	2.8	1.0	0.6	1.1	2.1	1.5	0.6	1.3	0.0	1.6
Oulu	17.4	17.1	16.5	16.1	15.9	15.0	13.6	13.9	12.9	13	11.4	11.5
Potchefstroom	2.2	0.0	0.7	0.0	1.2	0.0	1.7	0.0	0.1	0.0	0.2	0.0
Rome	0.0	0.0	0.0	0.0	0.0	0.0	0.0	0.0	0.0	0.0	0.0	0.0
SANAE [a]	19.5	19.4	17.4	17.4	17.5	17.5	14.7	14.7	15.1	15.0	14.8	14.8
South Pole	27.4	26.8	25.4	24.9	24.1	23.1	21.6	21.3	19.9	19.3	18.5	17.8
Terre Adelie	16.7	17.0	14.9	15.9	13.3	14.9	13.7	13.9	12.9	12.9	11.8	11.5
Thule	21.5	21.5	20.3	19.4	16	18.5	16.1	15.4	14.5	15.9	11.9	14.4
Tixie Bay	13.9	17.2	14.7	16.1	12.7	15.2	9.5	14	10.3	13.0	9.8	11.7
Tsumeb	0.0	0.0	0.0	0.0	0.0	0.0	0.0	0.0	0.0	0.0	0.0	0.0
Yakutsk	8.9	13.9	8.5	12.9	7.7	10.7	7.1	11.8	6.9	10.7	5.3	9.3

[a] Normalisation station.
[b] Actual % increases corrected to standard sea level atmospheric depth.
[c] Calculated % increases.

TABLE A3

COMPARISON OF OBSERVED AND CALCULATED INCREASES FOR THE 14 JULY 2000 GLE

Station	13:10 UT.		13:20 UT		13:30 UT		13:40 UT		13:50 UT		14:00 UT	
	Observed [b]	Calculated [c]	Observed [b]	Calculated [c]	Observed [b]	Calculated [c]	Observed [b]	Calculated [c]	Observed [b]	Calculated [c]	Observed [b]	Calculated [c]
Apatity	12.6	11.9	10.5	10.5	9.7	9.3	9.4	9.2	8.8	8.2	8.8	8.3
Aragats	0.0	0.0	0.0	0.0	0.0	0.0	0.0	0.0	0.0	0.0	0.0	0.0
Climax	1.5	0.3	1.2	0.3	0.4	0.4	0.2	0.2	0.0	0.0	0.0	0.1
Goose Bay	11.1	13.0	9.6	12.4	11.2	12.5	9.9	11.3	8.7	11.0	8.7	11.0
Haleakala	0.0	0.0	0.0	0.0	0.0	0.0	0.0	0.0	0.0	0.0	0.0	0.0
Hermanus	0.4	0.0	0.0	0.0	0.0	0.0	0.1	0.0	0.0	0.0	0.0	0.0
Hobart	6.3	3.6	4.8	4.0	5.5	3.7	6.3	3.3	4.9	3.1	4.9	3.0
Inuvik	11.7	10.5	13.5	9.6	11.9	8.4	11.7	8.4	10.2	7.3	10.2	7.1
Jungfraujoch	0.3	0.0	0.0	0.0	0.0	0.0	0.1	0.0	0.0	0.0	0.0	0.0
Kerguelen Island	12.3	10.7	9.0	9.7	9.7	9.6	8.7	9.9	6.4	8.0	6.4	7.9
Kiel	1.7	0.9	0.3	0.8	1.3	1.0	0.4	0.8	0.7	0.5	0.7	0.5
Kingston	4.3	4.5	4.9	4.1	4.6	4.2	3.1	3.7	2.4	3.7	2.4	3.5
LARC	0.9	0.3	0.9	0.3	0.5	0.4	0.5	0.2	0.7	0.1	0.7	0.1
Lomnický Štít	0.0	0.1	0.0	0.1	0.0	0.1	0.0	0.0	0.0	0.0	0.0	0.0
Magadan	3.5	3.6	2.6	3.7	3.0	3.5	2.9	3.1	2.6	2.8	2.6	2.9
Mawson	13.1	12.8	11.1	12.4	13.0	12.4	10.8	11.1	11.0	11.2	11.0	11.4
McMurdo	11.7	13.1	10.8	11.8	10.2	10.9	9.9	10.4	8.1	9.0	8.1	9.0
Moscow	0.0	1.2	0.9	1.2	1.1	1.4	0.0	1.1	0.9	0.6	0.9	0.8
Mt. Wellington	3.7	3.9	3.3	3.5	4.5	3.8	3.3	2.9	2.8	3.1	2.8	3.3
Newark	0.0	1.1	0.3	1.0	0.2	1.1	0.0	0.8	0.0	0.6	0.0	0.7
Oulu	12.3	11.9	11.1	10.5	10.6	9.3	9.1	9.3	9.3	8.0	9.3	8.1
Potchefstroom	1.0	0.0	0.0	0.0	0.0	0.0	1.7	0.0	0.5	0.0	0.5	0.0
Rome	0.0	0.0	0.0	0.0	0.0	0.0	0.0	0.0	0.0	0.0	0.0	0.0
SANAE [a]	12.4	12.3	12.2	12.1	11.1	11.1	10.6	10.6	10.0	10.0	10.0	10.0
South Pole	17.6	17.3	15.7	15.1	15.6	15.2	14.5	13.9	13.0	12.0	13.0	12.0
Terre Adelie	12.3	11.9	10.5	10.4	8.2	9.1	10.8	9.2	8.5	7.5	8.5	7.4
Thule	12.2	12.6	12.2	13.8	10.7	10.6	10.3	10.9	8.0	9.0	8.0	8.8
Tixie Bay	7.9	11.9	8.4	10.4	6.9	9.0	6.9	9.2	5.3	7.5	5.3	7.4
Tsumeb	0.0	0.0	0.0	0.0	0.3	0.0	0.1	0.0	0.0	0.0	0.0	0.0
Yakutsk	5.1	8.1	5.3	7.8	3.9	8.0	3.6	8.0	5.3	7.0	5.3	7.2

[a] Normalisation station.
[b] Actual % increases corrected to standard sea level atmospheric depth.
[c] Calculated % increases.

APPENDIX B

RESULTS: 15 APRIL 2001

TABLE B1

COMPARISON OF OBSERVED AND CALCULATED INCREASES FOR THE 15 APRIL 2001 GLE

Station	Lat.	Lon.	P_c [b]	Alt.	13:55 UT		14:00 UT	
	(deg.)	(deg.)	(GV)	(m)	Observed [c]	Calculated [d]	Observed [c]	Calculated [d]
Alma Ata	43.25	76.92	6.69	3340	0.8	1.3	1.3	1.7
Apatity	67.55	33.33	0.61	177	0.7	0.0	4.9	4.0
Athens	37.97	23.72	8.72	40	0.0	0.4	2.1	0.2
Bern	46.55	7.98	4.42	570	0.0	0.4	1.1	3.4
Calgary	51.08	245.87	1.09	1128	12.4	9.8	42.7	41.4
Cape Schmidt	68.92	180.53	0.45	0	0.0	1.5	1.7	4.7
Fort Smith	60.02	248.07	0.30	0	10.0	9.7	30.6	34.2
Irkustk	52.28	104.02	3.66	435	2.5	1.3	5.8	8.9
Jungfraujoch	46.55	7.98	4.48	3475	0.0	0.4	1.4	3.2
Kerguelen Island	-49.35	70.25	1.19	33	0.9	0.0	1.3	2.8
Kiel	54.33	10.13	2.29	54	1.3	0.1	4.6	3.8
Kingston	-42.99	147.29	1.88	65	0.0	2.3	2.4	14.8
LARC	-62.20	301.04	2.21	40	0.2	2.9	8.7	12.2
Lomnický Štít	49.20	20.22	4.00	2634	0.3	0.3	1.7	3.8
Magadan	60.12	151.02	2.10	220	0.1	1.2	9.9	11.3
Mawson	-67.60	62.88	0.22	30	0.0	0.0	10.4	7.3
McMurdo	-77.85	166.72	0.01	48	3.5	2.0	24.8	14.3
Moscow	55.47	37.32	2.46	200	0.4	0.1	2.8	3.8
Nain [a]	56.55	298.32	0.45	0	6.9	6.9	44.3	44.3
Newark	39.68	284.25	1.97	50	2.9	3.7	11.1	16.3
Norlisk	69.26	88.05	0.63	0	0.0	0.0	0.6	2.6
Novosibirsk	54.80	83.00	2.91	163	0.0	0.4	5.5	7.0
Oulu	65.05	25.47	0.81	15	0.2	0.0	5.4	4.1
Peawanuck	54.98	274.56	0.27	52	5.0	10.0	54.4	51.5
Potchefstrom	-26.68	27.10	7.30	1351	1.5	0.6	0.2	1.1
Rome	41.86	12.47	6.32	60	1.5	0.4	2.0	0.9
SANAE	-71.67	357.15	1.06	856	3.7	1.5	23.4	23.9
South Pole	-90.00	0.00	0.10	2820	1.6	2.6	24.3	27.3
Terre Adélie	-66.67	140.02	0.01	45	1.3	0.1	14.1	4.2
Thule	76.50	291.30	0.00	260	6.7	5.6	31.6	24.8
Tixie Bay	71.58	128.92	0.53	0	0.0	0.1	0.9	2.8
Yakutsk	62.03	129.73	1.70	105	3.2	0.1	7.1	4.4

[a] Normalisation station.

[b] Nominal vertical geomagnetic cutoff rigidities represent the minimum rigidities below which particles do not have access to a particular site on the Earth's surface. The cut-off at the geomagnetic equator is ~ 17 GV, decreasing to zero at the geomagnetic poles.

[c] Actual% increases corrected to standard sea level atmospheric depth.

[d] Calculated% increases.

TABLE B2

COMPARISON OF OBSERVED AND CALCULATED INCREASES FOR THE 15 APRIL 2001 GLE

Station	14:05 UT		14:15 UT		14:25 UT		14:35 UT		14:40 UT		14:50 UT	
	Observed [b]	Calculated [c]	Observed [b]	Calculated [c]	Observed [b]	Calculated [c]	Observed [b]	Calculated [c]	Observed [b]	Calculated [c]	Observed [c]	Calculated [d]
Alma Ata.....	1.4	0.4	1.7	0.3	1.3	0.2	1	0.5	0.9	0.4	0.7	0.4
Apatity.....	12.7	10.8	21.2	30.7	30.5	44.6	34.3	50.0	32.3	49.8	34.8	49.8
Athens.....	1.2	0.0	0.0	0.0	1.9	0.0	0.0	0.1	0.0	0.0	0.7	0.1
Bern.....	2.8	4.3	4.4	3.5	4.0	2.3	6.9	3.2	5.4	2.5	4.3	2.4
Calgary.....	76.3	77.1	121.1	104.3	119.9	107.8	113.7	108.7	107.4	99.6	91.9	88.9
Cape Schmidt.....	10.2	6.5	33.6	21.7	51.5	34.2	54.3	41.7	58.9	45.0	61.7	53.4
Fort Smith.....	39.7	47.9	58.2	71.7	69.0	80.9	91.5	90.1	93.7	90.1	89.3	86.7
Irkustk.....	8.8	12.7	11.1	11.6	12.1	10.6	10.2	10.1	9.9	10.1	8.0	8.3
Jungfraujoch.....	3.5	4.3	4.3	3.5	3.3	2.3	3.2	3.0	2.9	2.4	2.8	2.3
Kerguelen Island..	3.6	5.4	18.0	18.4	30.1	30.4	39.9	37.3	42.2	37.1	46.6	40.1
Kiel.....	10.7	10.6	19.1	20.3	23.4	24.2	21.7	22.8	21.6	23.4	17.4	19.3
Kingston.....	15.4	32.3	47.4	55.1	59.1	61.3	55.1	62.7	54.8	61.8	47.3	54.2
LARC.....	14	14.0	17.3	19.6	18.7	20.3	16.0	17.8	14.6	16.0	12.1	13.3
Lomnický Štít.....	3.6	5.6	6.1	6.0	4.8	5.6	4.3	5.9	4.6	5.5	4.0	5.4
Magadan.....	23.7	27.2	42.0	51.0	46.2	56.7	48.0	56.3	46.2	56.9	41.3	52.1
Mawson.....	47.3	39.7	84.1	78.9	95.9	88.1	103.5	90.2	101.6	84.1	94.7	79.6
McMurdo.....	51.5	45.3	80.2	79.7	79.8	85.2	76.5	88.4	74.0	86.5	74.3	85.9
Moscow.....	9.3	7.9	20.6	18.2	24.6	26.9	22.8	21.5	23.3	24.0	22.4	23.6
Nain [a].....	86.9	86.9	110.2	110.2	113.8	113.9	115.4	115.5	104.7	104.8	92.5	92.5
Newark.....	20.9	33.7	28.3	36.9	32.9	38.1	29.2	35.3	28.3	33.2	23.7	28.1
Norlisk.....	0.5	3.4	13.4	14.2	21.1	26.7	28.3	32.7	30.1	32.0	32.5	34.5
Novosibirsk.....	10.5	14.1	17.6	23	16.8	23.6	16.7	22.7	16.4	20.9	13.9	20.4
Oulu.....	16.5	12.5	36.3	34	52.4	47.4	53.7	51.7	47.8	51.2	42.4	51.5
Peawanuck.....	109.2	86.3	107	101.9	110.7	101.5	109.7	95.7	103.0	88.5	94.1	73.5
Potchefstrom.....	0.0	0.3	2.4	0.3	1.2	0.2	0.7	0.5	0.0	0.3	0.1	0.4
Rome.....	1.0	0.3	1.5	0.3	2.4	0.2	1.7	0.5	1.5	0.4	1.7	0.5
SANAE.....	56.4	67.9	92.8	89.2	99.0	94.3	101.1	94.3	97.8	88.4	93.7	77.7
South Pole.....	77.1	81.6	106.9	112.4	115.3	114.7	124.3	115.8	110.7	105.3	100.4	94.8
Terre Adélie.....	22.8	10.2	40.9	29.3	58.6	39.2	61.4	43.6	59.6	45.5	69.8	52.2
Thule.....	47.3	33.0	64.3	48.7	77.0	61.4	81.1	71.7	82	74.6	75.1	69.7
Tixie Bay.....	1.0	3.4	12.8	14.1	24.6	26.2	32.5	32.3	34.4	32.3	40.3	37.0
Yakutsk.....	3.0	9.3	27.6	32.0	39.0	45.6	43.6	55.9	45.9	59.3	44.3	60.4

[a] Normalisation station.
[b] Actual% increases corrected to standard sea level atmospheric depth.
[c] Calculated% increases.

TABLE B3

COMPARISON OF OBSERVED AND CALCULATED INCREASES FOR THE 15 APRIL 2001 GLE

Station	14:55 UT		15:00 UT		15:05 UT		15:10 UT		15:15 UT		15:20 UT	
	Observed [b]	Calculated [c]	Observed [b]	Calculated [c]	Observed [b]	Calculated [c]	Observed [b]	Calculated [c]	Observed [b]	Calculated [c]	Observed [b]	Calculated [c]
Alma Ata.....	0.6	0.6	0.1	0.4	0.1	0.2	0.1	0.2	0.4	0.6	0.1	0.1
Apatity.....	36.6	48.9	40.1	46.8	39.5	42.4	37.8	39.4	35.3	36.5	30.5	34.9
Athens.....	1.4	0.1	0.0	0.0	0.7	0.0	0.0	0.0	0.6	0.2	2.3	0.0
Bern.....	6.8	3.0	4.3	2.0	2.1	1.5	4.3	1.3	2.1	1.9	2.7	0.8
Calgary.....	88	82.8	82.0	77.7	76.1	71.3	70.2	69.6	64.2	68.0	54.4	60.0
Cape Schmidt.....	71.4	57.9	65.3	54.3	64.2	54.9	62.0	51.6	59.1	48.8	54.8	48.7
Fort Smith.....	82.4	83.6	79.6	78.8	77.2	73.3	74.4	70.8	72.9	69.9	67.7	63.0
Irkustk.....	7.1	8.6	6.8	6.9	7.2	6.0	6.5	5.2	6.5	5.7	5.1	3.2
Jungfraujoch.....	2.3	2.9	2.3	1.9	1.8	1.5	1.9	1.2	1.8	1.8	0.9	0.7
Kerguelen Island..	46.2	40.4	44.5	39.0	40.4	36.6	38.3	35.6	37.3	35.6	35.9	31.6
Kiel.....	17.8	20.4	17	17.5	16.6	17.6	15.4	16.2	13.5	14.3	12.3	13.3
Kingston.....	45.1	51.8	43.1	45.8	41.4	45.2	37.7	42.6	34.1	39.3	31.1	34.7
LARC.....	14.0	13.1	12.0	11.1	10.2	9.9	8.3	9.5	8.6	8.8	7.1	6.2
Lomnický Štít.....	4.0	4.6	3.1	4.1	3.3	3.6	3.0	3.3	2.7	3.6	1.8	2.1
Magadan.....	38.4	46.3	35.2	44.3	33.5	40.8	30.8	36.8	29.1	34.6	26.0	33.3
Mawson.....	88.2	75.6	77.6	69.4	75.9	64.3	71.3	61.0	65.5	57.0	63.8	54.0
McMurdo.....	70.0	82.8	73.1	77.3	74.5	73.2	71.4	71.5	67.7	70.4	59.8	62.3
Moscow.....	20.4	22.4	18.6	20.7	17.1	21	16.9	18.8	15.9	16.0	14.2	14.6
Nain [a].....	85.7	85.7	80.4	80.4	73.2	73.2	70.5	70.5	68.4	68.4	61.8	61.8
Newark.....	22.9	24.7	21.1	22.6	18.8	21.9	15.5	19.4	15.8	17.4	13.9	14.3
Norlisk.....	32.7	33.9	33.5	34.4	32.8	32.1	34.1	31.9	32.2	31.5	29.9	27.2
Novosibirsk.....	14.8	18.9	12.2	18.2	13.1	16.2	11.6	15.3	9.4	14.8	8.9	12.2
Oulu.....	43.4	50.6	39.5	47.5	38.4	44.0	35.1	41.2	33.9	37.8	33.8	36.2
Peawanuck.....	83.0	66.1	81.2	62.3	77.9	57.2	75.5	54.5	71.4	50.8	69.7	45.1
Potchefstrom.....	0.7	0.5	0.2	0.3	0.0	0.2	3.1.0	0.2	0.2	0.5	0.7	0.1
Rome.....	2.3	0.6	2.0	0.4	3.2	0.3	3.1.0	0.2	2.3	0.6	0.4	0.1
SANAE.....	88.2	72.5	80.9	68.2	70.8	61.4	64.0	56.8	56.9	52.4	44.6	50.4
South Pole.....	97.4	88.0	90.1	82.4	85.4	75.9	81.9	74.3	82.7	73.9	59.5	64.3
Terre Adélie.....	64.0	54.7	58.2	53.3	53.5	54.4	50.9	51.6	48.3	48.1	46.5	46.5
Thule.....	72.0	69.5	69.5	67.3	65.6	60.6	59.1	54.2	56.1	50.5	54.8	52.3
Tixie Bay.....	40.4	38.8	39.0	37.3	36.8	37.3	33.2	36.0	33.0	34.8	31.9	32.9
Yakutsk.....	44.9	61.3	40.4	58.5	39.2	56.9	37.2	53.2	35.8	49.9	35.3	46.3

[a] Normalisation station.
[b] Actual% increases corrected to standard sea level atmospheric depth.
[c] Calculated% increases.

TABLE B4

COMPARISON OF OBSERVED AND CALCULATED INCREASES FOR THE 15 APRIL 2001 GLE

Station	15:25 UT		15:30 UT		15:35 UT		15:40 UT		15:45 UT		15:50 UT	
	Observed [b]	Calculated [c]	Observed [b]	Calculated [c]	Observed [b]	Calculated [c]	Observed [b]	Calculated [c]	Observed [b]	Calculated [c]	Observed [b]	Calculated [c]
Alma Ata.....	0.0	0.2	0.0	0.0	0.0	0.1	0.0	0.0	0.1	0.2	0.0	0.2
Apatity.....	28.1	31.8	27.2	30.8	24.6	29.5	26.0	29.7	21.7	30.0	23.2	27.5
Athens.....	1.6	0.0	0.6	0.0	0.0	0.0	1.9	0.0	3.3	0.0	0.0	0.1
Bern.....	0.5	1.0	0.4	0.6	2.9	0.7	4.5	0.5	2.6	1.0	2.4	0.9
Calgary.....	50.7	56.2	49.1	51.3	44.9	49.9	42.9	47.1	39.9	43.4	36.5	39.6
Cape Schmidt.....	50.1	42.3	46.2	40.8	36.4	36.0	36.9	36.1	33.4	30.1	33.6	27.5
Fort Smith.....	64.5	59.6	55.9	54.3	53.8	51.5	49.7	49.7	46.0	48.3	43.1	44.7
Irkustk.....	4.5	3.9	3.7	2.7	4.8	3.0	3.1	2.5	4.2	3.0	2.0	2.5
Jungfraujoch.....	1.1	1.0	1.0	0.6	1.0	0.7	1.0	0.5	0.4	0.9	0.5	0.9
Kerguelen Island..	33.9	30.4	33.1	29.0	31.1	27.2	31.7	26.9	29.4	31.0	29.5	28.6
Kiel.....	12.3	11.6	11.7	10.8	10.4	9.2	9.3	9.9	10.2	9.7	8.6	7.9
Kingston.....	31.5	33.5	25.7	30.0	25.8	30.0	23.6	27.9	23.7	23.2	21.1	20.0
LARC.....	5.4	6.4	5.9	5.6	5.8	6.0	5.5	5.3	4.9	5.1	4.3	4.5
Lomnický Štít.....	1.4	2.1	1.6	1.5	1.3	1.5	1.3	1.8	1.2	1.9	1.0	1.6
Magadan.....	23.1	30.5	22.2	28.4	19.8	27.0	19.8	25.7	17.7	22.1	16.4	18.8
Mawson.....	55.8	47.7	54.3	45.3	49.9	42.9	45.1	41.4	38.9	30.7	27.5	28.5
McMurdo.....	55.0	57.4	55	53.3	48.8	49.7	45.4	46.5	40.1	33.7	38.1	30.5
Moscow.....	12.9	14.2	12.2	11.9	12.1	13.0	10.4	10.5	11.1	11.3	10.0	10.3
Nain [a].....	58.2	58.2	53.1	53.2	51.4	51.4	49.3	49.3	43.9	43.9	42.9	43.0
Newark.....	16.7	13.7	11.8	12.7	12.1	12.7	12.0	12.3	12.2	10.8	11.6	8.8
Norlisk.....	29.5	26.7	28.5	26.1	27.5	24.8	24.4	23.9	23.6	31.5	24.0	28.9
Novosibirsk.....	7.9	11.3	7.3	10.3	7.0	9.6	7.6	10.1	5.8	7.9	6.0	7.3
Oulu.....	30.1	32.3	28.4	31.6	28.1	30.0	25.6	29.7	26.3	30.3	21.9	27.8
Peawanuck.....	64.6	43.2	60.1	39.9	58.8	39.1	53.8	36.7	52.3	46.7	46.5	43.8
Potchefstrom.....	0.8	0.1	0.0	0.0	2.0	0.1	1.9	0.0	0.8	0.2	1.3	0.2
Rome.....	2.7	0.2	1.9	0.0	1.1	0.1	1.3	0.1	1.3	0.2	1.1	0.2
SANAE.....	41.7	46.7	37.8	43.3	35.3	42.2	38.4	42.2	35.5	34.4	29.0	32.6
South Pole.....	59.5	60.9	52.1	55.6	49.1	53.4	44.6	50.1	42.1	41.6	38.6	38.8
Terre Adélie.....	38.5	39.4	36.5	38.8	39.1	34.1	42.1	32.6	41.7	29.8	38.8	27.4
Thule.....	52.2	49.2	49.2	44.5	47.0	42.4	47.0	45.0	44.9	40.8	41.9	40.0
Tixie Bay.....	29.9	29.8	29.1	29.4	25.4	26.6	23.3	26.0	25.4	30.5	26.9	28.1
Yakutsk.....	32.0	42.6	30.0	40.7	30.7	36.6	29.7	37.3	28.1	32.7	25.2	30.2

[a] Normalisation station.
[b] Actual% increases corrected to standard sea level atmospheric depth.
[c] Calculated% increases.

TABLE B4

COMPARISON OF OBSERVED AND CALCULATED INCREASES FOR THE 15 APRIL 2001 GLE

Station	15:55 UT		16:00 UT	
	Observed [b]	Calculated [c]	Observed [b]	Calculated [c]
Alma Ata.....	0.0	0.2	0.0	0.2
Apatity.....	20.5	26.5	19.3	24.5
Athens.....	0.0	0.1	0.0	0.1
Bern.....	1.2	0.9	0.3	0.8
Calgary.....	33.8	37.5	32.0	36.3
Cape Schmidt.....	32.2	26.7	36.3	24.6
Fort Smith.....	40.5	43.2	38.4	39.8
Irkustk.....	3.7	2.7	3.1	2.5
Jungfraujoch.....	0.7	0.9	0.4	0.8
Kerguelen Island..	29.6	27.3	27.4	25.5
Kiel.....	8.0	8.4	7.3	7.7
Kingston.....	20.8	20.4	19.2	19.7
LARC.....	5.6	4.4	5.3	4.2
Lomnický Štít.....	0.9	1.6	1.0	1.5
Magadan.....	16.6	18.7	13.6	16.8
Mawson.....	26.2	27.0	22.2	25.4
McMurdo.....	36.8	29.9	34.8	27.7
Moscow.....	10.3	9.9	9.3	8.3
Nain [a].....	37.8	37.8	37.0	37.0
Newark.....	10.5	8.2	9.3	7.8
Norlisk.....	21.3	27.8	19.8	25.7
Novosibirsk.....	4.4	6.6	5.8	6.4
Oulu.....	23.2	26.8	20.4	24.7
Peawanuck.....	43.9	39.8	42.1	39.0
Potchefstrom.....	0.4	0.2	0.9	0.2
Rome.....	0.7	0.3	0.1	0.2
SANAE.....	25.3	29.9	24.0	28.4
South Pole.....	37.2	36.5	35.5	34.9
Terre Adélie.....	35.9	26.3	33.7	24.4
Thule.....	39.7	35.3	35.7	32.8
Tixie Bay.....	28.9	26.8	24.4	25.0
Yakutsk.....	23.0	29.7	22.2	28.3

[a] Normalisation station.
[b] Actual% increases corrected to standard sea level atmospheric depth.
[c] Calculated% increases.

APPENDIX C

REFEREED PUBLICATIONS

Bombardieri, D. J., Duldig, M. L., Michael K. J., & Humble, J. E. 2006, Relativistic Proton Production During the 2000 July 14 Solar Event: The case for Multiple Source Mechanisms, Astrophys. J, **644**, 565

Bombardieri, D. J., Michael K. J., Duldig, M. L., & Humble, J. E. 2007, Relativistic Proton Production during the 2001 April 15 Solar Event, Astrophys. J, **655**, 813

Bombardieri, D. J., Duldig, M. L., Humble, J. E., & Michael K. J. 2008, An Improved Model for Relativistic Proton Acceleration Applied to the 2005 January 20 and Earlier Solar Events, Astrophys. J, **682**, in press

Klekociuk, A. R., Bombardieri, D. J., Duldig, M. L., & Michael K. J. 2008, Atmospheric chemistry effects of the 2005 January 20 Solar Proton Event, Advances in Geoscience, **14**, in press